Design and Growth of Luminescent Thin Films by Atomic Layer Deposition

Michael Norderhaug Getz

Dissertation for the degree of Philosphiae Doctor

Department of Chemistry
Faculty of Mathematics and Natural Sciences

UNIVERSITY OF OSLO

2017

Series of dissertations submitted to the
Faculty of Mathematics and Natural Sciences, University of Oslo
No. 1895

ISSN 1501-7710

Cover: Hanne Baadsgaard Utigard.
Print production: Reprosentralen, University of Oslo.

Preface

This dissertation presents parts of the requirements for the degree Philisophiae Doctor at the Faculty of Mathematics and Natural Sciences, University of Oslo. The work has been carried out at the group for Nanostructures and Functional Materials at the Department of Chemistry, and was funded by the Norwegian Research Centre for Solar Cell Technology, the Norwegian Research Council and industry partners in Norway during the period from October 2012 to September 2016, under the supervision of Per-Anders Hansen, Ola Nilsen and Helmer Fjellvåg.

I would like to express my gratitude to my supervisors Per-Anders Hansen, Ola Nilsen and Helmer Fjellvåg for their guidance, assistance and encouragement. As the courses available at UiO did not provide a solid background in luminescence, the countless scientific discussions with Per-Anders have been invaluable to my understanding and thus to this work, and I could never thank him enough.

Our group is also relatively new to the field of luminescence and we are still lacking some equipment like calibrated detectors and tuneable excitation sources. The collaboration with the group of Professor Andries Meijerink at the University of Utrecht, also initiated by Per-Anders, has consequently been essential for this work, and I would like to thank everyone from that group that helped me set up and perform measurements.

I also would like to thank my colleagues for a nice working environment and for offering assistance with equipment and providing a helping hand or suggestions whenever I had trouble with the reactor.

Finally I wish to thank my family and friends for supporting me, particularly my wonderful wife, Marit, for always believing in me and motivating me, and also for increasing my understanding of various scientific topics, including my own research, through numerous scientific discussions. I feel so lucky to share my life with such a lovely and intelligent person.

Abstract

Most solar cells exploit the ultraviolet (UV) region of our solar spectrum poorly, while being excellent in the near-infrared (NIR) range. The goal of this thesis has been to create luminescent materials able to enhance the efficiency of such solar cells by converting UV light to visible or NIR photons. The materials have been designed by the ALD method and analysed with respect to various optical and structural properties

The luminescent properties are designed using different structural units that absorb UV and units that emit in the visible or NIR. The ALD technique has proven highly suitable in design and distribution of such units from homogeneous mixtures to clusters and layers. As absorbers, both titanium phosphate and vanadates have been used, while lanthanides like Eu^{3+} and Yb^{3+} have been used as emitters

In the first article we demonstrate that as-deposited amorphous europium titanium phosphate can convert UV light to red, and exhibits unique properties like tuneable reversible reduction in luminescence intensity under UV or X-ray illumination, as well as an emission spectrum whose shape and intensity is highly dependent on the post-deposition annealing temperature and the Eu:Ti ratio in the samples. While the material appears to be a poor choice for enhancing solar cell efficiencies, due to low quantum efficiency and poor photostability under UV-excitation, the system is a good model system of a luminescent amorphous material and is important for understanding energy transfer in thin films made by ALD.

Working with the amorphous Eu-Ti-P-O system made me aware that achieving high energy transfer rates from the absorber to the emitter is easier if the host exhibits a reasonable quantum efficiency in the absence of the emitter. A crystalline host material would thus have a better chance of enabling high light-conversion efficiencies. Several host structures with metal cations in high oxidation states were considered due to these ions being easily reduced, which is an indication of a strong M-O charge transfer absorption. I eventually selected YVO_4 due to it being a well-known host material for lanthanides as it has a low-symmetry metal site that can easily be substituted with lanthanides like Yb^{3+}. The $Y_{1-x}Yb_xVO_4$ system also has the potential to convert one UV photon to two NIR photons, which in theory enables quantum efficiencies exceeding 100%. $(VO_4)^{3-}$ exhibits a strong charge-transfer absorption in the UV, and the absorbed energy can be transferred to two nearby Yb^{3+}, from which NIR emission takes place. Silicon solar cells utilize the energy in UV-photons poorly, but are excellent at utilizing NIR photons, making the system promising with respect to enhancing their efficiency.

In the second article we examine the $x = 1$ case, i.e. the $YbVO_4$ system, and demonstrate controlled growth of this system with ALD. We establish that $YbVO_4$ crystallization can be aided by an excess of V_2O_5 acting as a flux, reducing the onset of crystallisation by over 200 °C, and that the NIR emission increases with increased crystallinity. In the third article we determine the optimum Yb^{3+} concentration with respect to UV to NIR conversion by varying x, which at an excitation wavelength of 325 nm is determined to be ~8 mol% Yb^{3+}. We observe several strong indications of downconversion taking place. The energy transfer rate from $(VO_4)^{3-}$ to Yb^{3+} in a sample with ~2 mol% Yb^{3+} was measured to be 34%, resulting in a theoretical upper-limit quantum efficiency of 134%, though the actual quantum efficiency of the sample was determined to be ~15% due to strong quenching of the $(VO_4)^{3-}$ emission. The quenching can be reduced by increasing crystallinity, though additional research is required before we can establish whether a film with quantum efficiency exceeding 100% is possible. It is our interpretation that such a material could be realized in the future and $Y_{1-x}Yb_xVO_4$ should consequently be useful for enhancing the efficiency of solar cells.

In the third article we also demonstrate that it is possible to design a crystalline YVO_4-$YbVO_4$ layered material with a sub-nanometre layer thickness. This means that either or both of these materials may be used as building blocks when designing advanced optical structures by ALD. This could allow for fine control of optical properties by replacing the Yb^{3+} in some or all of the layers with various other lanthanides, and then tuning the optical properties by adjusting lanthanide concentrations by varying the amount of layers of the various types, thus enabling emission spectra engineering. This could be useful for applications where a combination of certain wavelengths is desired, like in artificial lighting.

The work can be considered a significant contribution to the currently ongoing search for materials that can harvest the light from the sun, while also contributing to understanding how deposition and annealing parameters affect the optical and structural properties of thin films deposited by ALD. The work can also be considered a contribution to the field of luminescence as a whole and several of the findings could be useful for improving existing or future applications.

Table of contents

Chapter 1 – Introduction

1.1 The basics of luminescence

Luminescent materials have become increasingly popular over the last couple of decades and are a crucial part of a wide range of technologies, most notably fluorescent lighting and light emitting diodes used in smartphones or TV displays, but also in less used technologies like lasers [1], sensors [2], bio-markers [3] and scintillators [4]. It is no exaggeration to say that the market for luminescent materials is tremendous. Currently there is an ongoing search for luminescent materials that can be used to harvest the energy in the natural light from the sun, and this thesis is a contribution to this search.

In order to understand what a luminescent material is, it makes sense to first understand non-luminescent materials. Most materials absorb visible light, and hence, the colour of the reflected light we perceive is the complimentary colour to the absorbed light. The exception is completely white materials that reflect all visible light. In a non-luminescent material, the absorbed light is used to heat the material, an effect we commonly embrace when exposing ourselves to the sun, as our bodies mainly consist of non-luminescent materials. Black clothes also raise the body temperature faster than white ones. Unless a black material is heated to more than 600 °C, it will not emit anything of the absorbed light back as visible light, everything will be lost as heat. In luminescent materials, parts of the absorbed light will be reemitted, usually in the form of visible or infrared light, a process called luminescence. In order for luminescence to take place, there needs to be a range of unavailable energy levels between the electronic ground state and the electronic excited states. In semiconductors this gap is referred to as E_g, while for other materials ΔE is typically used. In order to absorb energy, this energy gap needs to be comparable to the energy of a quantum of electromagnetic radiation, called a photon. When an electron is excited across the energy gap by a suitable photon, it will have the option to relax back to the ground state by emitting a new photon. This concept is illustrated in **Figure 1.1.**

The energy of the emitted photon will be lower in energy than the absorbed photon, usually somewhere between ultra violet (UV) and infrared (IR). In this way, luminescent materials can be used to convert light to longer wavelengths.

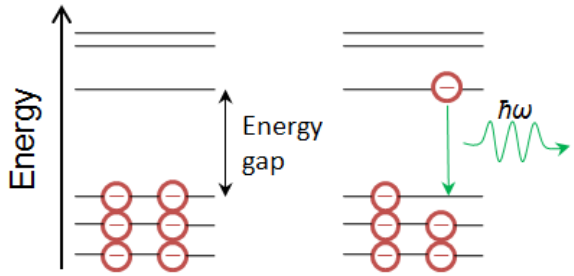

Figure 1.1: The electronic structure of a material can be described as a set of orbitals where the allowed states of the electrons in the material are depicted by horizontal lines. The configuration in which the electrons occupy the orbitals with the lowest possible energy, with at most two electrons per orbital, is called the *electronic ground state* of the material. The material is in an *excited state* if one or more of the electrons occupy a higher-energy orbital. The material is considered to be luminescent if the electron can relax to the ground state by emission of a photon.

1.2 Luminescent materials for solar cells

There are several types of luminescence depending on how the electron is excited. Excitation by an electron beam results in cathodoluminescence, while electric voltage can give rise to electroluminescence, and triboluminescence can be observed by excitation through mechanical energy. Excitation by X-rays can give X-ray luminescence and chemical reactions can result in chemiluminescence, etc. In this thesis, we will only consider photoluminescence, which is achieved by exciting a luminescent material with electromagnetic radiation, typically UV. By converting UV light to visible or near-infrared (NIR), it is possible to enhance the efficiency of solar cells [5, 6]. Solar cells are similar to luminescent materials in the way that there is an energy gap in the material. However, unlike a luminescent material, the solar cell aims to harvest the energy of the excited electron directly, by making it move through a circuit, instead of letting it relax back to the ground state and emit light or heat, as shown in **Figure 1.2**.

So, how can a luminescent material affect this process? To answer this, we first have to examine the loss mechanisms present in a solar cell. In order for an electron in the depletion region to become excited in silicon, a minimum energy of 1.1 eV, i.e. 1100 nm light, is required to bridge the energy gap. Photons with lower energy than this are not able to excite an electron, and thus do not contribute towards generating electricity. By examining the solar radiation spectrum received on earth shown in **Figure 1.3**, it is evident that about 20% of the energy from sunlight received on earth consists of photons with too low energy to generate electricity. It is also apparent that a lot of the sunlight has a shorter wavelength than

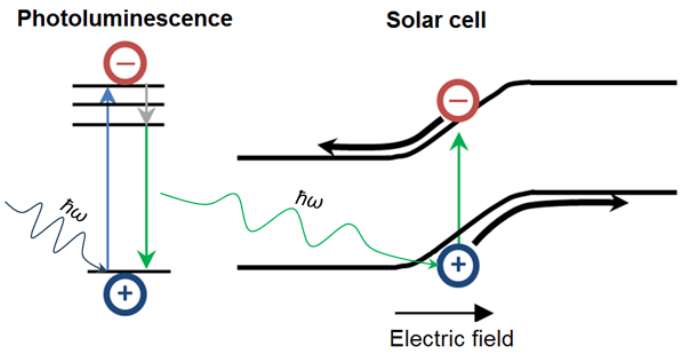

Figure 1.2: The left diagram shows an example of a photoluminescence process in which a blue photon is absorbed, resulting in the emission of a green photon when the electron recombines with the hole left during the excitation. In a solar cell (right), the electron and hole are separated by an electric field after the excitation process (e.g. by a green photon from the conversion layer) in order to make the charges move through a circuit to generate electricity.

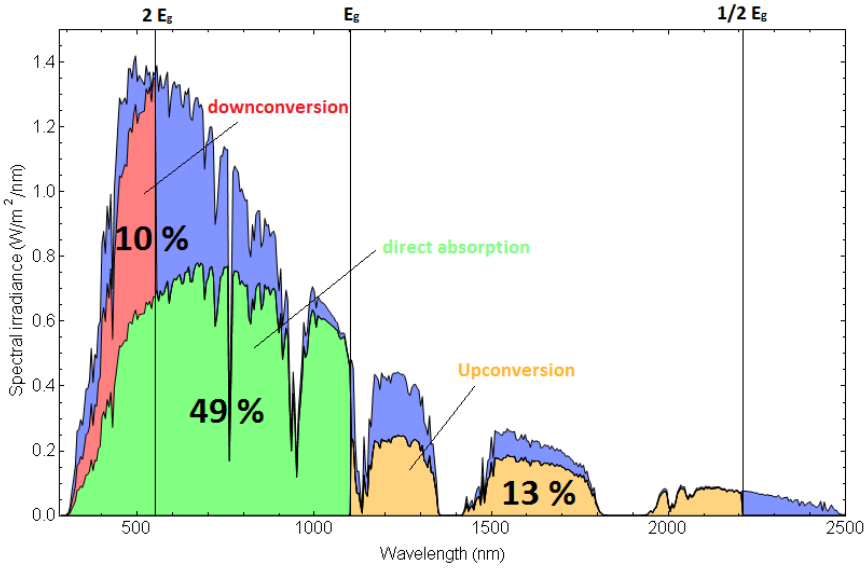

Figure 1.3: Solar radiation spectrum received on earth at sea level is shown in blue. Of all the energy in the sunlight, only 49% is directly utilized by a crystalline silicon solar cell (green). Any photon energy in surplus of the bandgap of silicon (1.1 eV), is lost to thermalization. Photons with an energy of 2.2 eV or more (550 nm), shown in red, could in theory be split in two photons with an energy of 1.1 eV each, resulting in a theoretical reduction of the thermalization losses from 30% to 20%. Photons with energy below 1.1 eV, but above 0.55 eV (2200 nm), shown in yellow, could in theory be upconverted by converting two low-energy photons to one high-energy photon.

1100 nm, carrying more energy than needed to excite an electron in silicon. This excess energy is not utilized in any way, but heats the solar cell, reducing its efficiency substantially. The thermalization loss and the heat generated within the cell increases with decreasing wavelength and in total accounts for approximately 33% of the total energy in the sunlight as well. This puts the theoretical highest efficiency of a silicon solar cell at slightly less than 50%

before accounting for other unavoidable losses, like recombination resulting in photons that exit the cell, blackbody radiation, and most importantly, that the optimum fill factor for a solar cell can at most be ~86%*. In total, this results in an upper limit for solar cell efficiency of 33.7%, for an ideal single bandgap material with a bandgap of 1.34 eV. This is known as the Shockley-Queisser limit [8]. The bandgap of silicon is slightly below this, and is also indirect (**Figure 1.4**), resulting in poor absorption near the band edge (950-1100 nm), resulting in a slightly lower limit. Some additional factors neglected by Shockley and Queisser reduce the limit even further, most importantly that the limited mobility of holes compared to electrons means that above a certain rate of production, there will be so many holes produced that the faster moving electrons will recombine with the holes left by previous photo excitations. This results in an upper limit on the rate of electricity production, causing an additional loss of 10% in silicon [9]. In addition, Auger recombination also causes some additional loss, which combined results in an upper efficiency limit for mono crystalline silicon of 29.4% [9], i.e. only a few percent above the current world record of 25.6% [10]. In practice, most commercial silicon solar cells currently have efficiencies in the range of 16-20%, though Panasonic currently make commercial solar cells with efficiency as high as 22.5% [11].

The reason why most cells perform well below the Shockley-Queisser limit is that in order to create a p- or n-type material required for solar cells, numerous defects have to be introduced through the doping process. One of the dopants required to make a p- or n-type material is introduced during the crystallization process, while the other dopant is introduced afterwards and will only affect the front and the back of the solar cell and the doping concentration of this dopant is several orders of magnitude higher than that of the other. The dopants on one of the sides, usually the back, are charge-compensated by coating with a

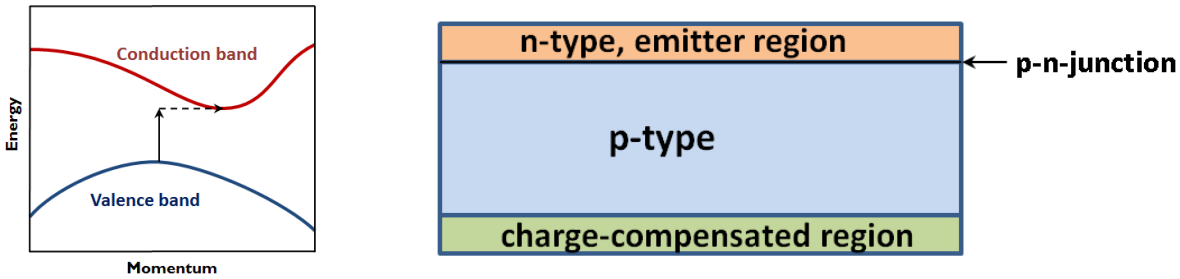

Figure 1.4: Left: Energy vs. crystal momentum for a semiconductor with an indirect band gap. A photon with an energy corresponding to the band gap would require the assistance of a phonon (dashed arrow) in order to be absorbed. **Right:** Illustration of a p-type silicon wafer after being subjected to an n-type dopant, followed by charge-compensation of the backside.

*Fill factor is the ratio of maximum obtainable power to the product of the open-circuit voltage and short-circuit current. The upper limit used here is the corresponding value that Shockley and Queisser used in their calculations. GaAs solar cells can have fill factors approaching 89%, while Silicon cells have fill factors approaching 85% [7].

different donor or acceptor material, e.g. if the back and front are doped with phosphorous, the back side can be compensated with aluminium and thus does not form a p-n junction, as shown in **Figure 1.4**. The dopants on the front side form the p-n junction required to produce the electric field that separates the electric charges generated in the cell. The heavily doped region is called the emitter region and electrons excited in this region will have a higher probability of being trapped by defect states, i.e. states that lie in the energy gap that excited electrons can relax to. The emitter region is usually found in the top of the solar cell, which is also where the shortest wavelengths are absorbed, i.e. UV light, due to the strong absorption of silicon at these wavelengths. For this reason the external quantum efficiency (EQE), i.e. the amount of extracted electrons per incident photon on the solar cell in this region is severely reduced, as can be seen in **Figure 1.5** for various solar cell technologies [5]. A luminescent material able to convert UV light to visible or NIR, called a *downshifting* material, would consequently increase the EQE of silicon solar cells in the UV region and provide a slight efficiency increase. Chen *et al.* for instance observed an efficiency increase of a silicon cell from 17.1% to 17.7% by adding a luminescent UV conversion layer [12], which is a relative increase of 3.5% and could be worthwhile as long as adding the luminescent layer does not come at too high cost.

However, a simple one-to-one UV to visible or NIR photon conversion will not break the Shockley-Queisser limit that the best solar cells are approaching. In order to breach this limit there are two options. Either, the solar cell can be modified to fit the solar spectrum by adding more junctions of different types of materials in order to harvest more of the lower energy light and to better utilize the higher energy part of the spectrum, in what is called a tandem or multi-junction solar cell. Alternatively, the solar spectrum can be modified in order to suit the solar cell by using a luminescent material. The first method has already seen remarkable success, sporting efficiencies as high as 46% [13]. These cells are the epitome of

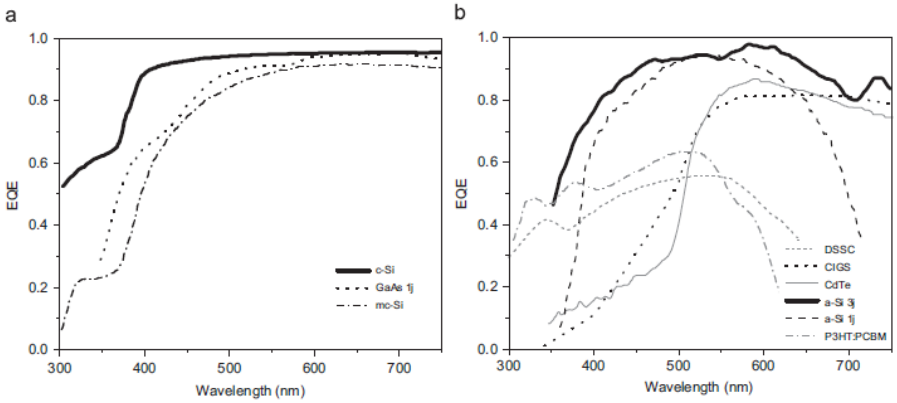

Figure 1.5: External quantum efficiency vs. wavelength for various solar cell technologies. UV-conversion is particularly beneficial for the non-silicon based technologies; however, even for silicon there is something to be gained. Adopted from [5].

materials engineering and extremely expensive and difficult to make. Covering large areas with such technology is currently not economically feasible and using solar concentrators to focus sunlight onto a small cell area is the most cost-efficient way of using these cells. The problem with concentrators is that the efficiency drops very quickly under low lighting conditions, which can only be remedied by employing a solar tracker. This introduces significant costs and also requires regular maintenance. They are thus presently considered much less reliable than conventional large area single-junction solar cells.

The second method to breach the Shockley-Queisser limit uses processes called upconversion or downconversion. These processes will be explained in more detail in chapter 2, but the basic principle of downconversion is to convert one high-energy photon to two photons with lower energy, while the principle of upconversion is to convert two low-energy photons into one photon with higher energy and thus utilize most of the energy in the solar spectrum. The downconversion layer should be placed in front of the solar cell, so that all the UV photons that impact on the cell are absorbed by the conversion layer and not the silicon. If the photons emitted by the conversion layer radiate equally in all directions, only half of the photons will be emitted in the direction of the solar cell and nothing is gained. In order to control the direction of the emission by the conversion layer, the refractive index, n, of both the conversion layer and the solar cell needs to be large, as illustrated in **Figure 1.6**. For a solar cell with a bandgap of 1.1 eV, Trupke *et. al.* calculated in 2002 that the upper limit with an ideal conversion layer placed in front of the solar cell with sufficiently high refractive index is 38.6% [6].

Since then there have been many attempts to achieve downconversion for solar cells, but this has so far not been very successful. The most promising systems involve materials that absorb UV light and transfer this energy to two Yb^{3+} ions, whose luminescence takes place in the 980-1050 nm region, i.e. close to perfect with respect to the 1100 nm band gap of silicon. Due to the indirect band gap of silicon, the wavelengths close to the band gap are poorly absorbed as previously shown in **Figure 1.4**, which means that these wavelengths are absorbed far away from the surface and in a region with few defects. This energy is consequently well-utilized provided that the silicon layer is thick enough that everything is

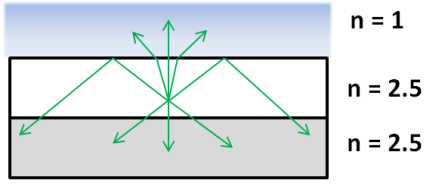

Figure 1.6: Illustration of the concept of total internal reflection. If the refractive index of the conversion layer and solar cell are similar and large compared to air for the wavelengths of interest, a large part of the luminescence that is directed opposite of the cell will be totally or partially reflected internally and can thus be utilized by the solar cell.

absorbed. An emission at 980 nm indicates that two Yb^{3+} ions should be able to split photons with wavelength below 490 nm, i.e. the UV-part of the solar spectrum. An alternative to Yb^{3+} would be Ho^{3+}, whose main emission takes place at ~900 nm, but also has significant emission below the band gap of silicon and was thus considered less suitable than Yb^{3+}. The main challenge with using Yb^{3+} is finding a suitable absorbing material that can transfer the absorbed energy efficiently to it. Even if the conversion layer doubles the amount of energy that can be utilized from each absorbed photon, it will not increase the efficiency of the solar cell significantly if only a small part of the total energy from the sun is absorbed. Finding a host that absorbs UV light efficiently, while also being able to transfer the absorbed energy efficiently to two nearby Yb^{3+} atoms is very challenging. Another problem is that in order for this energy transfer to be efficient, there needs to be plenty of Yb^{3+} ions ready to receive the absorbed energy, but due to an effect called concentration quenching, most of the energy is lost if the distance between several Yb^{3+}ions becomes too short. This happens naturally when the Yb^{3+} concentration becomes too large. This effect will be explained in more detail in chapter 2.

1.3 Motivation

Luminescent materials are used in a wide range of applications, any of whom could potentially benefit from improved materials or better understanding of them. The motivation for working with solar cells in particular is due to the energy challenge facing humanity. Most of the major challenges the world is struggling with is either directly or indirectly related to the need of energy, be it food, water, pollution, war, poverty or climate change. Numerous reports have stated the negative impact our society has on the Earth's climate [14, 15], and although there have long been heated arguments as to what degree emissions and deforestation are responsible, it is a fact that CO_2 absorbs large parts of the infra-red emission. This can be seen in the solar spectrum in **Figure 1.3**, where large portion of the infra-red appears to be missing, which is mainly due to this part being absorbed by CO_2 before reaching the surface of the earth. Likewise, CO_2 also prevents these wavelengths from ever leaving the earth, which is why CO_2 is a greenhouse gas. There is currently more or less general consensus among climate scientists that CO_2 contribution to global warming is significant [16, 17].

It is evident that the Earth will become a harsher place for humans to inhabit if the global temperature continues to rise. And, a large scale shift to renewable energy sources is required in order to reduce CO_2 consumption and to meet the growing need for energy. Non-renewable energy sources, as the name suggests, will at some point be expended, and thus a shift to renewable energy has to take place sooner or later to compensate for the increasing energy demand. Solar energy is by the far the largest energy source available on Earth and

the only energy source that alone has the potential to satisfy the worlds growing need for energy. The amount of solar energy reaching the Earth is approximately 10 000 the world's energy consumption *per hour*, and although photovoltaics (PV) only can utilize a small fraction of this, it is still possible for current PV systems to deliver between 3-100 times the worlds energy consumption when taking into account realistic conversion efficiencies and available land mass [18]. Calculations also show that covering a small section of Spain with solar cells could power all of Europe, while a small section of Nevada or Utah can power the entire United States [19]. Solar power also has the benefit of working best in the regions lacking energy the most, like Africa and southern Asia, and also providing energy when it is needed, i.e. during the day. It is evident that solar power has a tremendous potential as a renewable energy source. **Figure 1.7** shows the growth of PV in the period from 2006-2014, as well as a projection for the future. The figure shows that the production of photovoltaic installations is growing exponentially and solar energy is looking to become a crucial energy source in the future.

The cost of the actual solar cell module accounts for approximately 1/3 of the total cost of a new solar cell installation [20]. The efficiency of the cell thus has a significant impact on the return rate. A small increase in efficiency is usually worthwhile despite substantially increased production costs, as the additional module price becomes negligible compared to the extra energy produced in the long term. Increasing the efficiency of solar cells by using luminescent materials is therefore expected to have large beneficial implications for PV if it can be realized.

As most solar panels are flat with a textured surface, a logical way to apply the luminescent material is as a conformal thin film in front of the solar cell, or possibly behind in the case of upconversion. Atomic Layer Deposition (ALD) is a method of depositing thin

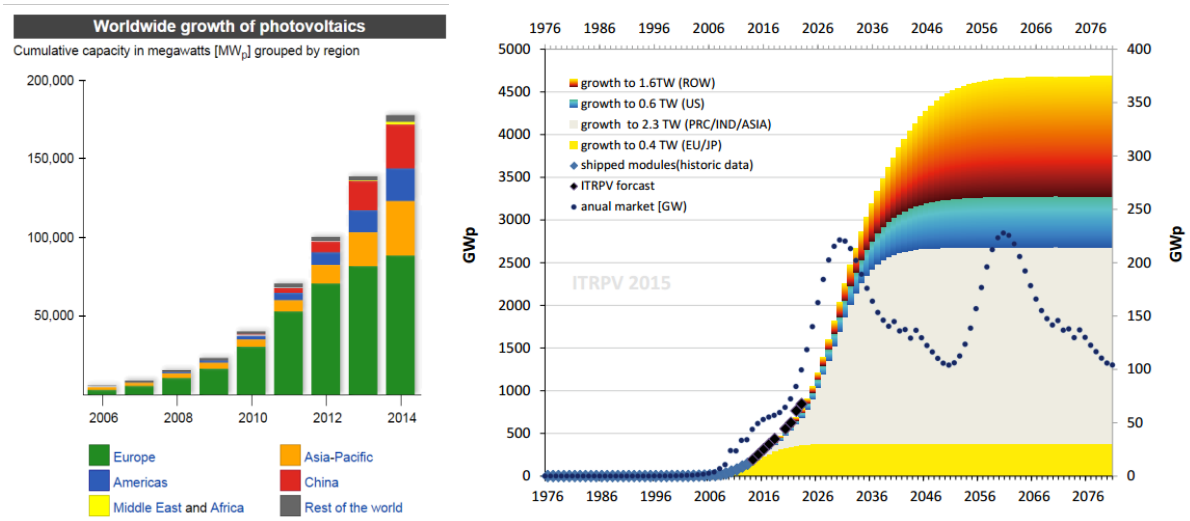

Figure 1.7: Worldwide growth of photovoltaics in the period of 2006-2014 (left) and estimated growth for the next 60 years (right) [21, 22].

conformal films with precise control of the atomic distribution and film growth, as each film is grown one sub-monolayer at a time. The wafer-based semiconductor industry has already been using the ALD technique to develop a wide range of products and components [23]. In order to improve system miniaturization and integration, the thin films needs to be uniform, dense and conformal as well as free from pinholes, cracks and other defects. ALD is superior to physical vapour deposition and regular chemical vapour deposition in this regard, particularly on the nanoscale. Defects are a serious problem for luminescent materials, as defects can potentially trap excited electrons and thus reduce the luminescence, and it is therefore preferable to use methods that introduce as few defects as possible. As the films are uniform and conformal across the reaction chamber it is also possible to coat several substrates simultaneously, and in this way create a large amount of identical samples. This is highly desirable not only from a research perspective, but also with regards to upscaling. It allows for large volumes to be coated simultaneously, which is a challenge for most other deposition techniques. In the solar cell industry, where ALD is used for deposition of Al_2O_3 as an ultrathin passivation layer, it is possible to coat several square meters simultaneously by positioning the wafers back to back, either vertically or horizontally [24].

ALD allows for both accurate control of atomic distances and for the option of making layered structures with precise thickness control. This could for instance be used in a way to control the energy transfer between certain ions or to reduce energy migration in certain directions by means of an intermediate layer. The options available with ALD are tremendous if suitable deposition processes can be found, controlled and understood, and engineering the perfect downconversion material may indeed be possible with this technique at some point. Synthesizing promising luminescent materials with ALD is thus expected to help realizing this process in the future and should yield several novel and interesting results along the way.

In this thesis, we investigate the luminescent properties of two systems made by atomic layer deposition. One is a highly complex amorphous material consisting of europium, titanium, phosphorous and oxygen. While this system is unable to produce two visible or NIR photons from one UV photon, it could be reasonable at a one-to-one conversion, which could still be useful for regular single-junction solar cells with poor UV-response (**Figure 1.5**) or other applications. A similar system without phosphorous was investigated previously by our group [25, 26] and some preliminary tests revealed that the addition of phosphate increased the luminescence significantly, warranting further investigation.

The second system is crystalline $Y_{1-x}Yb_xVO_4$. This system is promising as it uses a host material that has a strong and broad absorption in the UV while also displaying an energy level structure that could allow for simultaneous energy transfer to two Yb^{3+} ions, and could consequently display downconversion. Currently, there are two studies that have investigated the energy transfer of this system in the literature [27, 28], and both argue that

downconversion is likely to take place, though no definite proof of downconversion has been presented and no >100% quantum efficiency has been measured. Being able to deposit this system with ALD, and improving the understanding of the energy transfer processes taking place in this system, could be an important step in realizing an efficient conversion layer for solar cells. It would also be interesting to compare quantum efficiencies of films made by ALD to powders or films of the same material made by other techniques to determine whether ALD is a suitable technique for synthesizing luminescent materials.

Chapter 2 – Excited state dynamics and spectroscopy

2.1 Absorption of light

Electromagnetic radiation consists of a continuous range of wavelengths or frequencies, though the solar spectrum is limited to the range of 250-2500 nm. Electromagnetic radiation in this range is thus often referred to as *light*. The dominant interactions between light and inorganic matter are through refraction, reflection and electronic transitions. Refraction is a change in the direction of a propagating wave due to an interface between two mediums of different refractive index. Light waves will for instance refract when transitioning from air to water and vice versa as the refractive index of air is approximately 1, while it is about 1.3 for water. This can be observed by partially submerging something in water, which gives the illusion of the object being "bent". When a propagating wave is refracted, there will always also be some amount that is reflected depending on the incident angle and the difference in refractive index, as described by the Fresnel equations. For incident light normal to the surface, the reflectance, R, is given by:

$$R = \left|\frac{n_1 - n_2}{n_1 + n_2}\right|, \tag{2.1}$$

where n_1 and n_2 are the refractive indices of the two mediums the light passes from and to, respectively. For silicon, with a refractive index of n = ~3.45 for wavelengths present in the solar spectrum, it becomes apparent that approximately 30% of the incident light is reflected. For this reason, anti-reflective coatings are very important for the efficiency of solar cells.

The final dominant interaction between light and matter are electronic transitions, which happens when one or more electrons take up energy from a quantum of light, called a photon, and gets excited to a state with a higher energy. The energy of the electromagnetic wave is thus absorbed and transformed to internal energy of the absorber. The unoccupied energy state can be situated on the same atom as the excited electron, but can also be situated on a neighbouring atom, which means that the negatively charged electron is moving between two different atoms, resulting in a change in oxidation state of the atoms involved. The process is consequently called charge transfer (CT). The process is wavelength specific,

as the energy difference between the occupied state and the unoccupied state needs to match the energy of the incident photon precisely for the process to take place. The chlorophyll in plants for instance, selectively absorbs red and blue light, resulting in the green appearance of most plants as shown in **Figure 2.1**.

Some materials, like semiconductors typically absorb a wide range of wavelengths. The occupied states in these materials consist of many discrete energy levels that have merged together into energy bands, and can thus take on a wide range of energies that are separated from the unoccupied states by the energy gap between the bands. Materials with these band gaps are characterized by an absorption edge, as all photons of lower energy than the energy gap are transmitted and those of higher energy are absorbed.

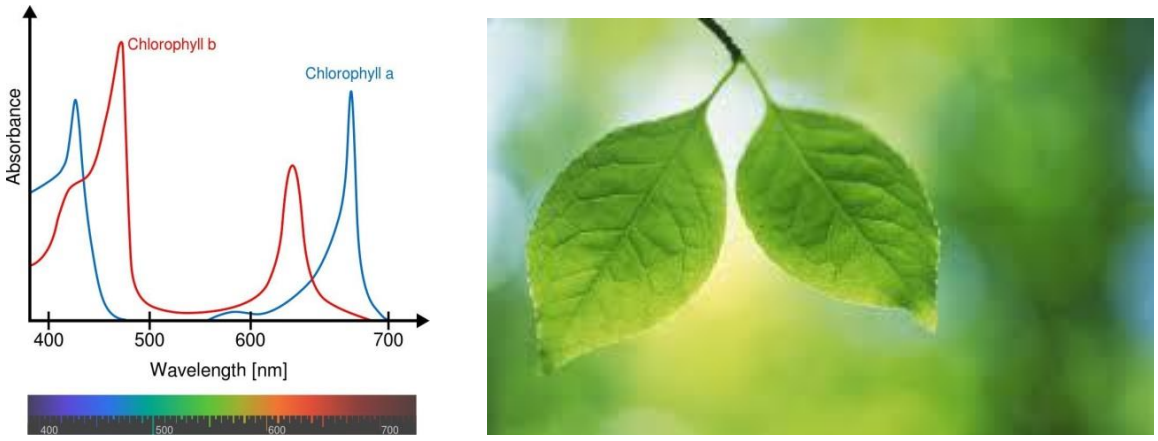

Figure 2.1: The absorption spectrum of chlorophyll a and b [29], resulting in the green colour of the leaves of a tree [30].

2.2 Radiative decay

The opposite process of absorption of light is the emission of photons, i.e. luminescence. For this process to take place, an excited luminescent centre must emit a photon in order to reach a lower energy state. As this process results in radiation being produced, it is called radiative decay. If the excited electron reaches a lower lying energy state by the production of lattice vibrations, or any other method, the process is called non-radiative as no photons are emitted in the process. In a luminescent material, the non-radiative decay is competing with the radiative decay and the ratio between them is used to determine the quantum efficiency. If the quantum efficiency is 10% it means that 10% of the excited electrons relax via radiative decay, while 90% decay non-radiatively. If an electron is in a state from which radiative decay can take place, it will usually do so spontaneously by emission of a photon. The rate of spontaneous emission, γ_{if}, or in general conceptual terms, the transition rate between the initial and final state of a system, follows Fermi's golden rule:

$$\gamma_{if} = \frac{2\pi}{\hbar}|M_{if}|^2\rho_f, \tag{2. 2}$$

where $\hbar$ is the reduced Planck constant and M_{if} is the matrix element describing the coupling between the initial and final state, e.g. a transition will proceed more rapidly if the coupling between the initial and final states is strong. The coupling term also gives rise to the selection rules that determine the strength of the electronic transitions. ρ_f is the electronic density of final states that the excited electron may transition to, and depends on the refractive index surrounding the emitter.

2.3 Lanthanide ions

The lanthanides are a group of elements that span the atomic numbers 57 through 71 and are unique due to their filled or partially filled f-orbitals, whose nature gives them particularly interesting absorption and emission properties, making them useful as luminescent materials. They are most commonly trivalent and are in nature generally found as mixtures of many different 'rare earth' elements. The rare earth (RE) elements, most of whom are in fact quite common; include the lanthanides in addition to yttrium and scandium, which are chemically very similar to the lanthanides. Due to their similar chemistry, some of them are very difficult to purify. Their similar chemistry also means that they easily can substitute for each other. Most phosphor and laser based materials based on lanthanide luminescence consist of a host crystal containing Y^{3+} (e.g. YAG: $Y_3Al_5O_{12}$ and YVO_4) or La^{3+} ($LaPO_4$), with a few percent of the non-luminescent Y^{3+} or La^{3+} replaced by luminescent dopants such as Er^{3+} or Nd^{3+}. The transitions taking place in lanthanides are usually within the partially filled f shells, i.e. they are called intraconfigurational f-f transitions as the electrons redistribute themselves over the 4f orbitals, while the $4f^n$ electronic configuration remains the same. This rearrangement does not necessarily require a lot of energy and some of the transitions can take place as low in energy as in the NIR, though transitions in the vacuum ultra violet (VUV) range also exists among the lanthanides. Some lanthanides, like Ce^{3+} and Eu^{2+}, also exhibit f-d transitions in the visible or UV part of the spectrum in which an electron is excited from the $4f^n$ ground state to a $4f^{n-1}5d^1$ excited state or vice versa. Intraconfigurational transitions are also common among the transition metals; however, one of the things that make the lanthanides special is the fact that the f-shell is shielded by the occupied 5s and 5p shells as shown in **Figure 2.2**. The probability for a 4f-electron to be affected by neighbouring atoms is thus small, which means that the host material only has a minor impact on the intraconfigurational 4f transitions, which is in contrast to transition metals where the crystal field has a significant impact on the energy of each state. They are therefore quite similar to free ions, however, due

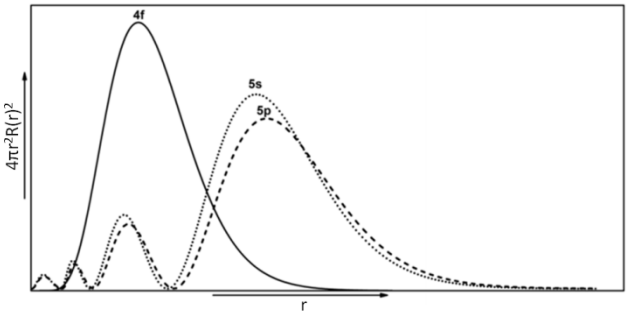

Figure 2.2: Radial electron distribution for 4f, 5s and 5p electrons typical for trivalent lanthanide ions (adapted and modified from [31]).

to the sheer amount of possible ways to distribute electrons over the 7 f-orbitals, and the splitting of them due to Coulombic, spin-orbital and crystal field interactions, means that there are a vast amount of energy states ranging from 1000 – 193 000 cm^{-1} (24 eV) that emission and absorption may take place to and from [32].

Coulomb repulsion arises from fact that similar charges repel each other, and is the most important reason why the various ways to distribute electrons over different orbitals result in widely separated energy levels. The Coulomb repulsion energy, V_c, between two negatively charged electrons at a distance, r, is given by:

$$V_c = \frac{e^2}{4\pi\varepsilon_0 r^2}. \tag{2.3}$$

Even though the 5s and 5p orbitals are filled for most of the 4f-elements, their distance from the nucleus are larger compared to the 4f orbitals, as shown in **Figure 2.2**. From this, it becomes evident that the 4f electrons must experience a strong positive net charge from the protons in the nucleus, which becomes stronger with increasing atomic number. This is known as the lanthanide contraction, which is no different than for 3d metals, except that it is even more pronounced due to less shielding and that there are more f- than d-orbitals. As the electrons in the 4f-orbitals experience such a strong pull from the core, the f-orbitals become compact relative to the s and p orbitals as they are filled and the Coulomb repulsion between the electrons thus becomes strong. Using the size of the f-orbitals ($r \approx 1$ Å), a rough estimate on the Coulomb repulsion energy between two f-electrons, results in $V_c \approx 14$ eV, which clearly has a tremendous effect on the energies of the 4f electrons, and explains why most of the lanthanides display luminescence. For instance, Eu^{3+} has 6 f-electrons that can fill the 7 4f-orbitals in $\binom{14}{6} = 3003$ different distributions. By only considering the kinetic energy of the 4f-electrons and interactions with the nucleus and the 54 core electrons, then all the distributions would have the same energy, however, Coulombic repulsion causes the $4f^6$ states to split, giving rise to terms that have well-defined total orbital angular momentum, L,

and spin angular momentum, *S*, called *LS*-terms. The splitting of the *LS*-terms is shown in **Figure 2.3** [33]. *L* (or *S*) is at its maximum if the orbital angular momenta, (or spin orbital angular momenta) of the individual electrons are parallel. In the $4f^6$-configuration, *L* can range from 3 – 3 = 0 (yielding the S term*) to 3 + 3 = 6 (yielding the I term), while *S* can range from 3/2 – 3/2 = 0, if half the electrons spin opposite of the other half, to 6 × 1/2 = 3 (or -3), if all the spins are parallel. The *LS*-terms are split further apart by spin-orbit coupling.

Spin-orbit coupling arises from the fact that each electron has an intrinsic spin angular momentum in addition to an orbital angular momentum. This is the quantum mechanical equivalent to how a classical object like the earth rotates around its own axis as well as around the sun. As the electron is charged, and moving charges generate electric and magnetic fields, there will be two types of these fields and these fields interact, or couple. This coupling results in a splitting of the energy levels, which for lighter atoms is small, as the Coulombic interaction between each electron is much larger than the interaction between the electron intrinsic spin and the field generated by its orbit around the nucleus. The interaction can in this case be described by using what is called a Russel-Saunders coupling scheme, which is done by first summing the spins of all the electrons, *S*, and then the total orbital

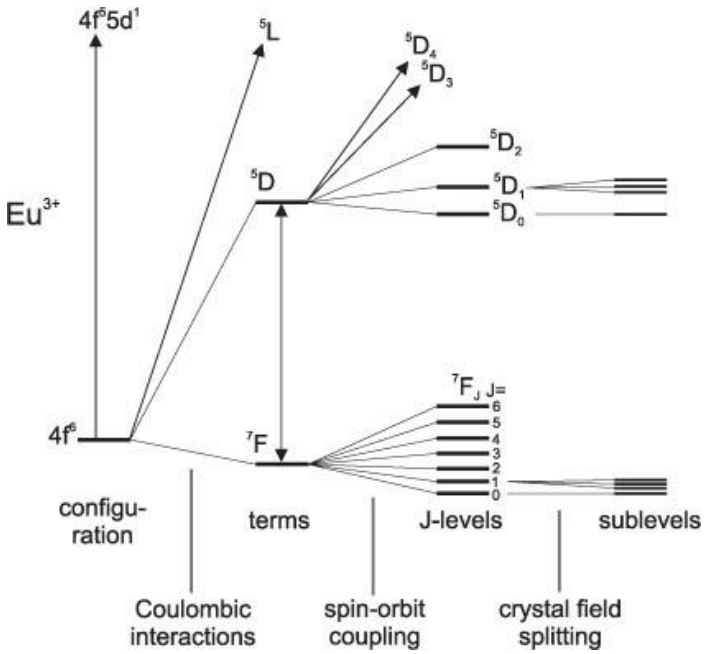

Figure 2.3: The $4f^6$ configuration of Eu^{3+} is 3003-fold degenerate to the zeroth order. Coulomb interaction splits the 3003 states in 7 *LS*-terms. Spin-orbit coupling and lifts the degeneracy. Each *J*-level is still 2*J*+1-fold degenerate, though, this degeneracy can be lifted by crystal field splitting, resulting in what is called Stark sublevels. Figure is modified and adapted from [33].

* Spectroscopic terms, L = 0, 1, 2, 3, 4, etc. are written as S, P, D, F, G and then continues alphabetically.

angular momenta, L, and then combining them. For heavier elements, however, the nucleus has a large charge and the interaction between each electron and its orbit becomes equally, or more significant than the electron-electron repulsion. To get the correct coupling in this case, it is necessary to first interact the spin, s, and the orbital angular momentum, l, of each electron, resulting in an individual angular momentum, j, for each electron. Summing up the j of each electron then gives the total angular momentum, J. This is called a j-j coupling scheme, which should be more appropriate for the lanthanides as they are heavy, but due to the poor penetration of the f electrons through the inner shells, they do not sample the high electric field at the nucleus and hence their spin-orbit coupling is in fact quite weak [34]. The quantum states of the lanthanide atoms and ions lie somewhere in between the two common cases, in what can be described as intermediate coupling states, which can be considered as combinations of several LS states [35]. In this scheme, the Coulombic and spin-orbital interactions are introduced simultaneously, which means that terms with the same J, but different L and S can mix. The effect of the mixing is relatively small on the energy of the levels, but can be significant on the optical transition probabilities between the levels. The spin-orbit coupling, albeit weak compared to non-RE elements with similar weight, still gives rise to excited states that are well separated from the ground states, which is why they are thermally inaccessible and ideal for electronic transitions. The crystal field only affects the energy levels very weakly.

Term symbols are used to describe energy levels and are defined as ${}^{2S+1}L_J$, where S is the total spin quantum number, L is the total orbital angular momentum quantum number and J is the total angular momentum of the energy level described by the spin-orbit coupling. The term ^{4}I refers to all the ${}^4I_J$ levels, which has a total spin of 3/2 ($2S + 1 = 4$), and a total orbital angular momentum of $L = 6$ (I-term). For lighter elements ($Z < 30$), this is sufficient to describe the energy levels, but for lanthanides the spin-orbit coupling further splits these levels apart and the J term is added. J can have the values $J = L + S, L + S - 1 \ldots |L - S|$, which in this case gives J = 15/2, 13/2, 11/2, and 9/2. In each level there is $2J + 1$ = n states, called Stark sublevels, which have the same total spin, total orbital angular momentum and total angular momentum, i.e. they are degenerate. When the atom is put into a crystal field, these states will split depending on the symmetry and chemistry of the neighbouring atoms. For lanthanides this splitting is small compared to the splitting between the levels, so even though optical absorption and emission takes place between states, it is more convenient to refer to the level the states belong to. As only the Stark sub levels are affected by the crystal field, not the J-levels, it means that the J-levels will always be at the same energy regardless of host structure. It is thus possible to construct what is called the Dieke diagram depicting all the J-levels of the trivalent lanthanide ions as shown in **Figure 2.4**.

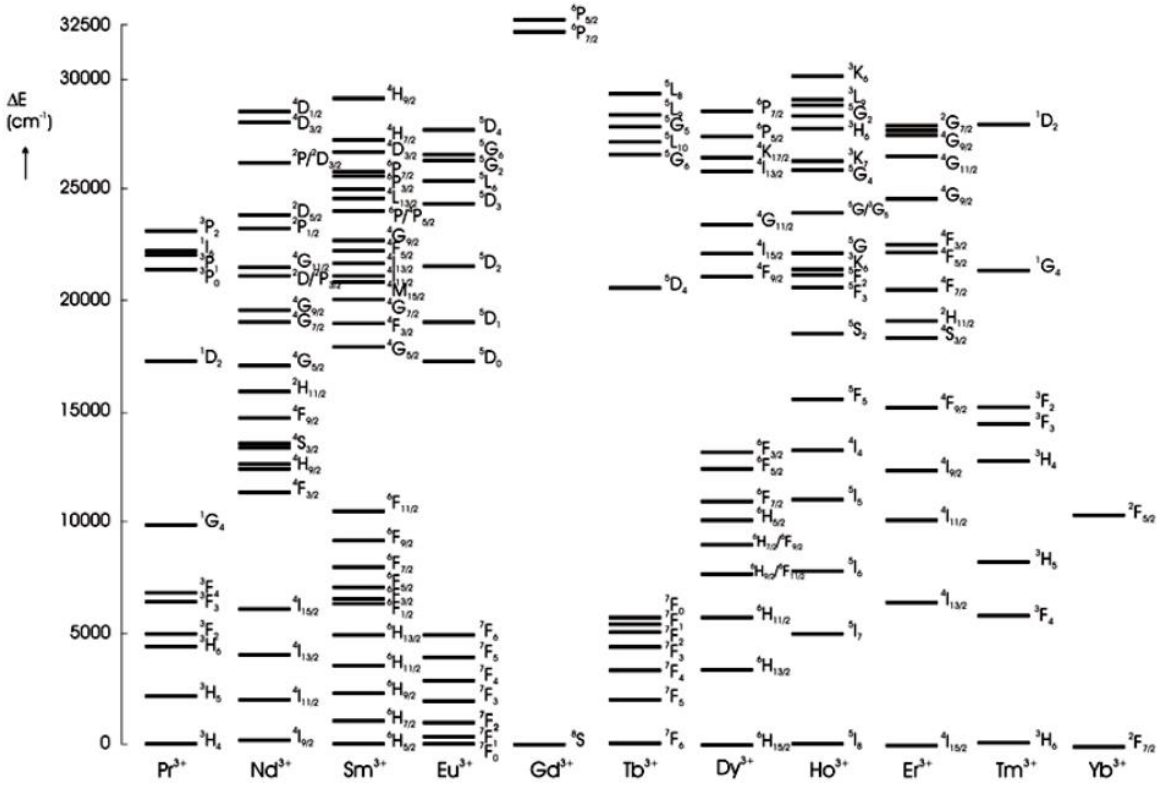

Figure 2.4: The Dieke diagram for a selection of optically active lanthanides in the range 0 - 32 500 cm^{-1}. Adapted and modified from [32].

2.4 Selection rules and intensities of electronic transitions

Electronic transitions follow certain selection rules, and transitions that do not follow these rules are forbidden on a quantum mechanical level. The basis for a spectroscopic selection rule is the value of the transition moment integral, measured by the transition dipole moment [34]:

$$M_{if} = \int \psi_f^* \mu \psi_i d\tau, \tag{2.4}$$

where $\boldsymbol{\psi_f}$ and $\boldsymbol{\psi_i}$ are the wave functions of the two states involved in the transition and μ is the transition moment operator. You may recall that $\boldsymbol{M_{if}}$ is used in Fermi's golden rule (Eq. 2.2) to describe the rate of spontaneous emission. The transition dipole moment can be regarded as a measure of the impulse that a transition imparts to the electromagnetic field, i.e. a large impulse corresponds to an intense transition, while zero impulse corresponds to a forbidden transition. In the hydrogen atom for instance, an excitation of the electron from 1s to 2s would not change the electric dipole of the atom as the s-orbitals are symmetric and the charge is evenly distributed and has the same distribution before and after the excitation

takes place. Since the dipole moment remains unchanged, the transition moment integral becomes zero and the transition is consequently forbidden. A transition from 1s to 2p on the other hand would change the dipole and this transition would consequently be allowed. In general the transition is forbidden when the transition moment function, $\boldsymbol{\psi}_f^* \boldsymbol{\mu} \boldsymbol{\psi}_i$, is odd or antisymmetric, i.e. when $\boldsymbol{y}(\boldsymbol{x}) = -\boldsymbol{y}(-\boldsymbol{x})$ holds. As such, it is enough to determine the symmetry of the transition moment function to determine whether a transition is allowed or forbidden. The symmetry of the function is the direct product of the parities of its components, and is typically found in standard character tables. The parity of an orbital is labelled *g* (*gerade*) if it is symmetric under inversion or *u* (*ungerade)* if it is not. For electrons in atomic orbitals, the interactions with the field are mainly due to electric dipole transitions. For these interactions, the operator $\boldsymbol{\mu}$ has odd parity, *u*, as the dipole moment changes sign under inversion, resulting in the product of the components of the transition moment function becoming odd for transition between orbitals with the same parity, i.e, $\boldsymbol{g} \times \boldsymbol{u} \times \boldsymbol{g} = \boldsymbol{u}$ and $\boldsymbol{u} \times \boldsymbol{u} \times \boldsymbol{u} = \boldsymbol{u}$. As the resulting intensities are zero for antisymmetric transition moment functions, the resulting transition is electric dipole forbidden. Similarly, electric dipole transitions between orbitals with different parity are allowed as $\boldsymbol{g} \times \boldsymbol{u} \times \boldsymbol{u} = \boldsymbol{g}$. It follows that s-s, p-p, d-d, or f-f, transitions are forbidden, whereas s-p, p-d, and d-f transitions are allowed as s-orbitals have *g* symmetry, p-orbitals and *u* symmetry, d-orbitals have *g* symmetry and so on and so forth. This is called the Laporte selection rule and also carries over to complexes with a centre of inversion, like octahedral complexes, where transitions between e_g and t_{2g} molecular orbitals are $g \leftrightarrow g$ and therefore forbidden. Complexes with no centre of inversion, like tetrahedral complexes, do not have any *g* or *u* subscript and the Laporte rule has usually significantly lower impact on the electronic transition rates in this case.

Another electronic selection rule that is a consequence of the transition moment integral is the spin selection rule. The wave function of a single electron is the product of a space-dependent wave function and a spin wave function. As spin is directional and can be said to have odd parity, and since the transition dipole moment operator acts only on the spatial part of the wave function, not the spin (ignoring spin-orbit coupling), the electromagnetic radiation is not able to interact with the spin of an electron, so the spin cannot change. It follows that transitions in which the spin changes direction are forbidden. For a transition to take place, ΔS for the transition must be zero, e.g. a singlet (S = 0) state cannot undergo a transition to a triplet (S = 1) state. If spin-orbit coupling is taken into account, then the singlet state has the same total angular momentum as the triplet state so the two states can interact. A small amount of singlet character in the triplet state leads to a transition moment integral that is non-zero, so the transition is weakly allowed.

As discussed previously, the optically active transitions in lanthanides are mostly intraconfigurational f-f transitions and are consequently forbidden. The question that arises is why do these transitions still occur? While the crystal field interacts only weakly with the f-orbitals due to the small radial extent of the f-orbitals, the effect is still enough to cause a slight departure from the perfect centrosymmetry, particularly for highly asymmetric structures. For transition metals, this distortion is much stronger and d-d transitions are consequently much stronger than f-f transitions. For heavy lanthanides, like ytterbium, the lanthanide contraction forces the f-orbitals to slightly penetrate the outer orbitals, which make them more susceptible to the crystal field, e.g. the f-f transition rates in Yb^{3+} are typically much higher than the f-f transitions in Eu^{3+}. It is also possible for the electronic states in lanthanide or transition metal ions to mix with vibrational states with different parity, which temporarily destroys the centre of inversion and thus relaxes the Laporte rule, with the result that at a given point in time there will be some ions where f-f or d-d transitions may occur. If these transitions are the only ones possible, then they will dominate the absorption and emission properties of the material, even though they are forbidden. Both of the effects that allow for f-f transitions to take place depend on the host material, which thus has a large impact on the transition rates in lanthanide ions.

2.5 Effect of the host material

As mentioned previously, the host material has no effect on the *J*-levels of the trivalent lanthanides shown in the Dieke diagram (**Figure 2.5**). However, the host does have a slight effect on the shape of the f-orbitals and can thus have a significant impact on the transition rates, i.e. the transition rate may go from zero to some non-zero value. The presence of a host material also enables transitions of luminescent centres to couple to vibrations. The crystal field has a negligible effect on the f-orbitals compared to s, p and d, but it still slightly deforms the orbitals so that some of them will be slightly closer to, or further from the core. For s, p and d-orbitals, the excitation of an electron also leads to a change in bonding between the ligands and the central atom. The excited state will consequently have an equilibrium positions that is either closer to, or further away from the core than the ground state. As any deviation, from the equilibrium position leads to a higher energy of the system, the associated energy potential is in a first-order approximation harmonic, i.e. the energy is a function of the square of the deviation from the equilibrium position, ΔQ_e, resulting in the parabolic bands shown in **Figure 2.6**. This kind of diagram is called a configurational coordinate diagram and plots the energy of the various bands against nuclear coordinates. As an electronic transition takes place rapidly compared to the motion of the nucleus, it follows

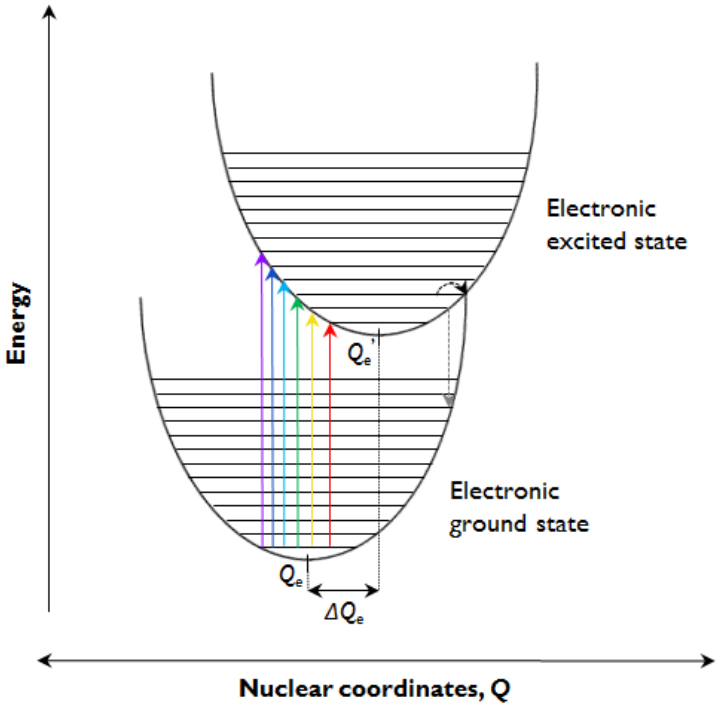

Figure 2.6: A configurational coordinate diagram of an f-d transition, where the separation between the luminescent ion and the anion ligand is increased in the excited state, resulting in the potential energy curve of the electronic excited state being shifted ΔQ_e relative to the ground state. The equilibrium positions of the electronic ground and excited states are denoted Q_e and Q_e', respectively. The upward arrows show possible transitions leading to the absorption of a photon. The reverse process would lead to the emission of a photon (not shown). The grey dotted arrow indicates the point at which phonon emission becomes dominant over photon emission, depending on the energy of the phonons in the material. The black dotted arrow indicates the point where excited electrons may cross over to the ground state directly.

that the nuclear coordination does not change notably during an electronic transition (Frank Condon principle). This means that the electron will be excited to a position that is higher in energy than the equilibrium position of the excited state. If the electron is to reach the equilibrium position of the excited state, it needs to get this momentum by emission of lattice vibrations, called phonons, which carry both momentum and small amounts of energy (compared to photons). The electronic transition thus couples to vibrations, which results in the maximum of the absorption and emission bands to be separated. This is called a Stokes shift if the emitted photon has less energy than the one that was absorbed, or anti-Stokes if the emitted photon has more energy (e.g. some phonons were absorbed during the process). As phonons are quantized the energy of the vibrational states can be described by $(n+1/2)\hbar\omega$, where n is the vibrational quantum number, and $\hbar\omega$ is the energy of the vibrational mode. Emission from n=0 is called the zero-phonon line. At cryogenic temperatures in high quality crystals, it is sometimes possible to observe the lines corresponding to different vibronic

transitions, due to low amount of phonons. At increasing temperatures, however, the lines broaden and start to overlap and the fine structure disappears, resulting in broad emission and absorption bands. The vibrational excited states are filled corresponding to the Boltzmann distribution, i.e. the number of electrons in a given state is proportional to $e^{-\frac{E}{kT}}$, where E is the energy of the state and k is the Boltzmann constant. Increasing temperatures thus causes the higher energy states to fill up. **Figure 2.6** also shows that if the geometry of the excited state differs from the ground state, the parabolas will intersect at some point, allowing excited electrons to cross over to the ground state non-radiatively, indicated by the black dotted arrow.

The displacement between the ground and excited state, ΔQ_e, depends on the flexibility of the structure and the influence on the chemical bonding between the ion and the surrounding ligands. As the shielded 4f-electrons of the trivalent lanthanides do not participate in the bonding, it follows that ΔQ_e for the f-orbitals must be small, much smaller than depicted in the configurational coordinate diagram in **Figure 2.6**, which means that the parabolas can be considered to be more or less directly above each other. The shielding also means that the 4f electrons are protected from the lattice and consequently couple only weakly to phonons. Their Stokes shift is thus negligible, and their luminescence spectra are dominated by sharp zero-phonon line emission even at room temperature. Luminescence in the trivalent lanthanides can in fact take place at well above 1000 °C in certain host structures [36, 37]. As only very specific wavelengths can be absorbed and emitted, and as the absorption process is also forbidden, it means that most lanthanides are very poor at absorbing the broad light spectrum produced by the sun. As such, it is common to separate the absorption and emission process when using lanthanides as light converters, by using a different material that excels at absorbing, like Bi^{3+} or Ce^{3+}, as either the host or by co-doping. For instance in YVO_4: Eu^{3+}, the $(VO_4)^{3-}$ will first absorb the photon and the energy is consecutively transferred to Eu^{3+}, where radiative emission is the dominating decay process. Electrons in states that are lower in energy of where the parabolas intersect might also decay non-radiatively, depending on the phonons in the material. If the energy difference between the vibrationally excited ground states and excited states is small enough to be bridged by 5 or less phonons, phonon emission will dominate the decay of the excited state. This is signified by the grey arrow in **Figure 2.6**. The energy of the phonons in the host matrix can therefore have a large impact on the decay mechanism in the material. **Table 2.1** shows the maximum phonon energies present in some common host matrices. These materials generally have low phonon energies and are thus suitable as hosts for luminescent materials. For YVO_4 for instance it follows that transitions with $\Delta E < \sim 4500$ cm^{-1} (~2200 nm), are quenched by phonons, i.e. the relevant emission in the visible or NIR is not quenched.

Table 2.1: Maximum phonon energies of some common host matrices [38, 39].

Material	Phonon energy (cm^{-1})
Silica glass	1100
$LaPO_4$	1050
YVO_4	890
$YAlO_3$	600
Y_2O_3	550
$NaYF_4$	350

2.6 Energy transfer and up and downconversion

Energy can be transferred between an excited absorber, acting as an energy donor, and a nearby species, acting as an energy acceptor, in various ways depending on the energy level structure of donor and acceptor. In almost all cases, energy transfer requires that the emission spectrum of the donor must at least partially overlap with the absorption spectrum of the acceptor. The strongest transitions, i.e. the transitions with the largest probability of taking place, are usually electric dipole transitions, where the electric dipole of the donor couples to the electric dipole of the acceptor, resulting in a dipole-dipole coupling that has a transfer rate proportional to the inverse sixth power of the donor-acceptor separation. Energy transferred in this way is called *Förster type* [40], and is the most common type of energy transfer. Note that this energy transfer is non-radiative. There are no photons involved; although the process is often described using virtual photons that are instantly absorbed by the accepting species as shown in **Figure 2.7**. As the Förster energy transfer rate is extremely sensitive to the distance, a convenient parameter to describe the strength of the energy transfer of a particular donor-acceptor couple is the critical Förster radius, R_0. It is defined as the separation between donor and acceptor at which energy transfer has the same rate as intrinsic decay of the donor, i.e. the separation at which the energy transfer rate is 50%. R_0 depends on the quantum yield of the donor in the absence of an acceptor, which for lanthanides is very low due to the f-f transitions being forbidden. Typical values of R_0 for lanthanides are thus only a few angstroms [41]. Due to the inverse sixth power dependence, donor-acceptor distances below R_0 result in very efficient energy transfer, while the energy transfer becomes negligible very quickly above R_0. In order for first-order energy transfer to take place between lanthanides, they must thus fulfil the two conditions for Förster energy transfer, i.e, the emission spectrum of the donor must overlap with the absorption spectrum of the acceptor, and the distance between them must be on the order of R_0 or less. This gives rise to several transfer mechanisms, some of which are shown in **Figure 2.7**.

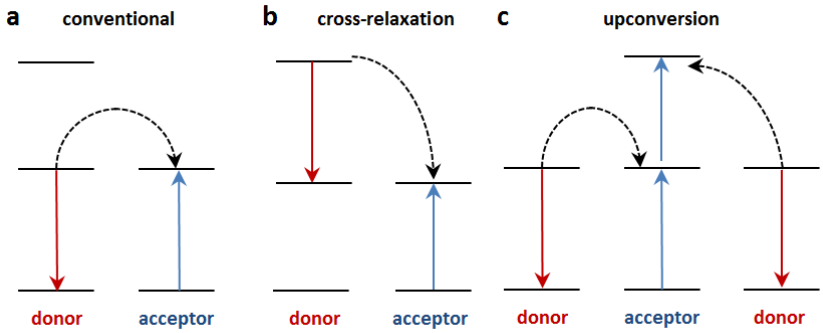

Figure 2.7: Various types of Förster energy transfer processes. Note that no photons are involved in these processes. (**a**) The most common type of energy transfer. An excited donor relaxes to its ground state by transferring its energy to the acceptor, which then gets excited. (**b**) The donor is initially in an excited state, but instead of relaxing to the ground state, it relaxes to an intermediate energy level and thus only part of its excitation energy is transferred to the acceptor. (**c**) A conventional energy transfer to a metastable intermediate state, followed by an additional energy transfer from another donor, resulting in the energy of two low-energy photons being transferred to a single acceptor. The process yields a high energy upconverted photon if the final excited state of the acceptor is emissive.

Another thing we can take from this is that if several luminescent centres with a similar energy level structure are separated less than R_0 apart, the energy can migrate efficiently between them until a quenching site is found, typically in the form of a defect, as shown in **Figure 2.8**. This is called *concentration quenching*, as the distance between the luminescent atoms decreases with increased concentration. As such, it is usually not possible to have more than a few percent of lanthanides acting as luminescent centres in a given

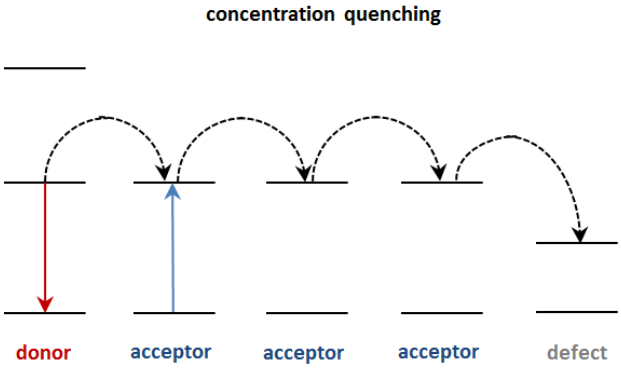

Figure 2.8: A donor transfers its energy to an acceptor who consecutively transfers its energy via Förster energy transfer to other acceptors separated within the Förster radius until a defect site, like an impurity is reached. This is called concentration quenching as the distance between the acceptors typically depends directly on the concentration, although the effect also depends on the lifetime of the excited state and the number and kinds of impurities in the material.

material, as higher concentrations decreases the average distance below R_0, manifesting as a significant drop in the emission.

It was earlier stated that in order for Förster energy transfer to take place, the emission spectrum of the donor and the absorption spectrum of the acceptor must overlap. However, should the overlap between donor emission and acceptor absorption be absent, it is still possible for Förster energy transfer to take place if the sum of two or more acceptors equals the energy of the emission of the donor. In this case, second-order *downconversion* may become the dominant relaxation process, competing with spontaneous emission [42]. Energy transferred in this way is called cooperative energy transfer (CET), as two or more acceptors cooperate to absorb the energy. An example of this process is the Tb^{3+}-Yb^{3+} pair, where the $^5D_4 \rightarrow {}^7F_6$ transition of Tb^{3+} is located at around twice the energy of the Yb^{3+} $^2F_{7/2} \rightarrow {}^2F_{5/2}$ transition and occurs with a transfer efficiency of 88% for the $YbPO_4$: 1% Tb^{3+} system [42]. In principle, this allows for a quantum efficiency of 188%, as 88% of the excited electrons result in two photons, while the remaining 12% provide one. In practice this is not observed, and in order to achieve this, a high Yb^{3+} concentration would be required (99 mol% was used in this study). The average distance between a Tb^{3+}-ion and an Yb^{3+} should be small, maximizing the chance that an excited Tb^{3+} ion would find two Yb^{3+} ions to which it can transfer its energy. With an Yb^{3+} concentration of 99 mol%, the average Yb^{3+}-distance becomes much shorter than R_0, resulting in severe concentration quenching. The fact that both Yb^{3+} and Tb^{3+} are prone to concentration quenching, means that it is challenging to find concentrations of each so that energy transfer between them is efficient, while energy transfer between two Yb^{3+} or two Tb^{3+} is not. In this thesis, we investigate the use of a $(VO_4)^{3-}$ donor that is a strongly absorbing material while also having an emission band at twice the energy of the Yb^{3+} $^2F_{7/2} \rightarrow {}^2F_{5/2}$ transition, potentially allowing for second order CET with decent efficiency.

First order downconversion, as shown in **a** and **b** in **Figure 2.9**, are also possible methods of obtaining quantum efficiencies above 100%, and will dominate over second-order cooperative downconversion where present. An example of this is the Pr^{3+}/Yb^{3+} couple, where mechanism **b** was determined to be the dominant decay process by Wijngaarden *et.al.* [43]. The mechanism shown in **a** is very efficient, but has so far only been realized for photons outside the solar spectrum [44]. As it has been shown that Förster energy transfer between one donor and two acceptors is possible, it also follows that the opposite process is possible, i.e. upconversion (see **Figure 2.7c**). Upconversion does, however, require high photon densities and it is consequently quite challenging to enhance the efficiency of solar cells cost efficiently by this method. For this reason, upconversion was not the main objective in this research and will not be explained in further detail in this thesis.

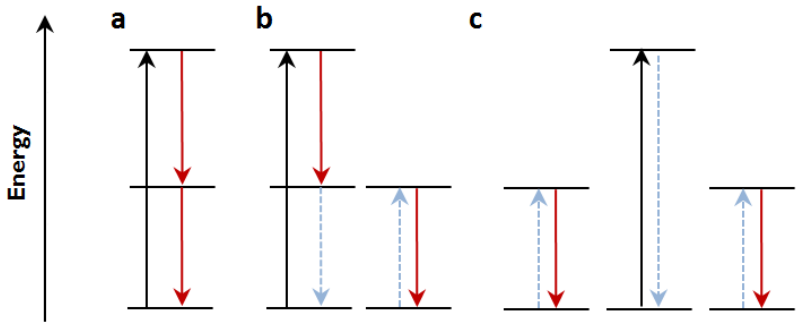

Figure 2.9: Possible downconversion processes. Black arrows indicate absorption, while red arrows indicate photon emission, while blue dotted arrows indicate energy transfer processes. (**a**) A high-energy photon is absorbed by an electron, which first relaxes to an intermediate state by emitting a low-energy photon, before relaxing to the ground state by emission of another one. (**b**) Similar to (**a**), but when the electron reaches the intermediate state, the energy is instead transferred via cross-relaxation to an electron on a different ion, who then relaxes by emitting a low-energy photon. (**c**) A high energy photon is absorbed followed by cooperative energy transfer to two nearby ions, who then relax to the ground state by emission of two low-energy photons.

A type of energy transfer not mentioned so far is Dexter energy transfer, also known as collisional or short range energy transfer. In this process, the excited electron of the donor moves directly to a vacant excited state of an acceptor, while a ground state electron of the acceptor moves to the vacant ground state of the donor. This process not only requires spectral overlap, but also requires that the wave functions of the involved orbitals overlap, which usually only happens during the collision between molecules. This type of energy transfer is thus unlikely to take place for lanthanides due to the shielding of the f-orbitals. Energy transfer to and from lanthanides is thus considered to be primarily Förster type.

Chapter 3 – Atomic layer deposition

There are several methods to produce light converting layers for solar cells and other applications. The atomic layer deposition (ALD) technique is one of them and was originally developed for industrial production of thin film electroluminescent displays in 1974 [45-47][*]. It is still used for this purpose today. The list of applications has since increased, particularly within microelectronics, where it is used for deposition of high-k dielectrics, metallization, and MEMS devices [48]. Other applications include material enhancing layers, such as moisture barrier coatings [49] and corrosion protection [50].

3.1 Basics of the ALD processes

While ALD is a unique deposition technique, it is still considered a subclass of chemical vapour deposition (CVD), as opposed to physical vapour deposition (PVD), as the process relies on chemical vapour reactions. In CVD, volatile materials used for the deposition, called precursors, are introduced simultaneously in the reaction chamber, and parameters such as temperature and pressure are controlled to limit gas phase reactions in favour of reactions or decompositions on a substrate surface. In ALD, the precursors are fully separated, usually in time, but sometimes also in space so that there is no possibility of the precursors to react with each other in an uncontrolled manner. This makes it possible to use extremely reactive precursors, which can react at temperatures as low as room temperature [51], although most processes are performed between 100-400 °C, and some can be run at much higher temperatures. CVD processes on the other hand typically run at 500-1000 °C, so the low temperatures used in ALD enables use of substrates such as plastics, polymers and textiles that do not withstand high temperatures.

After a precursor is pulsed into the reaction chamber, it will immediately react irreversibly with all surfaces in the chamber until all active adsorption sites are saturated. If the temperature is low enough, the precursor will not decompose or react with its own surface species and the growth is thus self-limiting to one mono-layer. The chamber is then

[*] ALD was in fact developed independently by Tuomo Suntola in 1974, who patented it [45] and by Aleskovskii *et al*. who presented the technique under the name “Molecular Layering” at a conference in the Soviet Union in the 1960s [46][47].

flushed with an inert gas, typically nitrogen, in order to purge away excess precursor or gaseous by-products. A second precursor is pulsed in once the chamber has been flushed and this will again react with the surfaces in the reaction chamber until all the active adsorption sites are saturated, after which the chamber is purged again. The first precursor will typically be a molecule containing a metal cation coordinated to some ligands, while the second precursor will usually be a molecule that contains the anion, for instance water or ozone for deposition of oxides, ammonia for deposition of nitrides or trimethylphosphate (TMPO) for deposition of phosphates. The sequence of cation precursor/purge/anion precursor/purge, is called an ALD-cycle, and this cycle can be repeated over and over until the desired thickness is reached, as the number of adsorbed precursor molecules on the surface is constant for a given temperature at ALD-conditions, and thus the growth rate per cycle is constant. The process is shown in **Figure 3.1.**

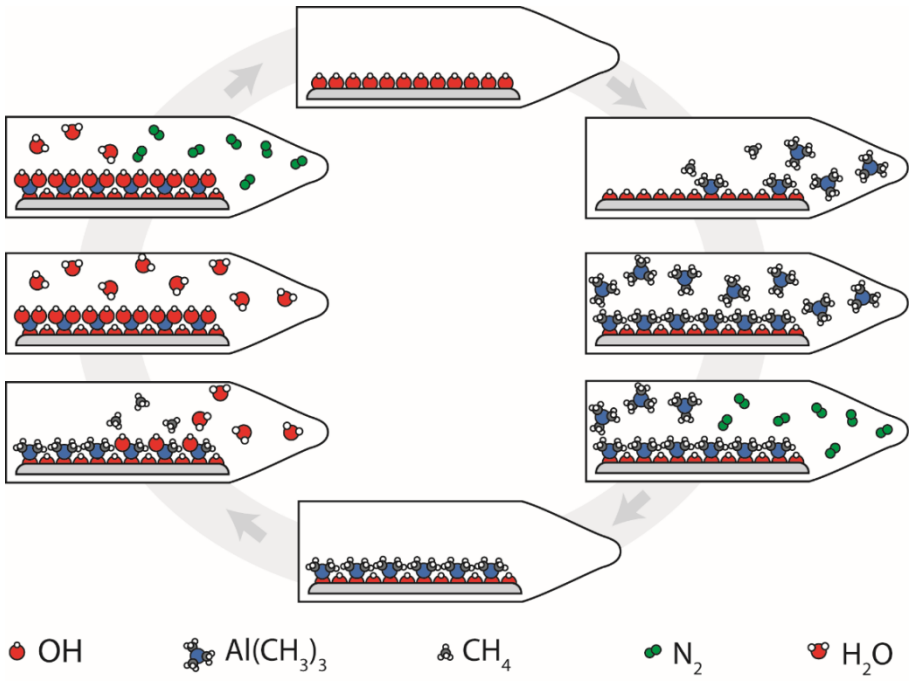

Figure 3.1: Illustration of an ALD-cycle using the $AlMe_3$-H_2O process. Adopted from [52].

3.2 Multicomponent films

Films containing more than two elements can also be deposited by combining sub-cycles of the desired elements. For instance a mixture of V, Y, Yb, and O can be made by repeating the pulse sequence: $VO(thd)_2/O_3/Y(thd)_3/O_3/Yb(thd)_3/O_3$, with purges between each precursor pulse. The stoichiometry can be controlled through the combination of the individual sub-cycles, although, a direct transferral of the pulsed composition to the deposited stoichiometry is not necessarily expected [53].

One of the challenges with films containing numerous elements is to find a temperature where all the reactions that take place are self-limiting. In order for self-limiting reactions to take place there can be no side reactions, such as etching, precursor desorption or thermal decomposition of the precursor. The temperature window where clean self-limiting reactions dominate is called the "ALD-window". The growth rate is usually only weakly temperature dependant in this temperature range, which is in contrast to regular CVD processes that are strongly temperature dependent or dependent on the flux of precursors. The "ALD-window" of multicomponent processes may differ from that of the individual binary processes, e.g. a multicomponent system consisting of binary systems with ALD-windows in the 200-250 °C range may display self-limiting growth beyond this range [53].

Another challenge with films containing more than two elements is controlling the composition and thickness, as the growth changes depending on the surface that is being deposited on, e.g. the growth rate of V_2O_5 is slightly different on an Y_2O_3 surface than on a V_2O_5 or Yb_2O_3 surface. Also, if one of the desired components in the film needs to be in a lower oxidation state, then this can restrict the use of oxidizing precursor like O_3 for other components in the film. For each precursor added there are more parameters that can be adjusted, making ternary, quaternary or even higher order systems thus quite challenging to deposit. In general, deposition of binary compounds is by far the most common, though the number of different materials that have been deposited by ALD is increasing rapidly and almost any class of material can be made. An overview of possible ALD-processes and materials made up to 2010, as well as a general overview of the field can be found in the review article by Miikkulainen *et al.*[48].

3.3 Advantages and drawbacks of ALD

The ALD technique is capable of highly reproducible conformal films regardless of equipment type and vendor. This means that the growth rate of a certain compound for a certain temperature should be universal. However, many ALD-processes are not perfectly ideal, e.g. some precursors may react partly reversibly or some irreversible decomposition may take place. Some by-products may also not be completely inert, but may react with the precursor or adsorb to the surface, blocking further growth. ALD-processes are also considered relatively slow, being the main disadvantage of the technique. As only one mono-layer of precursor is deposited at a time, the thickness grown per hour will depend on the size of the precursor molecule, the number of active adsorption sites and the length of the pulse and purge times, which typically are in the order of seconds. Growth rates are typically in the range of 0.1-2 Å per cycle, with a cycle in the range of ca. 1-30 seconds. For this reason, it is also often accepted to have a surface saturation slightly below 100%, and the unreacted reactant to be purged to 0.01% of the original concentration in order to save time [48]. All

things considered, ALD-processes are usually not 100% reproducible between research groups, but are usually very close.

A slow deposition rate, as compared to other deposition techniques, is not necessarily a problem on an industrial scale, as the ALD technique offers high precision and possibilities for batch processing, as exemplified earlier in the case of wafers for the solar cell industry.

An advantage of the purge-step in ALD is that there are no gas-phase reactions. The films will thus be particle free as any particles already on the surface will be covered by the film, resulting in pinhole free films. This is particularly important for applications such as dielectrics or battery electrolytes, where pinholes causes short circuiting or self-discharge. The self-limiting growth also means that it is possible with most precursors to achieve conformal growth across surfaces with high aspect ratios, such as structures with trenches, or textured surfaces, like the surface of a silicon solar cell. Some precursors, like ozone, do not necessarily survive multiple collisions with a surface on its way down a trench and could partially decompose into O_2. So there is usually a limit to the kind of surface where conformal growth can be achieved, but this is still often the most important reason for using ALD for a specific process.

Due to the precise thickness control and great conformality available with ALD, it is possible to deposit layered materials with very thin layers. This is useful for a wide range of applications, and could potentially also be of interest for luminescent materials as it could allow for engineering of materials similar to core-shell nanoparticles where emitter and absorber can be separated by a layer that prevents charge-transfer directly between them [54-56]. Energy transfer between Ce^{3+} and Yb^{3+} is for instance bridged by a first-order Ce^{4+}-Yb^{2+} charge transfer state [57], quenching the second-order cooperative downconversion for this system. By separating these ions by a Tb^{3+}-layer, however, it should be possible to force energy transfer to go via Tb^{3+}, and as discussed in chapter 2, the energy transfer between Tb^{3+} and Yb^{3+} has been shown to be dominated by second-order CET. For efficient energy transfer to take place, these lanthanide ions do, however, require non-centrosymmetric crystalline host materials. Samples grown with ALD can be either crystalline as deposited or amorphous, and due to the low temperature of ALD-processes they are usually amorphous, particularly for multicomponent materials. Amorphous films can be subjected to post deposition annealing in order to obtain crystalline films. However, the layers of a layered film might be destroyed by annealing at high enough temperatures for crystallinity to be induced, which thus is a serious problem for this kind of material. These challenges can be overcome by achieving epitaxial growth, which requires the right pulse ratio of the various components so that the correct stoichiometry can be achieved, combined with a sufficiently high deposition temperature. Sometimes epitaxial growth can be induced by depositing on a crystalline substrate with the desired crystal structure. Utilizing nanostructuring to control physical

interaction on an atomic scale is still in the early stages, and determining growth rates and optimizing conditions for known systems needs to be done before more advanced materials can be realized.

3.4 ALD of lanthanide-based luminescent materials

As thin films made by ALD have been used in electroluminescent displays since the conception of the technique, a wide range of luminescent materials have been deposited, including several using lanthanides. At this point, all the stable binary oxides of lanthanides have been deposited with ALD [58]. The most commonly used precursor is the Ln(tris(2,2,6,6-tetramethyl-3,5-heptanedionato))$_3$/O_3 pair. Ln(thd)$_x$ is a β-diketonate and is stable at room temperature and most of them sublimate between 115-200 °C and can be deposited between 200-350 °C, making them easy to handle and also suitable for ALD. The carbon content at optimized temperatures for the Ln(thd)$_x$/O_3 processes typically ranges from 1-5 at%, while the hydrogen content ranges from 1-2 at%, though some processes, like La_2O_3, deviate markedly from this with carbon content at 10-12 at% [59]. While relatively pure RE oxides can be produced by using β-diketonate precursors, a significant drawback of this kind of precursor is that the growth rates for the oxides is rather low due to the large size of the thd-ligand and low reactivity of lanthanide compounds. Typical growth rates obtained are in the range of 10-40 pm/cycle [59, 60]

ZnS:(Ce, Tb, Eu, Tm) was among the first classes of materials deposited by ALD [61], while more recently, ALD has been used to make thin-films of Er^{3+} containing oxides as optical gain media in Er_2O_3 [62], Y_2O_3 [63, 64] and Y_2O_3:Er^{3+}, Yb^{3+} [65] or as upconverters [66, 67]. Of particular interest for this thesis was the study by Hansen *et al.* [25] on the Eu_2O_3-TiO_2 system. The results showed that this system displays significant luminescence as deposited, even though the films are amorphous. Upon annealing the samples at higher temperatures the luminescence efficiency decreases, most likely due to increased symmetry around europium. It was also determined that up to ten consecutive pulses of Eu(thd)$_3$/O_3 could be deposited between the same amounts of $TiCl_4$/H_2O cycles before the luminescence efficiency decreased. While samples made by ALD are expected to have more defects than a crystalline bulk material, it could still be that the layered nature of the technique allows for higher concentration of luminescent centres before the average distance between them becomes short enough for concentration quenching to become dominant. In bulk materials, the lanthanide ions are randomly distributed throughout the sample, while in ALD they have defined positions as deposited and then migrate from these positions upon annealing. The distance between the acceptor-emitter and emitter-emitter distances will be different in bulk than in thin-films made by ALD, and determining how this affects the luminescence in various systems is thus of interest.

Chapter 4 – Experimental methods

In this chapter, the various characterization techniques used during the experimental work will be explained briefly. This section will outline the principles of the various methods so the reader can achieve a basic understanding of the techniques and why they were used during the work with the thesis, but they will not be explained in detail. For a more thorough description of the various techniques the reader will be referred to dedicated books or articles on the subject. Instrument specific details of each experiment or measurement are presented in the experimental section of the respective papers.

4.1 Photoluminescence

In photoluminescence spectroscopy (PL) the excitation wavelength is fixed, while the detector records the photons emitted by the sample at different wavelengths, as shown in **Figure 4.1**. This technique gives information about the position of bands between which electronic transitions occur radiatively. For Eu^{3+} for instance, the transition from the $^5D_0$ level to the ^7F_J-manifold is radiative and can thus be detected. The technique is often used for determining the band gap of semiconductors or to detect impurity levels or defects from which radiative relaxation may occur. For additional information about the technique the reader is referred to references [68-70].

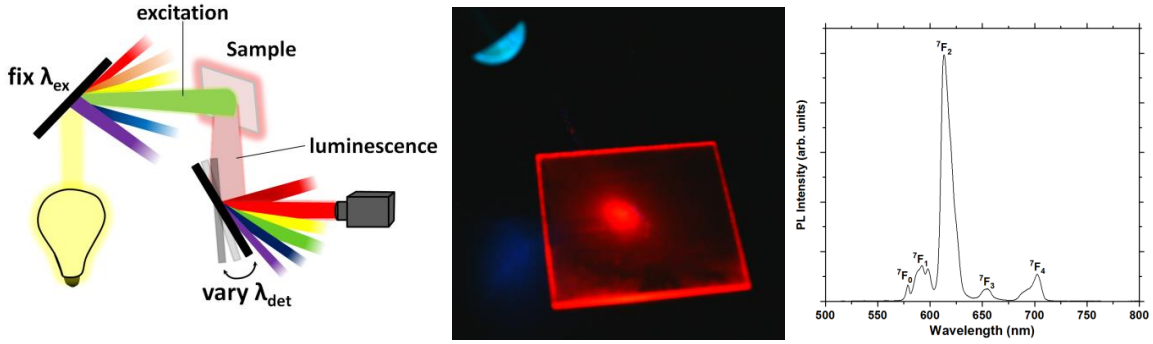

Figure 4.1: Setup for emission spectroscopy (left). The sample is excited with light of a fixed excitation wavelength, λ_{ex}, and the luminescence intensity is measured as a function of detection wavelength, λ_{det}. The image in the middle shows a photograph of an amorphous Eu-Ti-P-O sample excited by a UV diode, while the figure to the right shows the corresponding emission spectrum resulting from transitions from the $^5D_0$ level to the various ^7F_J-states of Eu^{3+}.

4.2 Photoluminescence excitation

Photoluminescence excitation spectroscopy (PLE), the excitation wavelength is varied, while the detected wavelength is fixed. This gives information about transitions leading to certain kinds of emission. In the case of EuTiPO, by tracking the 613 nm emission of Eu^{3+} while varying the excitation wavelength, it becomes evident that the 613 nm emission originates from a broad absorption in the UV, like a charge transfer absorption in the $(TiO_6)^{8-}$ complex, while a small amount originates from narrow absorption bands due to direct excitation of Eu^{3+}, as shown in **Figure 4.2**. For additional information about the technique the reader is referred to reference [70].

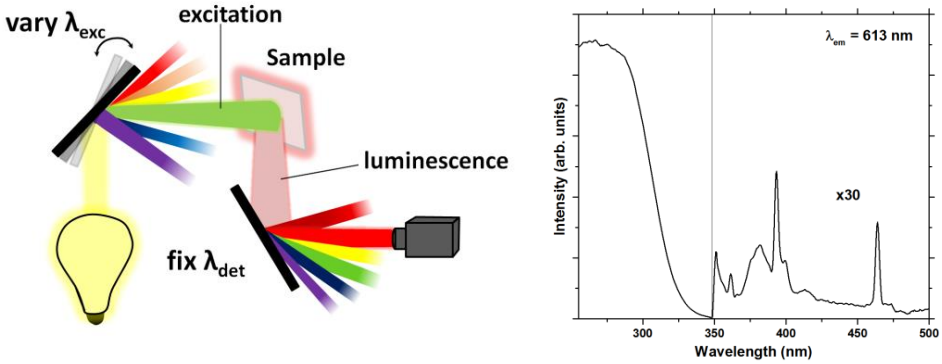

Figure 4.2: Setup for excitation spectroscopy (left). The luminescence intensity of the sample is measured at a fixed detection wavelength, λ_{det}, while varying the excitation wavelength, λ_{exc}.

4.3 Absorption spectroscopy

Absorption spectroscopy, also called UV-Vis spectroscopy when performed in the UV or visible, is used in order to determine the transmission and reflectivity of the sample at certain wavelengths. This is done by varying the incident wavelength while detecting the transmitted (**Figure 4.3**) or scattered and reflected light, usually by using an integrating sphere. The light that is not detected by either of these two measurements is consequently absorbed by the sample. For additional information about the technique the reader is referred to reference [71].

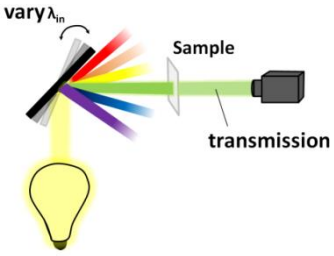

Figure 4.3: Setup for transmission spectroscopy. Transmission spectra are recorded by measuring the transmission of light with varying wavelength, λ_{in}, through the sample.

4.4 Photoluminescence decay measurements

In order to gain information about the lifetime of the excited state, it is possible to use photoluminescence decay measurements. In these measurements a fixed excitation wavelength is used, and the emitters are brought into the excited state by a short laser pulse. After the short pulse, the excited electrons will relax to the ground state and emit photons that can be detected. The point in time they are detected after the pulse thus equals the time spent in the excited state, i.e. the lifetime, for the particular electron that produced the detected photon. Emitters will typically have two or more competing pathways that the excited state can decay by in order to reach the ground state, e.g. radiatively and non-radiatively. While only the radiative process can be detected, it is still possible to obtain information about the non-radiative process, as the number of photons emitted per unit of time, $\Phi(t)$, will depend on the rate of the different processes. If there is only one radiative decay pathway and dp_{rad} is the probability of that decay process occurs during the time interval between t and $t+dt$ and $N(t)$ is the number of excited emitters at a delay time t after a lase pulse, the photon emission rate is given by:

$$\Phi(t) = \frac{dp_{\mathrm{rad}}}{dt} = \gamma_{\mathrm{rad}} N(t) = \gamma_{\mathrm{rad}} N(0) e^{-\Gamma t}, \tag{4.1}$$

where Γ is the total decay rate of the excited state and thus depends on all radiative and non-radiative decay rates. By comparing two samples, it is thus possible to tell from differences in $\Phi(t)$ the relative rate of the different decay pathways. This also means that it is possible to determine the energy transfer rate from one emitter acting as the donor (e.g. $(VO_4)^{3-}$) to another emitter acting as the acceptor (e.g. Yb^{3+}), by measuring the emission of photons by donors for various samples and comparing the results to a reference measurement without the acceptor present (e.g. YVO_4).

If the sample contains emitters that emit at the same wavelength, but with unequal exponential decay rates, Γ_1 and Γ_2, like Eu^{3+} ions in two different chemical environments for instance, the experimental PL decay curve will be biexponential:

$$I(t) \propto \Phi_1(t) + \Phi_2(t) = \gamma_{\mathrm{rad},1} N_1(0) e^{-\Gamma_1 t} + \gamma_{\mathrm{rad},2} N_2(0) e^{-\Gamma_2 t}, \tag{4.2}$$

where $I(t)$ is the phonon detection rate. In principle, it is still possible to fit the data to this equation and obtain the two rates Γ_1 and Γ_2, but it can be difficult to discriminate between two or more decay pathways and care must be taken when interpreting the data. Often the average lifetime, defined as the time when 1/e of the electrons have decayed, will provide a better metric to use as a comparison between samples when multiple radiative decay pathways are present in the sample. For additional information about the technique the reader is referred to reference [72].

4.5 Quantum efficiency measurements

Quantum efficiency (QE) measurements can be performed in order to determine the ratio of radiative emission in a sample, compared to non-radiative processes. If for instance half of the absorbed photons result in an emitted photon, the quantum yield of the phosphor is considered to be 50%. The measurement is carried out in two steps by using an integrating sphere, which in theory allows for detection of every photon that exits the sample. First, the emission of the light source in an empty sphere is measured. This is followed by a second measurement where the luminescent sample is placed in the sphere and both light from the light source as well as the luminescence from the sample are measured simultaneously. By using a calibrated setup, it is possible to determine the total amount of photons absorbed and emitted by the sample and consequently determine the quantum efficiency.

4.6 Ellipsometry

A light beam can be described by an oscillating electric field that propagates in a certain direction with an amplitude, frequency and phase. If light is filtered or created so that the geometry of the oscillations of the electric field becomes specified, the light is said to be polarized. The polarization is given by the electric field vector and the phase. If the x- and y-components of the electric field are in phase, the light has a linear polarization, and if they are 180 °C shifted, the light has circular polarization. If they are somewhere in between these two cases, the light is elliptically polarized. In ellipsometry, linearly polarized light is reflected of a surface or interface, which changes the polarization state of the light. The incident light consists of two components, *s* and *p*, where the *s*-component is oscillating perpendicular to the plane of incidence and parallel to the sample surface, and the *p* component is oscillating parallel to the plane of incidence. The amplitudes of the *s* and *p* components after reflection are denoted by R_s and R_p. The ellipsometer measures the amplitude ratio on reflection, ψ, and the phase shift, Δ:

$$\frac{R_s}{R_p} = \tan\psi\, e^{i\Delta}. \tag{4.3}$$

ψ and Δ contain indirect information about the optical constants of the sample as well as the thickness of the film. By using the Fresnel equations, it is possible to fit ψ and Δ to a model and extract this information. In this thesis, ellipsometry has primarily been used to determine the thickness of the deposited thin films. This is done by fitting the data to a Cauchy function:

$$n(\lambda) = n_0 + \frac{n_1}{\lambda^2} + \frac{n_2}{\lambda^4}, \tag{4.4}$$

where $n(\lambda)$ is the refractive index as function of wavelength, and n_0, n_1 and n_2 are the fit parameters. The thickness can usually be determined easily if $n(\lambda)$ is known, and sometimes also the absorption, though usually a strong absorption requires further parameterizing using other functions. For additional information about the technique the reader is referred to reference [73].

4.7 X-ray Diffraction

X-ray diffraction (XRD) is a technique that utilizes X-rays scattered from the electrons in a material to obtain structural information about the sample. If the atoms in the sample are arranged in a periodic fashion, as in crystals, the diffracted waves will consist of sharp interference maxima that depend on the symmetry and distribution of atoms. The resulting diffraction pattern thus makes it possible to deduce the atomic distances in the material, typically achieved by comparing the signal with previously obtained patterns found in various databases. Amorphous materials on the other hand, have little or no apparent periodicity and will scatter X-rays randomly with no evident peaks in the resulting intensity distribution. The possible geometries and the information that can be obtained with XRD are tremendous. For additional information about the technique the reader is referred to the book: X-ray Crystallography by Waseda *et.al.* [74].

4.8 X-ray Fluorescence

X-ray fluorescence (XRF) utilizes high energy X-rays to knock out core electrons from atoms in the sample. This allows an electron from a higher energy state to relax to this now unoccupied level and in the process produce fluorescence in the form of an X-ray that can be detected. The wavelength of the emission is usually characteristic of the element, though some elements have overlapping emission, which can be accounted for. By comparing the detected intensity to standards with known quantities of the respective element, it is possible to determine the relative amount of the various elements in the sample. In theory all elements with $Z \geq 4$ can be detected, but due to instrumental limitations and low X-ray fluorescence yields for the light elements, it is challenging to quantify elements with $Z < 11$. The incident X-rays do not interact with the bonding electrons and the technique consequently does not provide structural information. For additional information about the technique the reader is referred to reference [75].

4.9 X-ray Reflectometry

X-ray reflectometry (XRR) can be used to analyse the roughness of a surface or interface, or the density and thickness of individual layers of a thin film consisting of one or more layers. It is similar to ellipsometry and provides complimentary information. The basic principle is to reflect incident X-rays off a flat surface or interface and measure the intensity in the specular direction. A perfectly smooth and flat surface will follow the law of Fresnel reflectivity, while any imperfections will cause a deviation that can be analysed in order to obtain the density profile of the interface normal to the surface. In a material with an average electron density profile, $\rho_e(z)$, the X-ray reflectivity can be approximated by [76]:

$$\frac{R(Q)}{R_F(Q)} = \left| \frac{1}{\rho_\infty} \int_{-\infty}^{\infty} e^{iQz} \left(\frac{d\rho_e}{dz} \right) dz \right|^2, \tag{4.5}$$

where $R(Q)$, is the reflectivity, $R_F(Q)$ the reflectivity of a perfectly smooth surface, $Q = 4\pi\sin(\theta)/\lambda$, λ is the X-ray wavelength, θ is the angle of incidence and ρ_∞ is the density deep into the material. The formula can be used to compare parameterized models of the average density in the z-direction, and the parameters can then be fitted until they match the measurement. A thin film sample will typically have two interfaces, one at the surface of the film and one between the film and the substrate. The reflected signal from these two interfaces will interfere constructively or destructively with each other, resulting in an oscillating signal. The periodicity of the oscillations can be used to determine the thickness of the film. If more interfaces are present, like in a layered thin film, these will cause oscillations with a different periodicity, making it possible to determine the thickness and electron density of each individual layer. For additional information about the technique the reader is referred to reference [77].

4.10 Scanning Electron Microscopy

The scanning electron microscope (SEM) utilizes electrons in order to scan a surface to obtain information about the phase, topography and morphology of the sample. Electrons from a filament are accelerated towards the sample through a lens system which focuses the beam to a spot of a chosen size. The spot has the shape of a droplet and penetrates a few nanometers down in the sample and is what governs the resolution of the obtained images. When the electron beam hits the sample it will generate X-rays as well as elastically and inelastically scattered electrons, and these can be detected by various detectors, resulting in images with different kinds of contrast. The X-rays can be used to obtain location specific

chemical information and can thus be used to generate elemental maps. For additional information about the technique, the reader is referred to reference [78].

4.11 Atomic Force Microscopy

Atomic force microscopy (AFM) is a characterization technique used to scan the surface of a material in order to obtain an image of the topography of the sample surface, and can provide information like surface roughness and grain size. The technique utilizes a sharp tip to raster the surface. The tip is mounted on a flexible cantilever so that when the tip experiences a force from the surface, the cantilever will bend. In order to observe this, a laser is pointed at the top of the cantilever and the reflection of the laser is monitored on a photodiode detector. When forces act on the tip, the reflected laser beam will shift and this shift is used to give a 3D-image of the surface by plotting the laser deflection against the tip position. For more information on the technique the reader is referred the book: Atomic Force Microscopy by Greg Haugstad [79].

Chapter 5 – Results and discussion

In this section, the most important results will be presented and discussed with regard to the goals for the respective study, but also in light of the broader goal to increase understanding of luminescent materials made by ALD and enhancing the efficiency of solar cells.

5.1 Deposition of europium titanium phosphate thin films

Based on paper I

The goal of the study on europium titanium phosphates was originally to understand the implications of adding phosphate to the luminescence, and if this could have implications transferrable to other systems. Our initial studies of the luminescent properties of amorphous europium titanate thin films proved increased emission intensities when a Me_3PO_4 + H_2O + O_3 cycle was added between the $Eu(thd)_3/O_3$ and $TiCl_4/H_2O$ cycles. We thus wanted to use EXAFS to elucidate the structural differences and accurately determine the Ti-Eu distances and the coordination sphere around Eu^{3+} in both these systems. This proved to be challenging for a number of reasons, and I will share some of our experiences with this so that some of the pitfalls we encountered may be avoided in the future.

In EXAFS analysis, the results are fitted to a model to obtain structural information about the average interatomic distances and the average coordination of each atom. However, the results rely on that a suitable valid model can be constructed. As with all kinds of fitting, the number of parameters is crucial. It is possible to fit anything given enough parameters to adjust, and in a system containing europium, titanium, phosphorous and oxygen in an amorphous matrix, there are simply too many parameters to provide trustworthy data, unless you start the fitting procedure with the correct values. Prior knowledge of the sample is essential in order to fix enough interatomic distances to allow for valuable fitting. There are, however, no reports of any stable Eu-Ti-P-O phases in the literature to provide a good starting point. Instead, samples of various crystalline Eu-Ti-O phases were synthesized, intended to be used as references. This could work if the Eu-O and Eu-Ti distances and coordination would be similar to the amorphous samples.

Using known distances from the respective crystal structures to fit the measurements of the reference samples also proved to be challenging as the data quality was simply too poor, possibly due to a combination of inhomogeneity of the sample, instability of the synchrotron beam and low quality crystals. Fitting of the Eu_2O_3 powder revealed that the parameter depending on the instrument changed between each scan and was outside common values for this compound. Another problem encountered was that even though every sample was measured for several hours, the statistics were still too poor, as the signal obtained from every scan could vary significantly and some of the data had to be discarded due to this. It was later determined that this could have been related to the samples not being photostable and possibly undergo structural changes while being exposed to UV or X-rays. While these changes would be interesting to study, it is extremely challenging to obtain enough prior knowledge about the interatomic distances that some of these can be fixed in order to fit the unknown parameters. With the limited EXAFS experience in our group, this system proved to be too complex to start building competence with and future endeavours should start with simpler systems.

The samples still showed a number of interesting luminescent properties that were worth investigating. Of particular note was a reduction in luminescence intensity when being exposed to the UV-laser used for the PL measurements, as shown in **Figure 5.1.** The effect is called photobleaching, and is commonly associated with reversible or irreversible photostructural changes in highly amorphous materials [80-83]. In those cases, a change in refractive index or a shift in the absorption edge can usually be observed, resulting in a reduction in absorption. The samples in this study did not exhibit any such features and it was consequently not possible to find a model that describes the effect for this system. Some

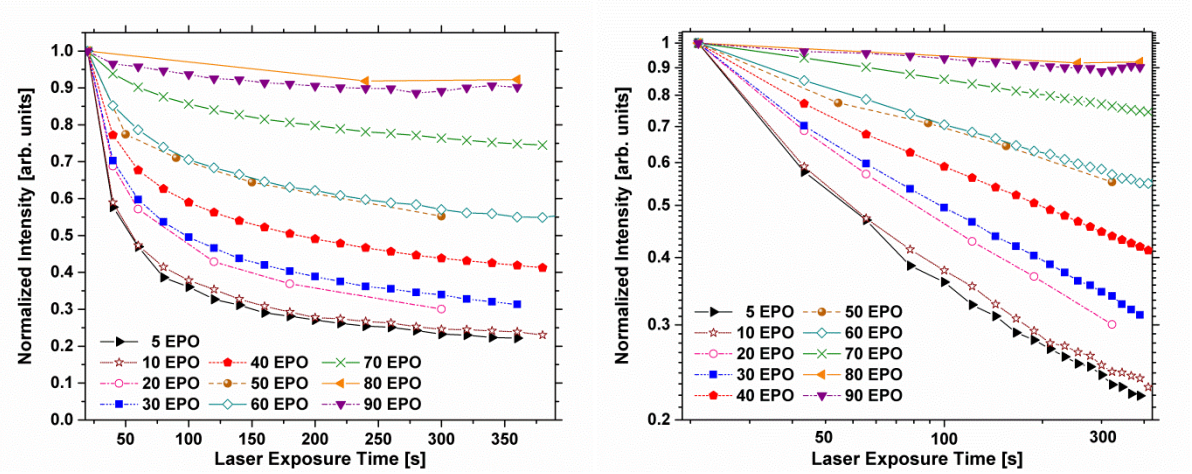

Figure 5.1: Normalized PL intensity vs. laser exposure time for as deposited samples. Each data point represents the total PL intensity per second divided by the maximum intensity measured for that data set. Left image shows data on linear scales, while right image shows the same data on logarithmic scales.

general observations could still be made. The emission rate falls of exponentially, and by plotting the total intensity as a function of laser exposure time on logarithmic scales, and fitting the data to a linear function, it was possible to extract a value for the bleaching rate. Increasing the titanium concentration increased the bleaching rate, which means the effect can be controlled, and also suggests that titanium is involved in the process. The bleaching was not observed in samples without phosphate, so it follows that phosphate is either also directly involved in the process or indirectly by increasing the disorder. The latter seems most likely as XRF results revealed that the phosphate content was slightly reduced in samples with high titanium concentrations and photobleaching is an effect that usually only is observed in highly amorphous materials [82-85]. There is also the fact that adding phosphate increased the emission intensity by up to 400% compared to titanium oxides depending on composition. This can be explained by phosphate disordering the structure, and thus distort the f-orbitals of Eu^{3+} enough to further relax the Laporte rule, increasing the spontaneous emission rate.

It was also determined that the effects of the bleaching process can be reversed by tempering the bleached samples at the deposition temperature for a sufficiently long period, while annealing the samples above the deposition temperature increases the photostability. Particularly annealing at 500 °C or above for 10 minutes had a significant effect. At the same time, the lifetime of the Eu^{3+} emission also increased for annealing temperatures up to 700 °C, which could be an indication that the bleaching is associated with quenching sites that can be removed by annealing, or it could be that the quenching sites are created during the bleaching process, and that annealing makes the material resistant to this. While the bleaching effect was severely reduced at 700 °C for all samples, it did not disappear before the samples were annealed at 800 °C, at which point the luminescence was sharply reduced, which disqualified the material as a candidate for a conversion layer for solar cells.

An overview of the emission intensity of each sample (~100 nm) is presented in **Figure 5.2.** Note that the figure does not account for the absorption, which severely impacts the emission intensity. Using the extinction coefficient at 325 nm, it was possible to calculate the absorption and the relative emission intensities of each sample, revealing that 70 pulse% EPO will result in the highest emission intensity, provided a sufficient film thickness or a low enough excitation wavelength, and should consequently display the highest quantum efficiency. This was also in agreement with the photoluminescence decay measurements presented in **Figure 5.3**, revealing that the lifetime first drops significantly in samples with 80 pulse% EPO or more due to concentration quenching.

The luminescence quenching observed at 800 °C coincided with a change in local coordination around Eu^{3+} and a reduction in the lifetime, which AFM and SEM indicated was due to large structural changes probably resulting in segregation of europium and titanium.

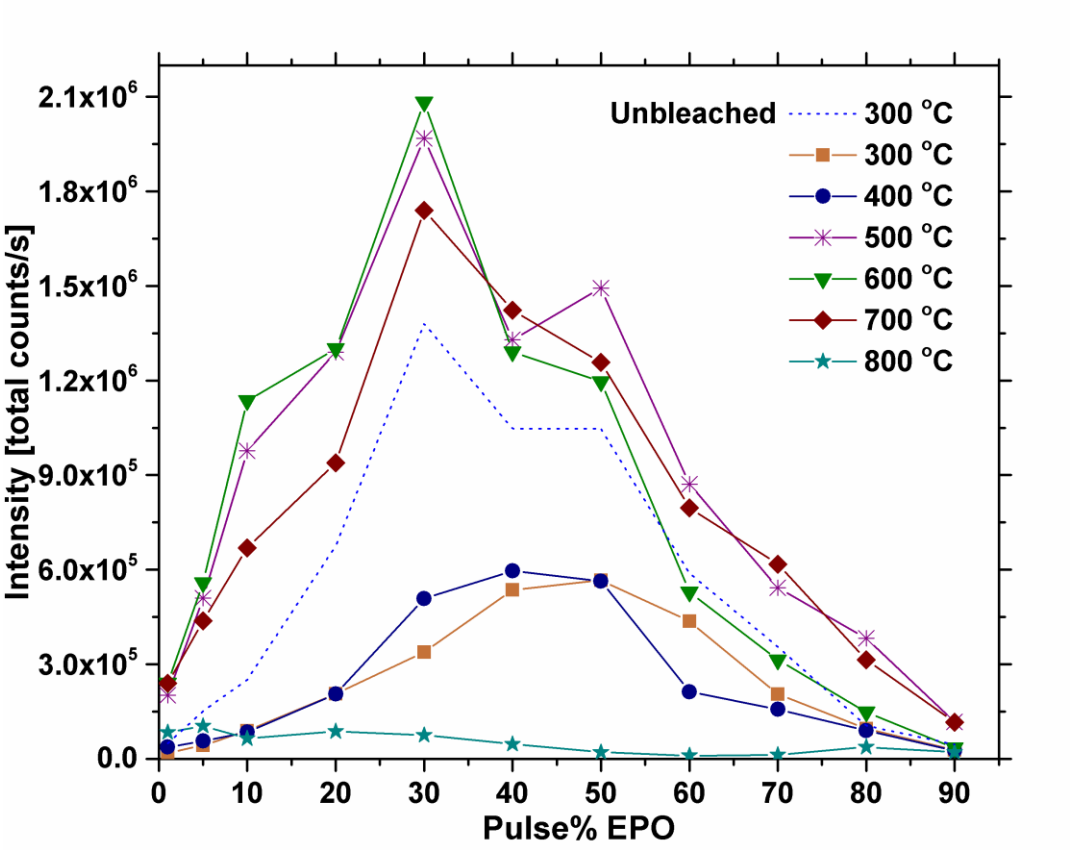

Figure 5.2: Total PL intensity vs. pulse% EPO for samples annealed at different temperatures (300 °C is as deposited) at 325 nm excitation. Note that the samples are compared after 20 seconds of laser exposure in order to reduce uncertainty introduced by photobleaching. The dotted line shows the estimated emission intensity after 1 s of laser exposure, obtained by fitting the data to the right in **Figure 5.1** to a linear function and extrapolating to 1 s.

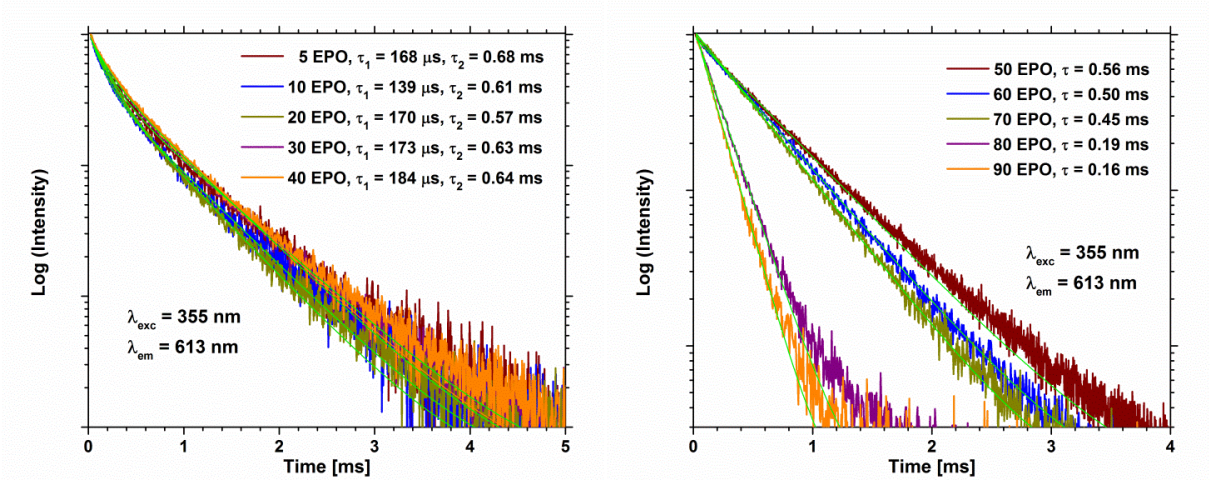

Figure 5.3: Photoluminescence decay measurements of as-deposited samples. 5-40 EPO (left) are fitted using a biexponential decay function, while 50-90 EPO (right) are fitted by a single exponential decay function.

The average Eu-Eu distance is thus expected to decrease, increasing concentration quenching, while the average Ti-Eu distance should increase, reducing the energy transfer between them. This was also supported by the presence of a broad emission in the 725-950 nm region for the sample with 1 pulse% EPO. This was interpreted as belonging to titanium complexes that no longer can transfer all their energy to Eu^{3+} due to the increased distance. Annealing beyond 800 °C increased the NIR emission for this sample, and after annealing at 1000 °C, most of the other samples also started to exhibit this emission, as shown for a sample containing 80 pulse% EPO in **Figure 5.4**. Note that some Eu^{3+} emission is still present, however, the shape of the emission is reminiscent of $EuPO_4$ [86], with the $^5D_0 \rightarrow {}^7F_2$ transition not being the most intense anymore, indicating that energy transfer no longer takes place and that the observed Eu^{3+} is due to direct excitation of Eu^{3+} instead of by energy transfer from the titanium complex.

The quantum efficiency of a sample with 60 pulse% EPO and annealed at 600 °C was determined to be ~6%. The NIR emission of the titanium phase could explain the poor efficiency, as emission in the 725-950 nm region suggests that the Stokes shift is very large and phonon emission could be the dominant decay process.

While the photobleaching properties potentially could be useful for applications like optical storage and holography [87], it seems unlikely that the material would be able to enhance the efficiency of solar cells, even if additional optimization should be possible. The study on EuTiPO was nevertheless useful for improving our understanding on what kind of properties to look for when selecting a host material for lanthanides. While a strong charge transfer absorption is desired, efficient energy transfer is easier to achieve with a large Förster radius. As this radius depends on the quantum yield of the donor in the absence of an acceptor, it implies that the host should display significant luminescence without any lanthanide doping. This could not be said for the amorphous Ti-P-O host in this study. So

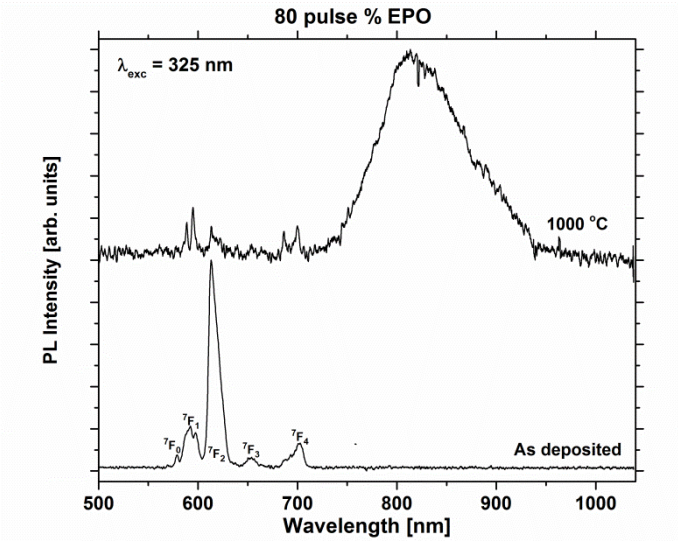

Figure 5.4: PL emission of an 80 pulse% EPO sample as-deposited and after annealing at 1000 °C.

while the EuTiPO system demonstrated that it is possible to achieve reasonable luminescence even for amorphous systems with ALD, in order to realize quantum efficiencies that can be useful for solar cells, it is most likely necessary to use a crystalline host material. At this point the most interesting candidates were $YBiO_3$, Y_2MoO_6, YVO_4 and Y_2WO_6, due to displaying a strong M-O charge transfer absorption and having a metal site that easily can be substituted for a lanthanide like Yb^{3+}. A high oxidation state like in V^{5+}, W^{6+} or Mo^{6+} usually implies that these metal ions are easily reduced and will consequently have a strong absorption. Bi^{3+} on the other hand, is known to be a good sensitizer for lanthanides [88-91], though, it could possibly be oxidized by lanthanides that are easily reduced, like Eu^{3+} and Yb^{3+}, which could lead to unwanted charge transfer states. YVO_4 is the most studied host material for lanthanides among the other candidates and is commonly used in lasers with high efficiency [92]. Our group also had recent experience with ALD deposition of V_2O_5 [93] and in addition there were two reports of downconversion using this material [27, 28]. YVO_4 was consequently chosen as the next host material to deposit and investigate.

5.2 Deposition of ytterbium vanadate

Based on paper II

The goal of this study was to achieve controlled growth of the $YbVO_4$ system and characterize its optical properties. $YbVO_4$ can be considered an $Y_{1-x}Yb_xVO_4$ system in which 100% of the yttrium positions are occupied by Yb^{3+}. YVO_4:Yb^{3+} has previously been suggested as a down-conversion material for solar cells [27, 28], and deposition of $YbVO_4$ can thus be considered a step in the direction of depositing the more complex YVO_4:Yb^{3+} system. The challenges associated with the deposition of multicomponent films were already discussed in chapter 3.2, and in general it is usually a good idea to start with the binary systems and gradually add complexity in order to understand the effect each component has on the resulting films. Precursors were primarily selected based on the temperature region where the binary oxides display self-limiting growth. While a multicomponent process may display self-limiting growth over a different temperature range than the individual binary processes, the chance of a successful deposition if all the binary processes display self-limiting growth at the selected deposition temperature is high. In this case, the elements could be deposited by $VO(thd)_2$/$Yb(thd)_3$/$Y(thd)_3$ and O_3 processes, as they shared a self-limiting growth region between 240-300 °C, although the deposition rate of V_2O_5 increases quite significantly with temperature, even within this range [93]. For the mixed Yb_2O_3/V_2O_5 system, a deposition temperature of 240 °C was used and self-limiting growth was achieved. Elemental analysis

using XRF showed that the composition of the films could be controlled, as shown in **Figure 5**.5.

The films were amorphous as deposited and exhibited no detectable luminescence, but crystalline $YbVO_4$ could be obtained by post deposition annealing at various temperatures depending on composition, at which point luminescence could also be detected. Particularly interesting was that samples with an excess of V_2O_5 could be crystallized at significantly lower temperatures than those with stoichiometric amounts of V_2O_5 and Y_2O_3, or excess of Yb_2O_3. This was determined to be related to the relatively low melting point of V_2O_5 of only 690 °C. Near and above the melting point, excess V_2O_5 acts as a flux, allowing for high mobility of the elements present in the sample, enabling rapid crystallization. The crystallinity and luminescence intensity was also determined to be directly correlated for this system. Evidence supporting this is presented in **Figure 5.6**. The figure shows a comparison of the XRD-intensity for the various samples annealed at 1000 °C, while **Figure 5.7** shows the integrated NIR emission for all the samples annealed between 600-1000 °C. By comparing the two figures, it appears that the intensity of the (400)-reflection is directly proportional to the detected NIR emission signal. This was even further exasperated after differences in absorption were accounted for (i.e. the 50% pulse% $Yb(thd)_3$ sample had the highest absorption, while the 25% had the lowest). The (200)-reflection could also be used to show this, but this reflection dwarfs the other reflections. **Figure 5.8** shows the XRD intensity of a sample with a 1:3 pulse ratio of $Yb(thd)_3$ and $VO(thd)_2$ annealed at different temperatures. These results also show a correlation between the intensity of the (200) and (400)-reflections and the detected PL-intensity in **Figure 5.7**.

As $YVO_4:Yb^{3+}$ is known to be highly sensitive to concentration quenching, and as there is no mention of luminescent $YbVO_4$ in the literature, it was surprising to detect significant

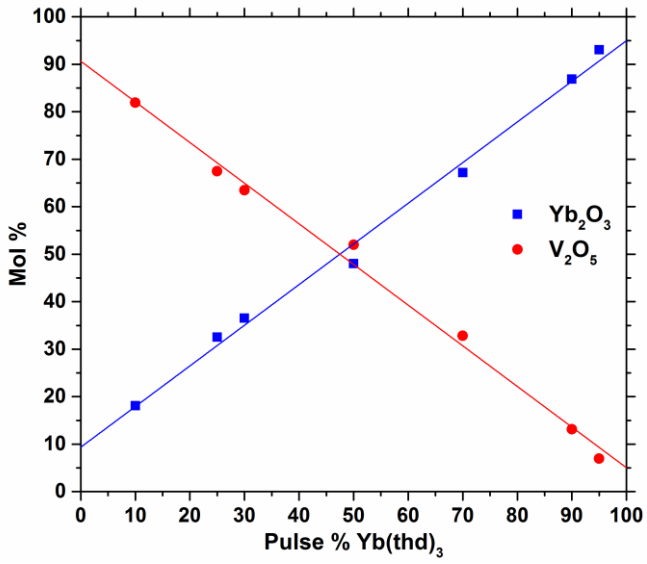

Figure 5.5: Mol% vs. pulse% $Yb(thd)_3$ as determined by XRF, fitted to linear functions.

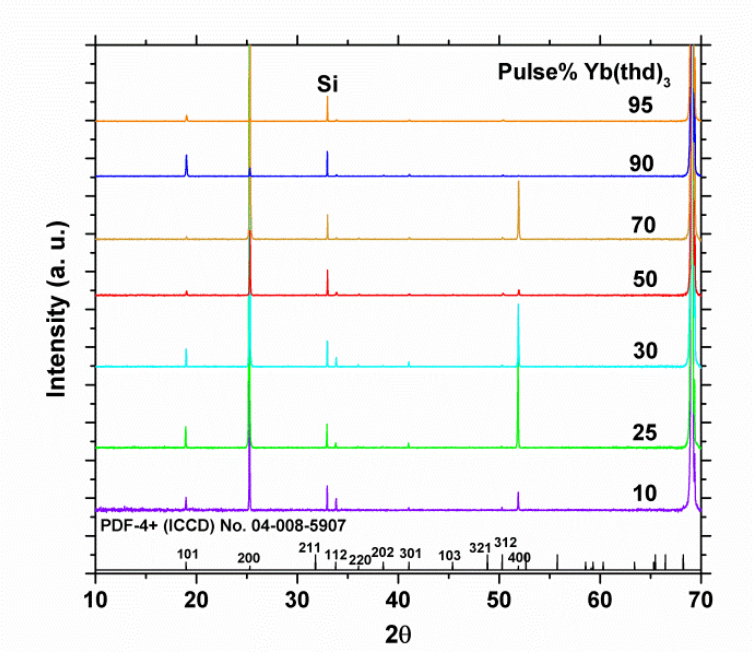

Figure 5.6: X-ray diffraction patterns of all the samples annealed at 1000 °C for 1 hour.

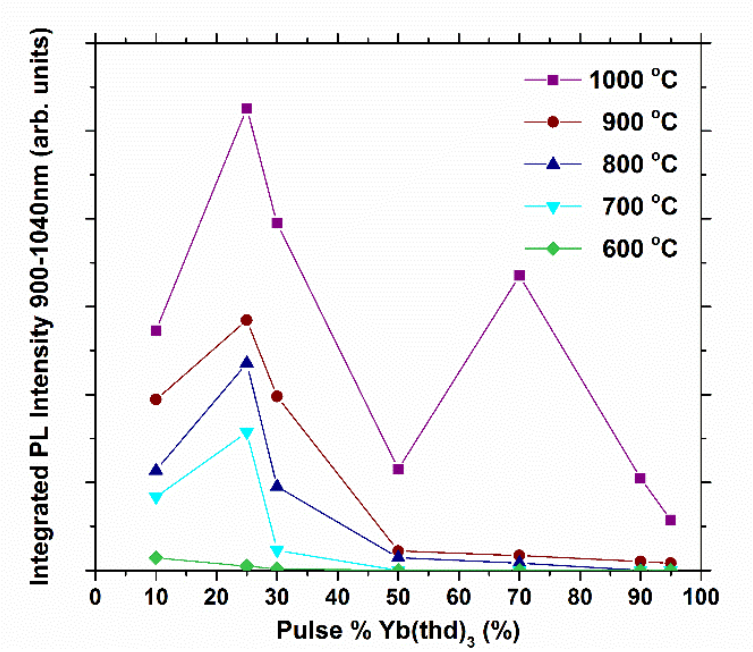

Figure 5.7: Total detected NIR intensity of all the samples annealed at 600-700 °C.

NIR emission from the samples on an OceanOptics USB4000 detector, whose sensitivity in the NIR is extremely poor. The excitation and emission spectra of a sample with 25 pulse% $Yb(thd)_3$ using a dedicated NIR-detector for the NIR emission is presented to the left in **Figure 5.9**, while the expected origin for the luminescence is shown to the right. Even with the maximum amount of Yb^{3+} in the sample, the Yb^{3+} emission is not completely quenched,

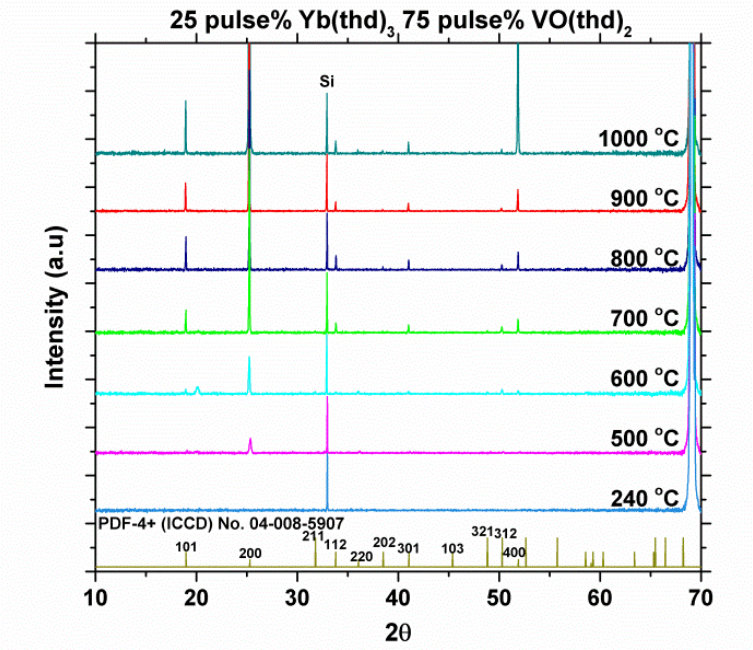

Figure 5.8: X-ray diffraction patterns of samples with a 1:3 pulse ratio of $Yb(thd)_3$ and $VO(thd)_2$ annealed at different temperatures.

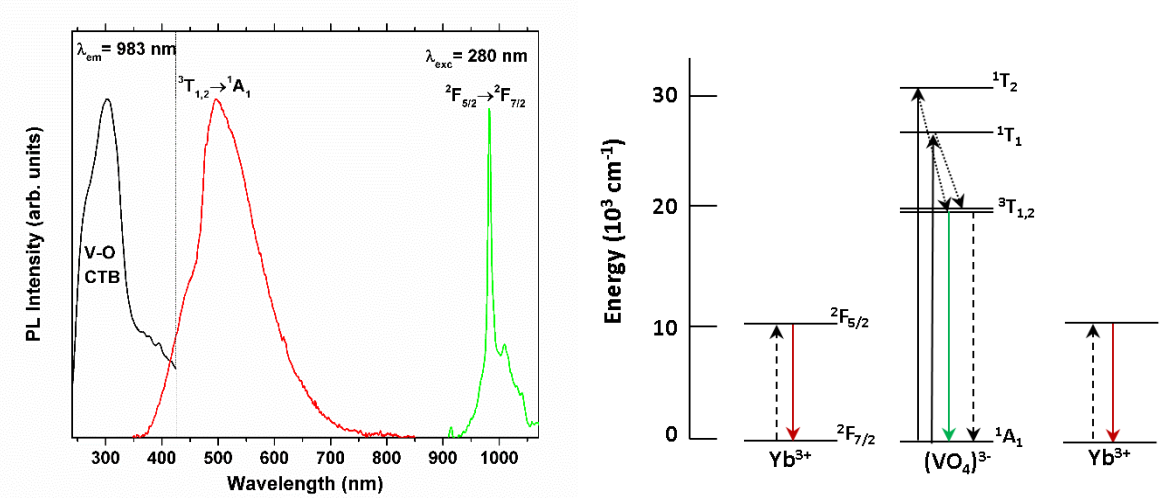

Figure 5.9: Left: Normalized PLE spectrum (black) monitoring the 983 nm emission of Yb^{3+} and normalized PL spectra (green/red) of a sample with a 1:3 pulse ratio of $Yb(thd)_3$ and $VO(thd)_2$. Right: Schematic energy level diagram of $(VO_4)^{3-}$ and Yb^{3+} in $YbVO_4$ [27, 94]. Black arrows show excitation, while the green and red arrows show emission processes. Relaxation from the $^1T_{1,2}$ excited states to the $^3T_{1,2}$ excited states is most likely non-radiative (short dash). From the $^3T_{1,2}$ excited states, energy can transfer to two nearby Yb^{3+} via CET (dashed arrows). The positions of the energy levels are approximate.

implying that the concentration quenching efficiency never reaches unity in this system. Obtaining definite proof of whether the energy transfer from $(VO_4)^{3-}$ to Yb^{3+} takes place via CET or via some other currently unknown mechanism is challenging. Nevertheless, from our

current understanding, CET is the only possible mechanism as Förster energy transfer requires an overlap between the emission integral of the donor and absorption integral of the acceptor. In this system, this can only be achieved through a second order process, i.e. $(VO_4)^{3-}$ transfers energy to two nearby Yb^{3+}. This process only competes with spontaneous emission and non-radiative relaxation. The spontaneous emission is spin-forbidden and consequently has low probability, while non-radiative relaxation depends on numerous factors, but can possibly be quite low in a highly crystalline material. The second order process should in this case be quite probable according to Veerger *et. al.* [42]. In addition, the energy levels in $YbVO_4$ are positioned similarly to the energy levels in the Tb^{3+}/Yb^{3+} system, where energy transfer via CET has been proven to take place by fitting experimental lifetime data to Monte-Carlo simulations [42]. It is thus probable that energy is transferred similarly in these two systems. Wei *et. al.* suggested that some energy may be transferred via the O^{2-}–Yb^{3+} charge transfer state, however, as this state locates at around 210 nm in YPO_4:Yb^{3+} [95], which has a similar crystal structure to $YbVO_4$, it is evident that excitation at 250-350 nm is insufficient to reach this state. The excitation spectrum thus clearly implies that energy transfer does not take place via this state.

The differences in the peak intensities of the $^1T_1$ and $^1T_2$ seen in the excitation spectrum of YVO_4 has previously been explained by Ronde and Blasse [94]. They state that since the charge transfer absorption of the $^1T_2$ state is incredibly strong, most of the absorption via this state is absorbed near the surface where the defect concentrations are higher which causes radiative emission to be easily quenched. The charge transfer absorption of the $^1T_1$ state is significantly lower, and absorption takes primarily place in the bulk, where defect concentrations are low, and thus dominates the excitation spectra. The difference in the peak intensities does consequently not imply a difference in the energy transfer to Yb^{3+}. While ruling out all other possibilities does not directly prove that energy transfer takes place via CET in this system, it does certainly seem likely to be the case at this point.

With respect to using the material for solar cells, the material is thus clearly a candidate if energy transfer via CET can become efficient, e.g. by reducing the amounts of quenching sites to a minimum. Concentration quenching is of course expected to be tremendous in pure $YbVO_4$, though this is easily solved by diluting with yttrium. However, a challenge with $YbVO_4$ made by ALD is the absorption. **Figure 5.10** shows two FE-SEM images of samples with 25 and 50 pulse% $Yb(thd)_3$. The sample with 25 pulse% $Yb(thd)_3$ has significantly higher crystal quality compared to the 50 pulse% sample according to XRD, and also appears to have more regularly shaped grains. As the samples crystallize, they turn from being a film into micron-sized grains. As more crystalline samples equals higher conversion efficiency, but also seems to cause higher transparency, it is important to find a way to

crystallize the material in such a way that the materials still covers the whole surface if it is to be used for solar cells. This was investigated in more detail in paper III.

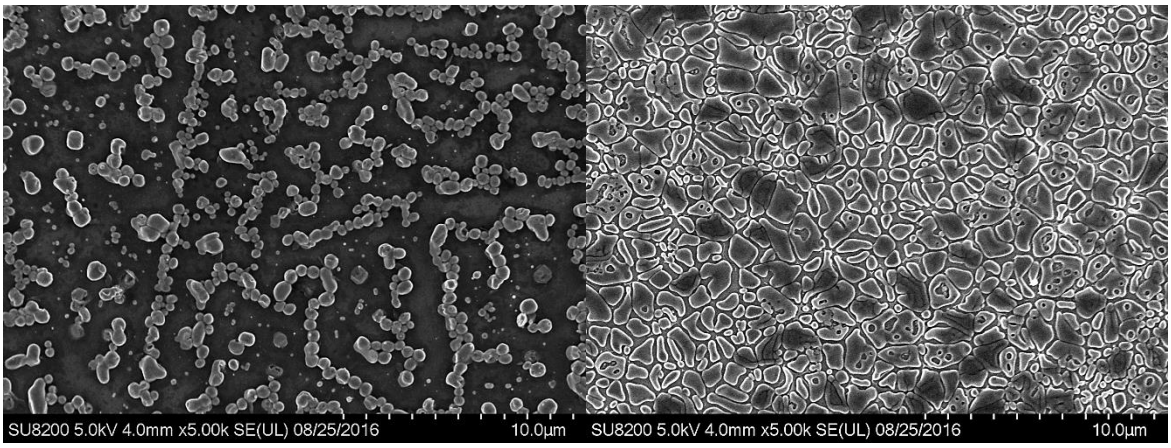

Figure 5.10: FE-SEM image of samples with 1:3 pulse ratio (left) and 1:1 pulse ratio (right) of $Yb(thd)_3$ and $VO(thd)_2$.

5.3 Deposition of YVO_4: Yb^{3+}

Based on paper III

The objective of this study was to achieve controlled growth of YVO_4: x% Yb^{3+} by ALD, characterize most of the optical and structural properties, and determine the luminescence quantum efficiency of the produced films in order to have a benchmark that can be used to track further progress.

YVO_4: Yb^{3+} is similar to $YbVO_4$ except that the Y^{3+}/Yb^{3+} ratio can be tuned in order to reduce concentration quenching, and the annealed films could thus have reasonable quantum efficiencies, provided the energy transfer from $(VO_4)^{3-}$ to Yb^{3+} is good. Wei *et. al.* found that the theoretical upper-limit efficiency is 148%, 150%, 165%, 179%, and 186% in powder samples with 1%, 2%, 4%, 8% and 16% Yb^{3+}, respectively [27]. When determining these upper-limit quantum efficiencies, energy transfer from $(VO_4)^{3-}$ to Yb^{3+} is assumed to take place via CET and any concentration quenching of Yb^{3+} emission is ignored. In addition, the quantum efficiency of both $(VO_4)^{3-}$ and Yb^{3+} is assumed to be 100%. Lanthanides can often achieve near 100% quantum efficiency at low concentrations, though the efficiency of $(VO_4)^{3-}$ can probably never reach 100%. However, if the energy transfer from $(VO_4)^{3-}$ is efficient, it might be possible to eventually reach quantum efficiencies close to the theoretical upper-limit, at least in the case of 1-8% Yb^{3+}. That said, energy transfer via CET in this system has not been proven beyond a doubt and measuring the actual quantum efficiency of a material that is excited in the UV and emits in the NIR is challenging, and is consequently

rarely reported in the literature. The only report is from Xu *et. al.* who determined the quantum efficiency of YVO_4: 5 mol% Bi^{3+}, x mol% Yb^{3+}, obtaining a quantum efficiency of 12.3% for 10 mol% Yb^{3+}. While this number may appear somewhat depressing, it is a reasonable start, as optimizing quantum efficiencies is extremely challenging. YVO_4: 5 mol% Eu^{3+} can have quantum efficiencies up towards 70% [96], yet most reports in the literature are far below this, e.g. Singh *et. al.* measured only 9% for the same Eu^{3+} concentration [97]. The synthesis method, source material, the quality of the source material and probably also uncertainties in the measurement method, all contribute significantly, implying that quantum efficiencies can change tremendously for what appears to be similar materials. A value of 12.3% is thus far from discouraging and could in fact be an indication that CET can become efficient in YVO_4:Yb^{3+}. If reasonable quantum efficiencies can be achieved, it should not take long before the material can be used for enhancing the efficiency of solar cells. YVO_4:Eu^{3+} has already been established as a material able to reduce UV degradation of TiO_2 organometal halide perovskite based solar cells, while simultaneously increasing light harvesting capabilities [98]. YVO_4:Yb^{3+} has the potential to surpass this material if it does indeed display downconversion and is consequently an exciting material to investigate.

While thin films are not renowned for being ideal when it comes to optimizing quantum efficiency, ALD does offer a unique method of synthesis, and when it comes to high quality thin films, ALD is among the best techniques available. Particularly that the samples can be crystallized at relatively low temperatures could be beneficial with respect to defect formation, and with ALD it is possible to deposit the material in the form of a layered structure.

The first challenge that emerged when working with this system as opposed to pure $YbVO_4$, was that the addition of $Y(thd)_3/O_3$ resulted in freckled films. The films were slightly less conformal than the $YbVO_4$ thin films, while the reproducibility of both the growth rate and the PL emission after annealing was quite poor. Despite this, the annealed samples were indeed YVO_4 according to XRD and exhibited NIR-emission several orders of magnitude more intense than that of the $YbVO_4$ samples, as shown in **Figure 5.11.** This was expected, as the concentration quenching efficiency in $YbVO_4$ should approach 100%. The PL measurements also suggested that the $Y(thd)_3$ precursor used for the deposition contained significant amounts of Eu^{3+} and Dy^{3+} impurities. Note that the sensitivity of the detector used is around 15 - 1500 times higher in the visible region compared to the NIR, so while it may appear that the Eu^{3+} and Dy^{3+} signal is strong, it is in fact far weaker than that of Yb^{3+}. Nevertheless, the impurities were not distributed homogeneously throughout the annealed samples and both the spectrum and intensity varied significantly depending on which part of the sample was being excited, making any kind of comparative or quantitative study impossible. It was also unclear whether the impurities had an effect on the Yb^{3+} emission, i.e.

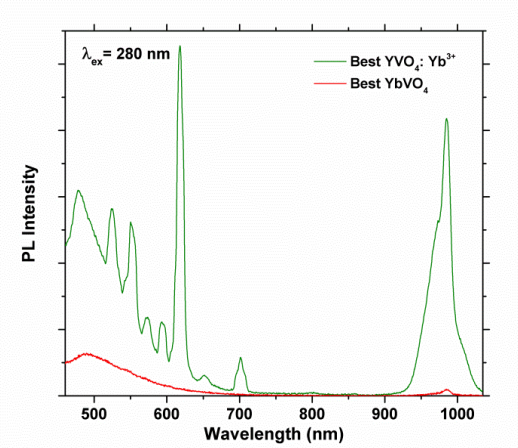

Figure 5.11: PL measurement comparing the emission intensity of the most emissive $YbVO_4$ sample and the most emissive YVO_4:Yb^{3+} sample.

energy transfer from $(VO_4)^{3-}$ to Eu^{3+} or Dy^{3+} is a first order process and will dominate over second order CET. Alternatively, Lau *et.al.* have presented results that indicate that Eu^{3+} potentially could enhance the Yb^{3+} emission through CET from Eu^{3+} to Yb^{3+} [99]. There could also be impurities in the sample that are not observable if they are able to transfer their energy to Yb^{3+}, e.g. Pr^{3+} [100], Nd^{3+} [101], Er^{3+} [102] and Tb^{3+} [103] have all been demonstrated to transfer energy to various degrees to Yb^{3+}.

It was thus crucial to deposit samples without significant amounts of Ln^{3+} impurities. As it was evident that samples without yttrium did not exhibit impurity peaks in the emission spectrum, the solution was to prepare our own $Y(thd)_3$ using the method described in [104]. The resulting films were both conformal and reproducible and no visible freckles were present on the as-deposited samples. The NIR emission was significantly reduced compared to the impure sample with the strongest luminescence while some signal from impurities remained, though the spectra were constant all over the sample surfaces, allowing for a systematic study to be performed. The reason for the reduced NIR emission in samples made by in-house $Y(thd)_3$ is challenging to determine due to the poor reproducibility of samples with $Y(thd)_3$ from Strem. It could possibly be due to Cl^- impurities from the $YCl_3 \cdot 6H_2O$ source material, or due to using a different synthesis route resulting in less pure $Y(thd)_3$, which could lead to more CH_x-impurities in the films. Judging from the differences in the FE-SEM images presented in **Figure 5.12**, it appears that the samples deposited using in-house made $Y(thd)_3$ have a lower crystallinity, and the reduced energy transfer from the $(VO_4)^{3-}$ host to Yb^{3+} is thus expected to be the main reason for the reduced luminescence. The reduction in Eu^{3+} and Dy^{3+} emission should in part be due to using a 4N $YCl_3 \cdot 6H_2O$ source material, as opposed to the 3N $Y(thd)_3$ precursor from Strem, though some of the reduction is also expected to be due to reduced energy transfer from $(VO_4)^{3-}$ to various Ln^{3+} in general.

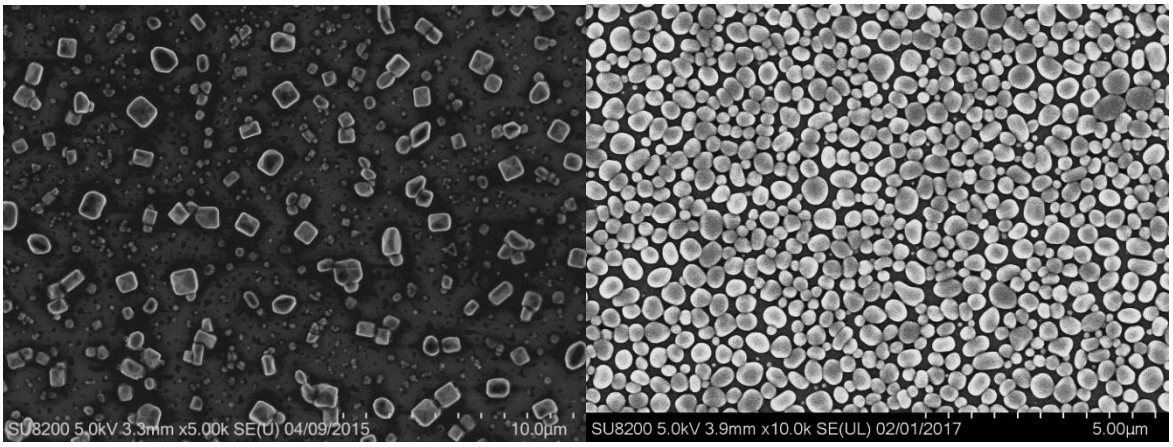

Figure 5.12: FE-SEM images of samples with 4 pulse% $Yb(thd)_3$ deposited with $Y(thd)_3$ precursor from Strem(left) and with $Y(thd)_3$ synthesized in-house (right).

As the $YbVO_4$ system exhibited accelerated crystal growth in excess V_2O_5, resulting in increased luminescence, it was interesting to determine whether this also was the case when yttrium was added. **Figure 5.13** shows XRF data of samples with fixed $Yb(thd)_3$ pulse rate of 4% with varying $Y(thd)_3/VO(thd)_2$ pulse ratios (left), and corresponding NIR emission for each sample after annealing (right). The samples with a slight excess of V_2O_5 all displayed significantly stronger NIR emission, with 56 pulse% $VO(thd)_2$ resulting in the strongest NIR emission. This value was consequently used for a set of samples where the $Y(thd)_3/Yb(thd)_3$ pulse ratio was varied. A set of samples were also deposited at 290 °C in order to determine whether the deposition temperature could influence the optical properties after annealing. As the deposition rate of V_2O_5 is sensitive to the deposition temperature [93] compared to Yb_2O_3 and Y_2O_3, the pulse rate was adjusted in order to obtain similar samples. A 1:1 pulse rate

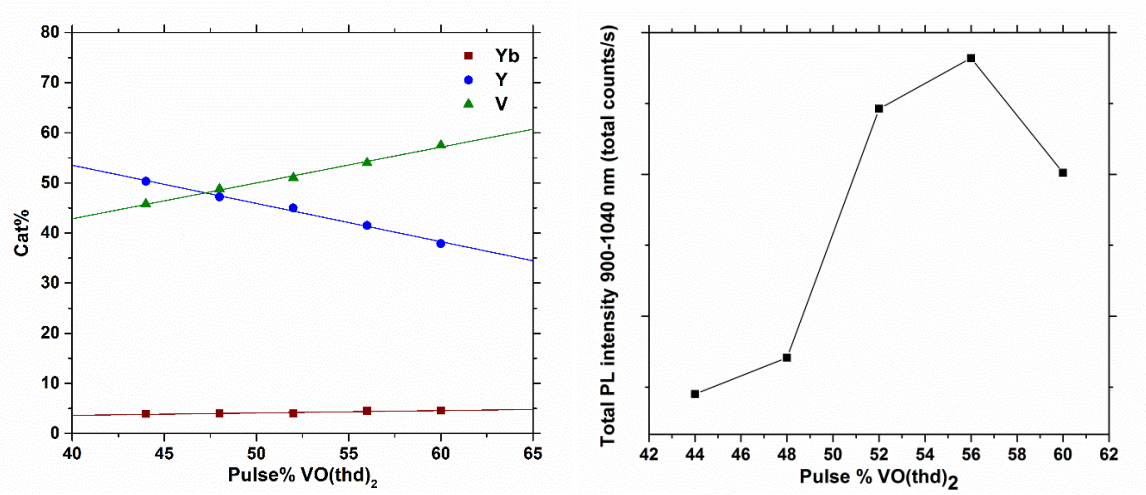

Figure 5.13: Left: Cat% vs. Pulse% $VO(thd)_2$ as determined by XRF analysis of samples with fixed $Yb(thd)_3$ pulse rate, and with varying $Y(thd)_3/VO(thd)_2$ pulse rate. The samples were deposited at 260 °C. Straight lines show result of fitting the data to a linear function. Right: Total NIR emission vs. pulse% $VO(thd)_2$ for the same samples after being annealed at 1000 °C for 1 hour.

between $VO(thd)_2$ and $Yb/Y(thd)_3$ yielded the same Ln_2O_3:V_2O_5 ratio as samples deposited at 260 °C, as shown to the left in **Figure 5.14**, while the figure to the right shows that the PL intensity was more or less unaffected by the change in deposition temperature when the pulse rate was varied to compensate for the increased deposition rate of V_2O_5 at 290 °C. In the following discussion only samples deposited at 260 °C will be considered, but apart from some slight variations the results are also valid for samples deposited at 290 °C.

The excitation and emission spectra of the YVO_4:Yb^{3+} samples after being annealed at 1000 °C for 1 hour is presented to the left in **Figure 5.15**, while the total visible and NIR emission of each sample is shown to the right. The spectra closely resemble those of $YbVO_4$,

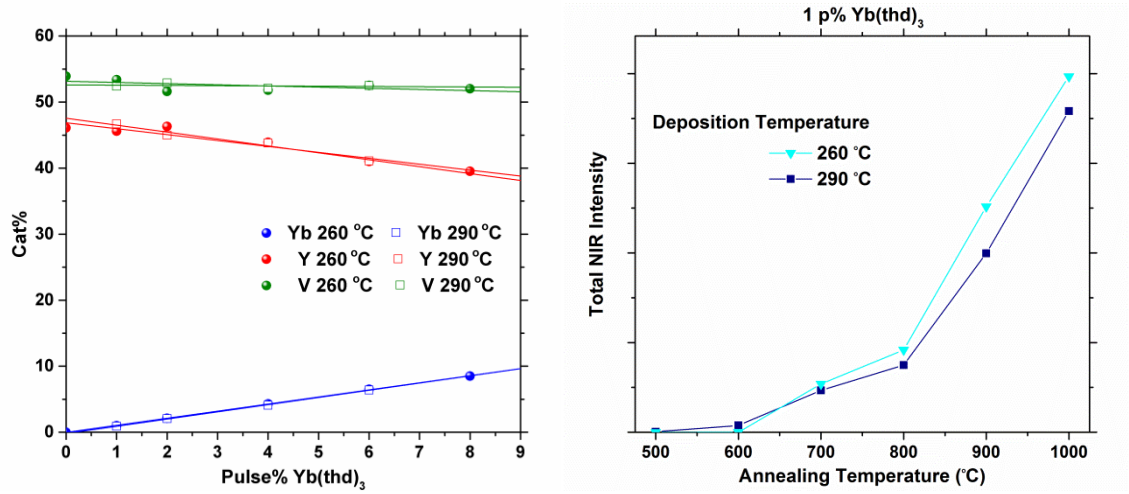

Figure 5.14: Left: Cat% vs. Pulse% $VO(thd)_2$ as determined by XRF analysis of samples with fixed $VO(thd)_2$ pulse rate of 56 % for samples deposited at 260 °C and 50 % for samples deposited at 290 °C, with varying $Yb(thd)_3/Y(thd)_3$ pulse ratios. Right: Total NIR intensity of samples with 1 pulse% $Yb(thd)_3$ deposited at 260 and 290 °C and annealed at various temperatures.

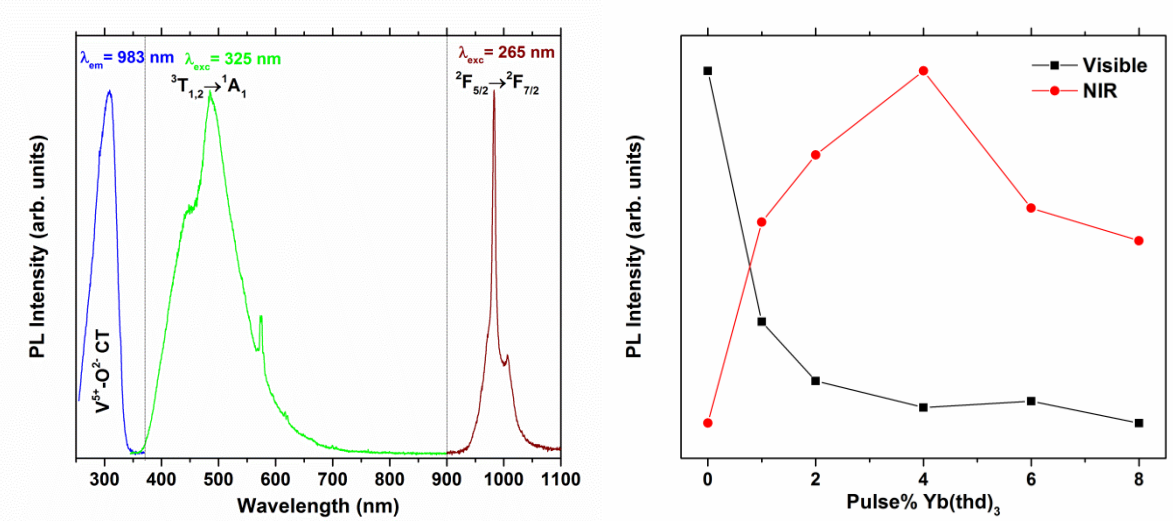

Figure 5.15: Left: Normalized PLE spectrum (blue) monitoring the 983 nm emission of Yb^{3+} and normalized PL spectra (green/red) of an YVO_4: 1 pulse% $Yb(thd)_3$. Right: Total PL counts in NIR and VIS region for samples deposited at 260 °C and annealed at 1000 °C.

with the exception of some signal from Dy^{3+} and Eu^{3+}, and the lack of V_2O_5 absorption in the excitation spectrum. The origin of each peak is consequently assumed to be the same, and the energy level diagram presented previously to the right in **Figure 5.9** is still valid. Energy transfer from $(VO_4)^{3-}$ to Yb^{3+} is demonstrated by a reduction in the visible emission with increased $Yb(thd)_3$ pulse rate, while the NIR emission increases up to 4 pulse% before the negative contribution from concentration quenching causes a reduction in the NIR emission at 6 pulse% $Y(thd)_3$. As 4 pulse% $Y(thd)_3$ corresponds to 4.3 cat% Yb^{3+}, which corresponds to 8.6 mol% Yb^{3+}, this can be considered to be consistent with the results from Xu *et. al.*, who observed the highest quantum efficiency in a sample with 10 mol% Yb^{3+} [105]. However, the previous experimentally obtained value in powders and thin films made by pulsed layer deposition is only 4 mol% Yb^{3+} [27, 28]. Most likely, the experimental value depends on factors like crystallinity, and impurity and defect concentrations, and as such it is likely to vary with synthesis method and choice and grade of source materials. Even so, a value of 8-10 mol% is consistent with calculations performed by Wei *et. al.*, which predicted that 8 mol% should be the ideal Yb^{3+} concentration [27]. Should this be correct, it could be an indication that energy transfer does not take place via first order FRET. In YVO_4:Eu^{3+} the ideal Eu^{3+} concentration in is considered to be 5 mol% [96, 106], and the Förster radius for the Eu^{3+} couple is significantly shorter than for the Yb^{3+} couple, implying that Yb^{3+} should be more affected by concentration quenching. Indeed, from the lifetime measurements presented to the left in **Figure 5.16**, it is evident that concentration quenching does occur already in samples with ~8 mol% Yb^{3+} (4 pulse%), which is also consistent with similar measurements in the literature [27, 28], and the lifetimes are much shorter than previously measured for Eu^{3+} in YVO_4 [97]. As Yb^{3+} and Eu^{3+} interact differently with various defects that cause the concentration quenching, a direct comparison like this might not be possible. Nevertheless, if

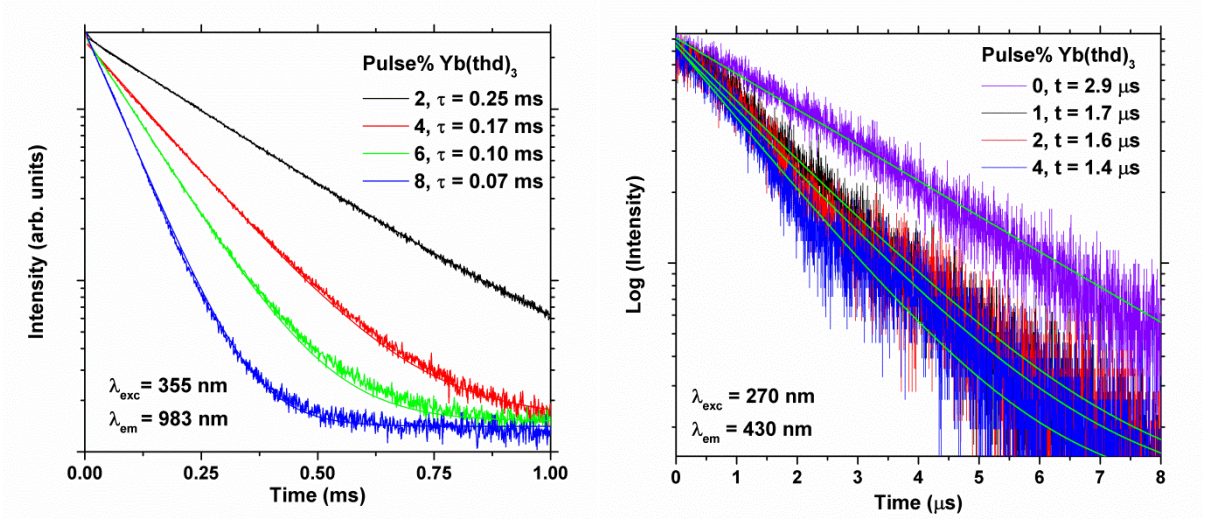

Figure 5.16: PL decay measurements of the Yb^{3+}emission at 983 nm for samples with 2-8 pulse% $Yb(thd)_3$ (left) and of the $(VO_4)^{3-}$emission at 430 nm for samples with 0-4 pulse% $Yb(thd)_3$ (right).

we assume that the difference in the interaction with defects is insignificant, based purely on differences in R_0, the ideal Yb^{3+} concentration should be lower than the ideal Eu^{3+} concentration in the same host material, provided that the energy transfer mechanism from the donor is the same. A difference in the energy transfer mechanism could explain that the ideal relative concentration is increased by 60% when changing the dopant from Eu^{3+} to Yb^{3+}, even when differences in R_0 would imply the opposite. CET process from $(VO_4)^{3-}$ requires two nearby Yb^{3+} in order to occur, while the first order energy transfer in YVO_4:Eu^{3+} only requires one nearby Eu^{3+}. Based on this alone, it would be expected that the ideal Ln^{3+} concentration would be higher for Yb^{3+} than Eu^{3+} provided that energy transfer occurs via a CET process, and could thus be an explanation for the results. This may be an oversimplification, however, the reason why CET is even considered, is, as mentioned during the discussion about $YbVO_4$, that FRET requires an overlap between the emission of the donor and the absorption of the acceptor. As this is not the case for $(VO_4)^{3-}$ and Yb^{3+}, the NIR-emission is best explained by a CET process. An ideal concentration of 8 mol% Yb^{3+} is not at odds with this, but rather supports the notion that energy transfer takes place via CET in this material.

The energy transfer rate from $(VO_4)^{3-}$ to Yb^{3+} can be estimated from changes in the lifetime of the $(VO_4)^{3-}$ excited states when a dopant is added. The lifetime of the visible emission of samples with 0-4 pulse% $Yb(thd)_3$ is shown to the right in **Figure 5.16**. The instability of the laser used in the measurement caused a smearing of the data, so the fitted lifetimes can only be considered to be approximate, though, the relative detected emission between the samples should still provide quantitative data. It is evident that increasing the Yb^{3+} concentration reduces the $(VO_4)^{3-}$ lifetime, in agreement with previous studies [27, 28]. This can be explained by introduction of the extra decay pathway via Yb^{3+}, and can be considered proof that energy transfer from $(VO_4)^{3-}$ to Yb^{3+} occurs. The CET efficiency, η_{CET}, and the theoretical quantum efficiency, η_{QE}, can be determined from the following equations [42]:

$$\eta_{\mathrm{CET,x\ p\%Yb}} = 1 - \frac{\int I_{x\ \mathrm{p\%\ Yb}} dt}{\int I_{0\ \mathrm{p\%\ Yb}}\ dt}, \tag{5.1}$$

$$\eta_{\mathrm{QE}} = \eta_{\mathrm{VO_4}}(1 - \eta_{\mathrm{CET}}) + 2\eta_{\mathrm{Yb}}\eta_{\mathrm{CET}}, \tag{5.2}$$

where I is the decay intensity, x p% Yb indicates the Yb content in the sample, and η_{VO4} and η_{Yb} correspond to the luminescence quantum efficiency of $(VO_4)^{3-}$ and Yb^{3+}, respectively. For the samples with 1, 2 and 4 p% Yb the η_{CET} was determined to be 34%, 44% and 50%, respectively. These values are significantly lower than what has been found for YVO_4:Yb^{3+} powders [27], but slightly higher than what has been reported for thin films made by pulsed measured lifetimes of Eu^{3+} in YVO_4 [97]. As Yb^{3+} and Eu^{3+} interact differently with various laser deposition [28]. By ignoring all quenching processes and setting the luminescence

quantum efficiencies of $(VO_4)^{3-}$ and Yb^{3+} to 1, the upper-limit value of the theoretical quantum efficiency for the samples with 1, 2 and 4 pulse% $Yb(thd)_3$ is 134%, 144% and 150%. Most likely concentration quenching will be impossible to completely avoid in samples with ~8 mol% Yb^{3+}, so the actual upper limit in a perfect YVO_4 host is most likely somewhere between 134% and 150%.

The actual quantum efficiency of the YVO_4: 1 p% Yb phosphor was determined by using the overlapping spectral region of 795-825 nm of the two detectors used to detect the visible and NIR emission. The emission of the Xe lamp was then recorded with each detector at three different wavelengths within this region, using the same slits, and corrected using the correction file for the integrating sphere and the two detectors. Comparing the total recorded emission revealed a strong correlation between the two measurements, i.e. the photomultiplier tube (PMT) used to record the visible emission was ~4.6 times more sensitive after taking the correction files into account, as shown to the left in **Figure 5.17**. In order to compare the emission recorded by the two detectors, the emission detected by the NIR detector was multiplied by 4.6. The quantum efficiency measurement could then be conducted by measuring the UV emission escaping the sphere with and without the sample, followed by measuring the escaped visible and NIR emission shown the right in **Figure 5.17**. This resulted in a quantum efficiency of ~15% for a sample with 1 pulse% $Yb(thd)_3$ deposited on fused silica and annealed for 1 hour. As the availability of the measurement technique was limited, only one sample was characterised.

Comparison with the PL measurements indicate that the sample with 4 pulse% $Yb(thd)_3$ should have a quantum efficiency above this. In the study by Xu *et. al.* [105], the sample with 10 mol% Yb^{3+} had a relative quantum efficiency of ~50% higher than the sample with 2 mol% Yb^{3+}, which indicates that the sample with 4 pulse% $Yb(thd)_3$ could have a

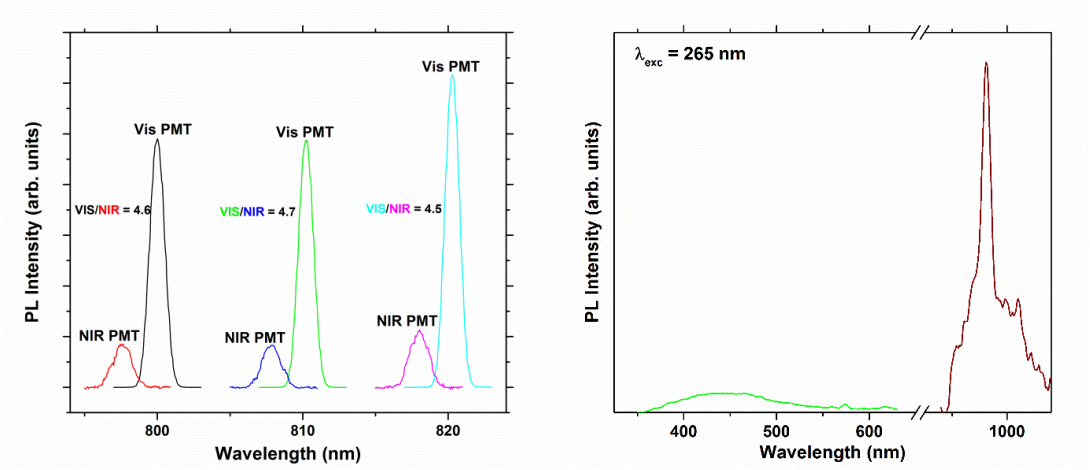

Figure 5.17: Left: Emission from the Xe900 lamp detected by NIR and visible PMT at three wavelengths in the 795-825 nm region after correcting for detector sensitivities. Right: Visible and NIR emission detected after correcting for detector sensitivities and multiplying NIR signal by 4.6.

quantum efficiency of around 20-25%. The measured quantum efficiencies are still very far off from the theoretical upper limit, however, they are still reasonable given that the samples were only annealed for 1 hour at 1000 °C and deposited with in-house made $VO(thd)_2$ and $Y(thd)_3$. This is in contrast to typical solid state processes where samples are usually annealed at higher temperatures and for several days, with the possibility of using high grade source materials. One of the samples made with $Y(thd)_3$ from Strem exhibited ~60% higher NIR emission than samples deposited using in-house made $Y(thd)_3$. This sample is in addition also much more transparent, as previously shown in **Figure 5.12**. While no quantitative number on the transmission could be measured as the sample was not deposited on fused silica, it is evident from the image that only around 25% of the surface is covered by crystals, which is partly due to a higher $VO(thd)_2$ pulse rate used for this sample. The absorption can consequently at most be 25%. Possible differences in refractive index and morphology between the samples makes it complicated to make an accurate estimate on the quantum efficiency, though with a 60% increase in PL emission, while the transmission is around 3 times larger, it seems likely that the quantum efficiency of this sample is significantly higher. This would explain the strong impurity signal observed in **Figure 5.11**. While the $Y(thd)_3$ from Strem may contain more lanthanide impurities, it is also evident that the energy transfer from $(VO_4)^{3-}$ is highly efficient in this sample, so that even trace impurities will produce easily detectable emission. Currently, my efforts of reproducing samples with similar PL emission on fused silica have not been successful, though at this point it is evident that there are reasons to be optimistic about the possibility to enhance the efficiency of solar cells using this material.

One of the advantages of ALD is the possibility of making layered materials, which for instance could be functionally similar to core-shell structures of nanoparticles [54-56]. This would require a sub-nanometre doping profile of crystalline material. Creating a multi-layered film of crystalline YVO_4 or $YbVO_4$ seemed challenging at this point due to the film structure collapsing during the crystallization process. It was nevertheless interesting to determine the temperature at which the Y and Yb atoms from the different pulses start to mix and whether it could be possible to obtain crystalline layers below this temperature.

The easiest way to achieve a multi-layered crystalline film would be to grow it as-deposited. This would require the film to have the correct stoichiometry and then would need to be deposited at the highest temperature possible. A test deposition at 310 °C resulted in films with large gradients, indicating that the growth was not self-limiting. However, deposition at 300 °C yielded smooth films and was selected as the deposition temperature for the layered thin films. Two samples were made with alternating layers of $YbVO_4$ and YVO_4. One was deposited with 25 consecutive supercycles of $Y(thd)_3/O_3/VO(thd)_2/O_3$ followed by 25 consecutive supercycles of $Yb(thd)_3/O_3/VO(thd)_2/O_3$, and the other one with a 100:100

pulse ratio between $Y(thd)_3$ and $Yb(thd)_3$. The layer thicknesses were selected so that they would be detectable by XRR. XRD revealed that the samples were indeed crystalline already as deposited, as shown in **Figure 5.18**. The results also showed that the crystallinity, and hence the luminescence properties, could be enhanced by annealing. XRR was performed in order to determine the upper-limit temperature at which the as-deposited doping profile could be maintained. The results are presented in **Figure 5.19**. The 25:25 sample could be heated up to 750 °C for 10 min in air before the signal was completely dominated by noise and no clear peak could be observed. The 100:100 sample on the other hand, still had detectable layered structure at 800 °C. **Figure 5.20** shows that the sample is indeed a cohesive film.

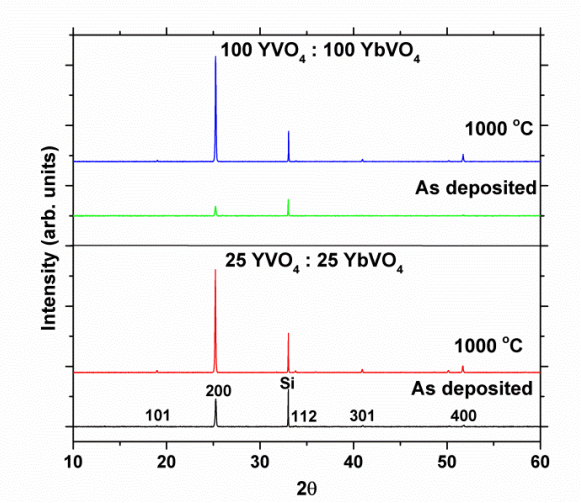

Figure 5.18: XRD of a samples with 25:25 and 100:100 pulse ratio of $Y(thd)_3/O_3/VO(thd)_2/O_3$ and $Yb(thd)_3/O_3/VO(thd)_2/O_3$, as-deposited and after annealing for 1 hour at 1000 °C.

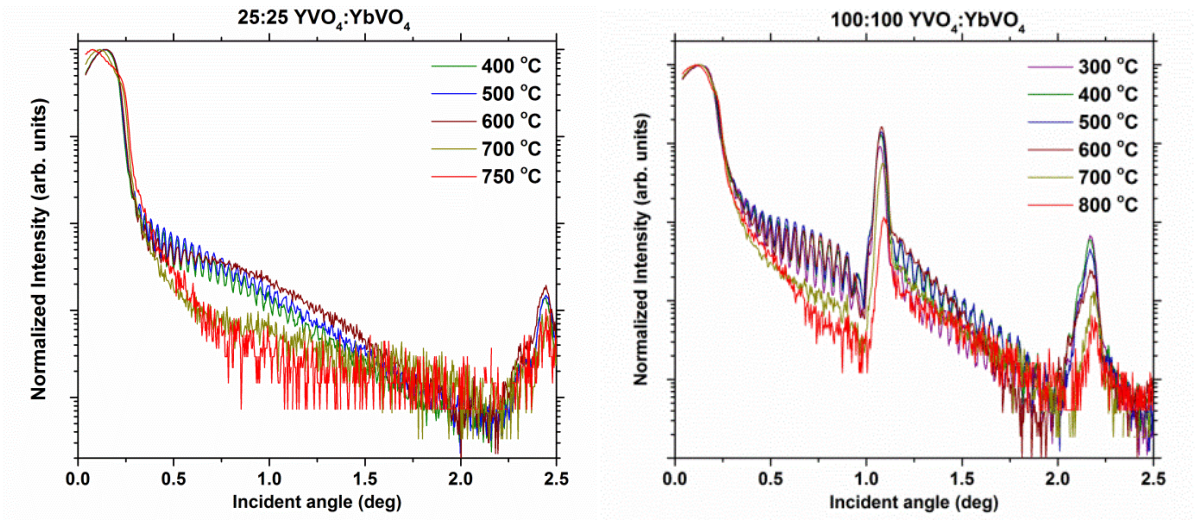

Figure 5.19: XRR measurements of samples with 25:25 (left) and 100:100 (right) cycle sequence of $Y(thd)_3/O_3/VO(thd)_2/O_3$ and $Yb(thd)_3/O_3/VO(thd)_2/O_3$.

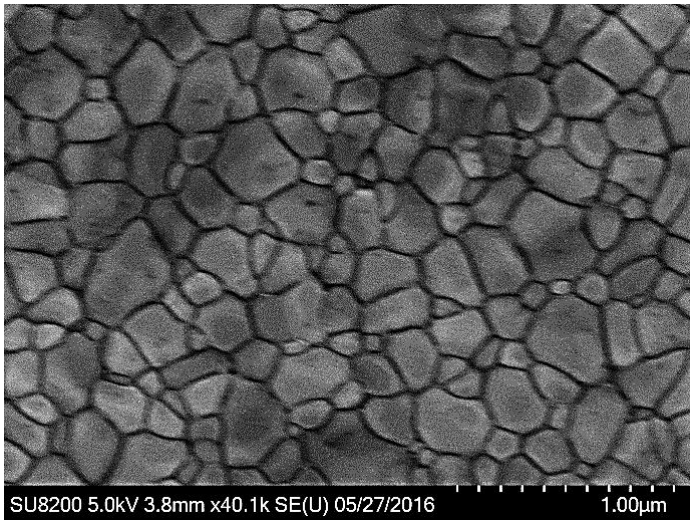

Figure 5.20: Sample with 100:100 supercycles YVO_4:$YbVO_4$ annealed at 800 °C for 10 min.

The results indicate that it is possible to deposit a layered material with sub-nanometre layer thicknesses using either YVO_4 or $YbVO_4$ as one of the building blocks. The $YbVO_4$ can be replaced by basically any $LnVO_4$ and it should thus be possible to grow a layered structure where the emission spectra can be designed by adjusting the layer thickness of the various layers in order to suit the desired application. This is particularly useful for applications where a combination of wavelengths is desired, like in artificial lighting. That it is possible to deposit crystalline YVO_4 also bodes well for similar materials like YPO_4, which might be more suited in combination with certain lanthanides.

While we were not able to obtain definite proof of whether the energy transfer in YVO_4:Yb^{3+} occurs via CET, this is very challenging, and probably the only proof that would in fact prove this beyond a doubt, would be a quantum efficiency measurement demonstrating >100% quantum efficiency. The results suggest that this could indeed be achievable, and might even be possible in the near future, provided that research on YVO_4:Yb^{3+} thin films is continued. The material could thus be useful for increasing the light-harvesting capabilities of solar cells, in addition to being useful for a wide range of other applications where intense NIR emission is desirable.

Chapter 6 – Summarizing discussion and outlook

The results presented in chapter 5 provide several indications that deposition of a thin film exhibiting a one-to-two photon conversion has been achieved, though we were not able to obtain conclusive evidence. Additional research is required in order to reach our goal of developing a thin film able to enhance the efficiency of solar cells, though the results in this study indicate that YVO_4:Yb^{3+} thin films deposited by ALD have the potential to exceed 100% quantum efficiency. It is thus my interpretation that it is possible to reach this goal using this material eventually.

In comparison with other options for light conversion, like Tb^{3+}–Yb^{3+} [42, 103, 107] Tm^{3+}–Yb^{3+} [107], Pr^{3+}–Yb^{3+} [100, 107], Er^{3+}–Yb^{3+} [108] or Bi^{3+}-Yb^{3+} [90, 109], it seems YVO_4:Yb^{3+} is the best option. A general problem with Yb^{3+} is that it is easily reduced, while Ce^{3+}, Pr^{3+} and Tb^{3+} are easily oxidized, resulting in RE^{4+}-RE^{2+} charge transfer states (CTS) that links the excited states, resulting in a possible decay pathway that competes with CET above certain excitation wavelengths in these systems. As CET is a second order process it is very slow and will always lose to a first order process, so sunlight with enough energy to reach the CTS will only result in a one-to-one conversion. Viable options for downconversion for use in photovoltaics thus only include sensitizers that are difficult or impossible to oxidize. Bi^{3+} resembles $(VO_4)^{3-}$ in many ways by having a spin-forbidden transition from which CET to two Yb^{3+} may take place and is a widely used as a sensitizer for lanthanides [88-91]. However, Bi^{3+} can be oxidized to Bi^{5+} (E_o = 1.59 eV) by reducing two Yb^{3+} (E_o = -1.05 eV), which means that the Bi^{5+}-Yb^{2+} CTS could be reachable from the Bi^{3+} excited states, depending on the symmetry and the chemical environment. Bi^{3+} might thus also be poorly suited in combination with Yb^{3+} for solar cell applications. Vanadium in $(VO_4)^{3-}$ on the other hand, is already in its highest oxidation state and there can consequently not be any CTS that compete with the CET process. Other similar options we considered, like Y_2MoO_6 and Y_2WO_6, do not exhibit an excited state from which resonant CET to Yb^{3+} is possible. Looking forward, the best option for downconversion consequently appears to be YVO_4:Yb^{3+} and the focus should be to either present definite proof of CET being the dominant energy transfer mechanism, or to maximize quantum efficiency and determine whether >100% is possible.

Both options are challenging, and it might be that the only sufficient proof of downconversion taking place for a large portion of the UV-part of the solar spectrum would be a sample exhibiting QE >100% under these conditions.

When it comes to optimizing the quantum efficiency, there are several parameters to investigate. While it is important that the Yb^{3+} concentration is not too high, the results indicate that it is the energy transfer from $(VO_4)^{3-}$ that is the most challenging factor for enabling high quantum efficiency. Both factors are certainly important, but the quantum efficiency can never be great, even if concentration quenching can be completely avoided, if the energy transfer from $(VO_4)^{3-}$ is poor. Efforts must thus be focused on reducing the quenching on $(VO_4)^{3-}$ as opposed to Yb^{3+}. Most studies on lanthanides focus on determining the optimum Ln-concentration in the respective host material, and while this is enlightening as to the effect of concentration quenching, I believe a more fruitful approach in the case of $YVO_4:Yb^{3+}$ would be to determine parameters that affect the crystallinity. A study comparing different synthesis methods or different source materials, annealing temperatures, ramp rates or stoichiometries would provide better understanding of how to optimize the luminescence efficiency. In this study, we have already determined that excess V_2O_5 is highly beneficial and that the chemical purity of the $Y(thd)_3$ source material is extremely important with respect to the quantum efficiency of the final product. While increased annealing temperatures have generally resulted in stronger NIR emission for this system, it is possible that lower annealing temperatures, but significantly longer annealing times, could provide even stronger emission. Intrinsic defect formation is increased at higher temperatures, and longer annealing times at lower temperatures could thus be beneficial, depending on whether these defects can quench the $(VO_4)^{3-}$ emission. Grain boundaries and surfaces usually contain charged defects, which are very efficient quenching centres, so determining synthesis methods that increase the size of the crystals could result in increased quantum efficiencies.

At this point it is evident that using ALD is very appealing due to the number of options available. While it might eventually be possible to synthesize powders of $YVO_4:Yb^{3+}$ that display high quantum efficiency, if the goal is to be able to deposit the material on a solar cell, it is crucial that it is possible to deposit it as a films that still exhibits the required quantum efficiency due to the adverse light scattering associated with powders. Continuing research using samples made by ALD might consequently be the most efficient method for actually obtaining a useful product.

When it comes to enhancing the efficiency of solar cells, efficient downconversion is the ultimate goal. However, for several applications, the efficiency of the phosphor is irrelevant and only the wavelengths that are absorbed and the wavelengths that are emitted matter. The option of making crystalline layered structures with ALD where the energy transfer between the layers in the material can be controlled offers a wide range of

possibilities to be explored and will certainly be important for current or future applications that require the material to be a thin film. The possibility of using YVO_4 and $YbVO_4$ as building blocks in such materials is particularly exciting as Yb^{3+} can be replaced by any Ln^{3+} that can be deposited by ALD, thus enabling a tremendous number of different emission spectra, which could for instance be used to produce an ultrathin white LED.

The fine control offered by the ALD-technique also allows for depositing amorphous luminescent materials with unique optical properties. The study on europium titanium phosphate revealed that it is possible to deposit a highly amorphous inorganic luminescent material, exhibiting a unique form of reversible photobleaching, and does not seem to follow any of the models describing such processes in the literature. Depositing other combinations of host materials and lanthanides with ALD could give rise to other amorphous materials with other distinctive properties. It is thus my belief that continued use of ALD to make luminescent materials is likely to lead to films with high quantum efficiency, as well as novel materials with unique optical properties.

Chapter 7 – References

1. Joubert, M.-F., *Photon avalanche upconversion in rare earth laser materials.* Optical Materials, 1999. **11**(2/3): p. 181-203.
2. Bunzli, J.-C.G. and C. Piguet, *Taking advantage of luminescent lanthanide ions.* Chemical Society Reviews, 2005. **34**(12): p. 1048-1077.
3. Yanagida, T., *Study of rare-earth-doped scintillators.* Optical Materials, 2013. **35**(11): p. 1987-1992.
4. Cavouras, D., *et al.*, *An evaluation of the Y2O3:Eu3+ scintillator for application in medical x ‐ ray detectors and image receptors.* Medical Physics, 1996. **23**(12): p. 1965-1975.
5. Klampaftis, E., *et al.*, *Enhancing the performance of solar cells via luminescent down-shifting of the incident spectrum: A review.* Solar Energy Materials and Solar Cells, 2009. **93**(8): p. 1182-1194.
6. Trupke, T., M.A. Green, and P. Würfel, *Improving solar cell efficiencies by down-conversion of high-energy photons.* Journal of Applied Physics, 2002. **92**(3): p. 1668-1674.
7. PV-Eductation.org. *Fill Factor*. [cited 09.11.16]; Available from: http://pveducation.org/pvcdrom/4-solar-cell-operation/fill-factor.
8. Shockley, W. and H.J. Queisser, *Detailed balance limit of efficiency of p-n junction solar cells.* Journal of Applied Physics, 1961. **32**: p. 510-19.
9. Richter, A., M. Hermle, and S.W. Glunz, *Reassessment of the Limiting Efficiency for Crystalline Silicon Solar Cells.* IEEE Journal of Photovoltaics, 2013. **3**(4): p. 1184-1191.
10. Bullis, K., *Record-Breaking Solar Cell Points the Way to Cheaper Power*. 2014, MIT Technology Review.
11. Panasonic. *Panasonic Quickly Beats SolarCity's Solar Module Efficiency Record*. 2015 [cited 09.12.2015]; Available from: http://cleantechnica.com/2015/10/09/panasonic-quickly-beats-solarcitys-solar-module-efficiency-record/.
12. Chen, J.Y., *et al.*, *Efficiency improvement of Si solar cells using metal-enhanced nanophosphor fluorescence.* Solar Energy Materials and Solar Cells, 2014. **120, Part A**: p. 168-174.
13. *New world record for solar cell efficiency at 46% French-German cooperation confirms competitive advantage of European photovoltaic industry*. 2014, Fraunhofer-ISE: https://www.ise.fraunhofer.de/en/press-and-media/press-releases/press-releases-2014/new-world-record-for-solar-cell-efficiency-at-46-percent.
14. IPCC. *Climate change 2013: the physical science basis*. 2013 [cited 21.01.2016]; Available from: : http://www.climatechange2013.org/report/.
15. IPCC. *Climate change 2014: impacts, adaptation, and vulnerability. Part A: Global and sectoral aspects*. 2014 [cited 21.01.2016]; Available from: http://ipcc-wg2.gov/AR5/.
16. Oreskes, N., *The Scientific Consensus on Climate Change.* Science, 2004. **306**(5702): p. 1686-1686.
17. Garnaut, R., *The Garnaut climate change review.* Cambridge University Press, 2008.
18. Arvizu, D., *et al.*, *Direct Solar Energy*, in *IPCC Special Report on Renewable Energy Sources and Climate Change Mitigation*, O. Edenhofer, *et al.*, Editors. 2011, Cambridge University Press: Cambridge, United Kingdom and New York, NY, USA.
19. Omedo, C.I. *Solar Panels Covering Spain can Power the World, Elon Musk Says*. 2015.
20. Maehlum, M.A., *How Much Do Solar Panels Cost*. 2015, Energy Informative: http://energyinformative.org/solar-panels-cost/.
21. Solar-Power-Europe-Association. *Global Market Outlook for Solar Power 2015-2019*. 2015 [cited 18.01.2016].
22. SEMI, *International Technology Roadmap for Photovoltaic 2014 Results.* 2015.
23. Johnson, R.W., A. Hultqvist, and S.F. Bent, *A brief review of atomic layer deposition: from fundamentals to applications.* Materials Today, 2014. **17**(5): p. 236-246.
24. Picosun. *P-1000 Pro technical features*. [cited 08.04.2016]; Available from: http://www.picosun.com/en/products/picosun8482+p-series/p-1000+pro+technical+features/.

References

25. Hansen, P.-A., *et al.*, *Luminescence properties of europium titanate thin films grown by atomic layer deposition.* RSC Advances, 2014. **4**(23): p. 11876-11883.
26. Hansen, P.-A., *et al.*, *Luminescent Properties of Multilayered Eu2O3 and TiO2 Grown by Atomic Layer Deposition***.* Chemical Vapor Deposition, 2014. **20**(7-8-9): p. 274-281.
27. Wei, X., *et al.*, *Energy transfer mechanisms in Yb3+ doped YVO4 near-infrared downconversion phosphor.* Journal of Applied Physics, 2010. **107**(10): p. 103107.
28. Cheng, X., *et al.*, *Near-infrared quantum cutting in YVO4:Yb3+ thin-films via downconversion.* Optical Materials, 2012. **34**(7): p. 1102-1106.
29. Pugliesi, D. and M0tty. [cited 08.01.2016]; Available from: https://en.wikipedia.org/wiki/Chlorophyll#/media/File:Chlorophyll_ab_spectra-en.svg.
30. Mehraj, H. *Leaves*. [cited 08.01.16]; Available from: http://hmehraj.blog.com/2013/05/29/leaves/.
31. Cotton, S., *Lanthanide and actinide chemistry*. 2006, Chichester, England; Hoboken, NJ: Wiley.
32. Dieke, G.H. and H.M. Crosswhite, *The Spectra of the Doubly and Triply Ionized Rare Earths.* Applied Optics, 1963. **2**(7): p. 675-686.
33. Werts, M.H.V., *Making sense of lanthanide luminescence.* Science Progress, 2005. **88**(2): p. 101-131.
34. Atkins, P., *et al.*, *Shriver & Atkins Inorganic Chemistry Forth Edition*. 2006: Oxford.
35. Phosphor-Research-Society, *Phosphor handbook*. 1999, Boca Raton, FL, : CRC Press.
36. Chambers, M.D. and D.R. Clarke, *Doped oxides for high-temperature luminescence and lifetime thermometry.* Annual Review of Materials Research, 2009. **39**: p. 325-359.
37. Gentleman, M.M., *High temperature sensing of thermal barrier materials by luminescence*. 2006. p. 147 pp.
38. Zhang, F., *Photon Upconversion Nanomaterials*. 2015, Berlin, Heidelberg: Springer.
39. Rademaker, K., *Rare Earth-doped Alkali-lead-halide Laser Crystals of Low-phonon Energy*. 2005, University of Hamburg: Hamburg. p. 37.
40. Forster, T., *Intermolecular energy transference and fluorescence.* Annalen der Physik, 1948. **2**(6): p. 55-75.
41. Rabouw, F., *Before there was light: Excited state dynamics in luminescent (nano)materials*. 2015, University of Utrecht.
42. Vergeer, P., *et al.*, *Quantum cutting by cooperative energy transfer in YbxY1-xPO4:Tb3+*. Physical Review B: Condensed Matter and Material Physics, 2005. **71**(1): p. 014119/1-014119/11.
43. van Wijngaarden, J.T., *et al.*, *Energy transfer mechanism for downconversion in the (Pr3+, Yb3+) couple.* Physical Review B: Condensed Matter and Material Physics, 2010. **81**(15): p. 155112/1-155112/6.
44. Piper, W.W., J.A. DeLuca, and F.S. Ham, *Cascade fluorescent decay in praseodymium (3+)-doped fluorides. Achievement of a quantum yield greater than unity for emission of visible light.* Journal of Luminescence, 1974. **8**(4): p. 344-8.
45. Suntola, T. and J. Antson, *Apparatus and method for growing thin compound films*. 1976, Instrumentarium Oy, Finland . p. 30 pp.
46. Puurunen, R.L., *A Short History of Atomic Layer Deposition: Tuomo Suntola's Atomic Layer Epitaxy.* Chemical Vapor Deposition, 2014. **20**(10-11-12): p. 332-344.
47. Sveshnikova, G.V., S.I. Kol'tsov, and V.B. Aleskovskii, *Fabrication of a layer of silicon dioxide of a given thickness on the surface of silicon by molecular lamination.* Zhurnal Prikladnoi Khimii, 1970. **43**(5): p. 1150-2.
48. Miikkulainen, V., *et al.*, *Crystallinity of inorganic films grown by atomic layer deposition: Overview and general trends.* Journal of Applied Physics, 2013. **113**(2): p. 021301.
49. Hirvikorpi, T., *et al.*, *Atomic layer deposited aluminum oxide barrier coatings for packaging materials.* Thin Solid Films, 2010. **518**(10): p. 2654-2658.
50. Harkonen, E., *et al.*, *Corrosion protection of steel with oxide nanolaminates grown by atomic layer deposition.* Journal of The Electrochemical Society, 2011. **158**(11): p. C369-C378.
51. Heil, S.B.S., *et al.*, *In situ reaction mechanism studies of plasma-assisted atomic layer deposition of Al2O3.* Applied Physics Letters, 2006. **89**(13): p. 131505/1-131505/3.
52. Vee, I., *Fluorholdige hybridmaterialer med atomlagsavsetting: Syntese og karakterisering*. 2012, University of Oslo.
53. Nilsen, O., *et al.*, *Growth of La1-xCaxMnO3 thin films by atomic layer deposition.* Journal of Materials Chemistry, 2007. **17**(15): p. 1466-1475.
54. Zhou, B., *et al.*, *Constructing Interfacial Energy Transfer for Photon Up- and Down-Conversion from Lanthanides in a Core-Shell Nanostructure.* Angewandte Chemie International Edition, 2016. **55**(40): p. 12356-60.

55. Chen, G., *et al.*, *Core/Shell NaGdF4:Nd3+/NaGdF4 Nanocrystals with Efficient Near-Infrared to Near-Infrared Downconversion Photoluminescence for Bioimaging Applications.* ACS Nano, 2012. **6**(4): p. 2969-2977.
56. Zhu, W., *et al.*, *An active-core/active-shell structure with enhanced quantum-cutting luminescence in Pr-Yb co-doped monodisperse nanoparticles.* Nanoscale, 2014. **6**(18): p. 10500-10504.
57. Yu, D.C., *et al.*, *Insights into the energy transfer mechanism in Ce(3+)-Yb(3+) codoped YAG phosphors.* Physical Review B, 2014. **90**(16): p. 165126.
58. Hansen, P.-A., *et al.*, *Structural and optical properties of lanthanide oxides grown by atomic layer deposition (Ln = Pr, Nd, Sm, Eu, Tb, Dy, Ho, Er, Tm, Yb).* Dalton Transactions, 2013. **42**(30): p. 10778-10785.
59. Päiväsaari, J., *et al.*, *Atomic Layer Deposition of Rare Earth Oxides*, in *Rare Earth Oxide Thin Films*, M. Fanciulli and G. Scarel, Editors. 2007, Springer: Berlin Heidelberg. p. 15-32.
60. Hansen, P.-A., *et al.*, *Luminescence properties of lanthanide and ytterbium lanthanide titanate thin films grown by atomic layer deposition.* Journal of Vacuum Science & Technology A: Vacuum, Surfaces, and Films, 2015. **34**(1): p. 01A130.
61. Tammenmaa, M., *et al.*, *Zinc sulphide thin films doped with rare earth ions.* Journal of the Less Common Metals, 1986. **126**: p. 209-214.
62. Michael, C.P., *et al.*, *Growth, processing, and optical properties of epitaxial Er2O3 on silicon.* Optics Express, 2008. **16**(24): p. 19649-19666.
63. Hoang, J., *et al.*, *Optical properties of Y2O3 thin films doped with spatially controlled Er3+ by atomic layer deposition.* Journal of Applied Physics, 2007. **101**(12): p. 123116.
64. Hoang, J., *et al.*, *Er3+ interlayer energy migration as the limiting photoluminescence quenching factor in nanostructured Er3+:Y2O3 thin films.* Journal of Applied Physics, 2012. **112**(2): p. 023116.
65. Hoang, J., *et al.*, *The effects of energy transfer on the Er3+ 1.54 μm luminescence in nanostructured Y2O3 thin films with heterogeneously distributed Yb3+ and Er3+ codopants.* Journal of Applied Physics, 2012. **112**(6): p. 063117.
66. Dingemans, G., *et al.*, *Er3+ and Si luminescence of atomic layer deposited Er-doped Al2O3 thin films on Si(100).* Journal of Applied Physics, 2011. **109**(11): p. 113107.
67. Tuomisto, M., *et al.*, *Photon up-converting (Yb,Er)2O3 thin films by atomic layer deposition.* physica status solidi (RRL) – Rapid Research Letters, 2017: p. 1700076-n/a.
68. Perkowitz, S., *Optical Characterization of Semiconductors; Infrared, Raman, and Photoluminescence Spectroscopy* Techniques of Physics. 1993: Elsevier Ltd.
69. Aoki, T., *Photoluminescence Spectroscopy*, in *Characterization of Materials*. 2002, John Wiley & Sons, Inc.
70. Ronda, C., *Luminescence: From Theory to Applications.* Wiley-Vch, 2008: p. 13-20.
71. Perkampus, H.-H., *UV-VIS Spectroscopy and Its Applications*. 1992: Springer Berlin Heidelberg.
72. Demas, J.N. and G.A. Crosby, *Photoluminescence decay curves: an analysis of the effects of flash duration and linear instrumental distortions.* Analytical Chemistry, 1970. **42**(9): p. 1010-1017.
73. Tompkins, H.G. and J.N. Hilfiker, *Spectroscopic Ellipsometry: Practical Application to Thin Film Characterization* 2016, Chennai, India: Momentum Press.
74. Yoshio Waseda, Eiichiro Matsubara, and K. Shinoda, *X-Ray Diffraction Crystallography: Introduction, Examples and Solved Problems*. 2011, Berlin Heidelberg: Springer.
75. Beckhoff, B., Kanngießer, B., Langhoff, N., Wedell, R., Wolff, H. , *Handbook of Practical X-Ray Fluorescence Analysis*. 2006: Springer Berlin Heidelberg.
76. Jens Als-Nielsen, D.M., *Elements of Modern X-ray Physics*. 2nd ed. 2011, New York: Wiley.
77. Daillant, J. and A. Gibaud, *X-ray and Neutron Reflectivity: Principles and Applications*. 2009: Springer Berlin Heidelberg.
78. Kazmiruk, V., *Scanning Electron Microscopy*. 2012, http://www.intechopen.com/: InTech.
79. Haugstad, G., *Atomic Force Microscopy: Understanding Basic Modes and Advanced Applications*. 2012, http://onlinelibrary.wiley.com/book/10.1002/9781118360668: Wiley.
80. Firstov, S., *et al.*, *Photobleaching effect in bismuth-doped germanosilicate fibers.* Optics Express, 2015. **23**(15): p. 19226-19233.
81. Elliott, S.R., *A unified model for reversible photostructural effects in chalcogenide glasses.* Journal of Non-Crystalline Solids, 1986. **81**(1): p. 71-98.
82. Mendes, A.C., *et al.*, *Photoexpansion and photobleaching effects in oxysulfide thin films of the GeS2+Ga2O3 system.* Physica B: Condensed Matter, 2011. **406**(23): p. 4381-4386.
83. Nalin, M., *et al.*, *Photosensitivity in antimony based glasses.* Journal of Optoelectronics and Advanced Materials, 2001. **3**(2): p. 553-558.
84. De Vicente, F.S., *et al.*, *Photoinduced structural changes in antimony polyphosphate based glasses.* Journal of Non-Crystalline Solids, 2003. **330**(1–3): p. 168-173.

References

85. Nalin, M., *et al.*, *Antimony oxide based glasses.* Journal of Non-Crystalline Solids, 2001. **284**(1–3): p. 110-116.
86. Dexpert-Ghys, J., R. Mauricot, and M.D. Faucher, *Spectroscopy of Eu3+ ions in monazite type lanthanide orthophosphates LnPO4, Ln = La or Eu.* Journal of Luminescence, 1996. **69**(4): p. 203-215.
87. Schwartz, K., *The Physics of Optical Recording*. 1993, Berlin: Springer.
88. Chen, D., *et al.*, *Color-tunable luminescence for Bi3+/Ln3+:YVO4 (Ln = Eu, Sm, Dy, Ho) nanophosphors excitable by near-ultraviolet light.* Physical Chemistry Chemical Physics, 2010. **12**(28): p. 7775-7778.
89. Iso, Y., S. Takeshita, and T. Isobe, *Effects of Annealing on the Photoluminescence Properties of Citrate-Capped YVO4:Bi3+,Eu3+ Nanophosphor.* The Journal of Physical Chemistry C, 2014: p. Ahead of Print.
90. Huang, X.Y. and Q.Y. Zhang, *Near-infrared quantum cutting via cooperative energy transfer in Gd2O3:Bi3+,Yb3+ phosphors.* Journal of Applied Physics, 2010. **107**(6): p. 063505.
91. Xu, W., *et al.*, *YVO4:Eu3+,Bi3+ UV to visible conversion nano-films used for organic photovoltaic solar cells.* Journal of Materials Chemistry, 2011. **21**(33): p. 12331-12336.
92. Ding, X., *et al.*, *High-efficiency direct-pumped Nd:YVO4 laser operating at 1.34 microm.* Optics Express, 2008. **16**(15): p. 11247-52.
93. Østreng, E., O. Nilsen, and H. Fjellvåg, *Optical Properties of Vanadium Pentoxide Deposited by ALD.* The Journal of Physical Chemistry C, 2012. **116**(36): p. 19444-19450.
94. Ronde, H. and G. Blasse, *The nature of the electronic transitions of the vanadate group.* Journal of Inorganic and Nuclear Chemistry, 1978. **40**(2): p. 215-219.
95. van Pieterson, L., *et al.*, *Charge transfer luminescence of Yb3+.* Journal of Luminescence, 2000. **91**(3–4): p. 177-193.
96. Wanmaker, W.L., *et al.*, *Luminescent properties of europium-activated phosphors of the type A(III)B(V)O4.* Philips Research Reports, 1966. **21**(4): p. 270-82.
97. Singh, N.S., *et al.*, *Luminescence, lifetime and quantum yield studies of YVO4:Ln3+ (Ln3+ = Dy3+, Eu3+) nanoparticles: Concentration and annealing effects.* Chemical Physics Letters, 2009. **480**(4–6): p. 237-242.
98. Chander, N., *et al.*, *Reduced ultraviolet light induced degradation and enhanced light harvesting using YVO4:Eu3+ down-shifting nano-phosphor layer in organometal halide perovskite solar cells.* Applied Physics Letters, 2014. **105**(3): p. 033904.
99. Lau, M.K. and J.-H. Hao, *Near-infrared Quantum Cutting in Eu3+-Yb3+ co-doped YAG through Downconversion for Silicon Solar Cell.* Energy Procedia, 2012. **15**: p. 129-134.
100. Aarts, L., *et al.*, *Downconversion for Solar Cells in YF3:Pr3+, Yb3+.* Spectroscopy Letters, 2010. **43**(5): p. 373-381.
101. Chen, D., *et al.*, *Ultraviolet-blue to near-infrared downconversion of Nd3+-Yb3+ couple.* Optics Letters, 2010. **35**(2): p. 220-222.
102. Xu, S., *et al.*, *Downconversion from visible to near infrared through multi-wavelength excitation in Er3+/Yb3+ co-doped NaYF4 nanocrystals.* Journal of Applied Physics, 2011. **110**(11): p. 113113.
103. Fu, L., *et al.*, *Cooperative down-conversion luminescence in Tb3+/Yb3+ co-doped LiYF4 single crystals.* IEEE Photonics Journal, 2014. **6**(1): p. 2600209/1-2600209/10, 10 pp.
104. Hammond, G.S., D.C. Nonhebel, and C.-H.S. Wu, *Chelates of β-diketones. V. Preparation and properties of chelates containing sterically hindered ligands.* Inorganic Chemistry, 1963. **2**: p. 73-6.
105. Xu, S., *et al.*, *A strategy for calibrating the actual quantum efficiency of quantum cutting in YVO4:Bi3+(Nd3+),Yb3+.* Journal of Applied Physics, 2013. **113**(7): p. 073101/1-073101/5.
106. Thakur, S. and A. K Gathania, *Optical properties of YVO4:Eu3+ nano-phosphors at different europium concentrations.* Indian Journal of Physics, 2015. **89**(9): p. 973-979.
107. Zhang, Q.Y., G.F. Yang, and Z.H. Jiang, *Cooperative downconversion in GdAl3(BO3)4:RE3+,Yb3+ (RE=Pr, Tb, and Tm).* Applied Physics Letters, 2007. **91**(5): p. 051903.
108. Rakov, N. and G.S. Maciel, *Near-infrared quantum cutting in Ce3+, Er3+, and Yb3+ doped yttrium silicate powders prepared by combustion synthesis.* Journal of Applied Physics, 2011. **110**(8): p. 083519.
109. Qu, M., *et al.*, *Broadband near infrared quantum cutting in Bi–Yb codoped Y2O3 transparent films on crystalline silicon.* Journal of Luminescence, 2012. **132**(5): p. 1285-1289.

I

Luminescent properties of europium titanium phosphate thin films deposited by atomic layer deposition

RSC Advances, 2017, **7**, 8051

Michael N. Getz, Per-Anders Hansen, Helmer Fjellvåg and Ola Nilsen

RSC Advances

PAPER

View Article Online
View Journal | View Issue

Cite this: *RSC Adv.*, 2017, **7**, 8051

Luminescent properties of europium titanium phosphate thin films deposited by atomic layer deposition†

Michael N. Getz, Per-Anders Hansen, Helmer Fjellvåg and Ola Nilsen*

In the present contribution we assess the luminescent properties of amorphous europium titanium phosphate thin films. The films have been deposited by atomic layer deposition, using the precursor combinations $Eu(thd)_3$ (thd = 2,2,6,6-tetramethyl-3,5-heptanedione) and O_3, $TiCl_4$ and H_2O, and Me_3PO_4, H_2O and O_3 at a deposition temperature of 300 °C. UV light is absorbed in the $(TiO_6)^{8-}$ complex and subsequently transferred to Eu^{3+}, from which characteristic visible red emission takes place. The inclusion of phosphate is expected to reduce the symmetry around Eu^{3+} compared to the pure oxide structure, which should increase the f–f transition rate and improve the luminescence efficiency. The as deposited samples display a high degree of photobleaching when subjected to UV or X-rays. The bleaching rate has been quantified for the as deposited samples and can be controlled by adjusting the Ti-content in the samples. Annealing the samples at 500–700 °C increases both the photostability and the luminescence of all compositions, while annealing at 800 °C and above quenches the Eu^{3+} luminescence. Annealing at 1000 °C results in a broad NIR emission centred around 820 nm for most of the samples. The structure, roughness, thickness and composition of the deposited films have been studied by X-ray diffraction, atomic force microscopy, ellipsometry, and X-ray fluorescence, respectively. The optical properties have been characterized with excitation and photoluminescence spectroscopy and spectroscopic ellipsometry, while field emission scanning electron microscopy has been used to determine the morphology of the annealed samples.

Received 1st December 2016
Accepted 11th January 2017

DOI: 10.1039/c6ra27644j

www.rsc.org/advances

Introduction

Luminescent materials, and the lanthanides in particular, are key components in a wide range of applications, like lasers,[1] LEDs,[2,3] scintillators,[4] sensors[5] and biological markers.[6,7] The lanthanide oxides are thermodynamically very stable with high melting points, enabling applications at high temperatures and under harsh environments as well as bifunctional materials such as protective luminescent coatings.[8] They are also stable in contact with silicon, which is a requirement for silicon based technologies such as photovoltaics.[9]

One of the limiting factors in present silicon based photovoltaics is losses due to thermalization. These losses can be reduced by application of thin films of luminescent materials that convert UV photons to visible light. In this manner, the visible light can be tuned to better fit the optical absorption profile of the silicon solar cell and with an overall increase in efficiency.[10–12] However, in order to realise such implementations, highly efficient converter materials have to be produced as thin films or coatings. Chen *et al.* for instance observed an efficiency increase of a silicon cell from 17.1% to 17.7% by adding a luminescent UV conversion layer.[13] Another related application of such thin films is as coatings for green houses to increase crop growth.[14]

Eu^{3+} is known for its characteristic red luminescence and is able to convert UV to red. However, as the absorption bands of Eu^{3+} are narrow, it is common to incorporate it into hosts that can absorb UV light and then transfer the energy to Eu^{3+}, from which characteristic red emission takes place. In our current work the charge-transfer (CT) absorption of $(TiO_6)^{8-}$ is used as the absorbing material, and the energy is transferred to Eu^{3+} *via* Förster resonant energy transfer (FRET).

Atomic layer deposition (ALD) is a unique gas-phase deposition technique and is considered a powerful method for depositing thin and conformal films for ultra-scaled conventional and novel microelectronic devices at low temperatures.[15–17] The development of ALD processes for ternary and quaternary oxides has recently seen a rapid increase.[18–22]

We here demonstrate successful ALD synthesis of an amorphous europium titanium phosphate system ($Eu_xTi_yP_zO_u$), as an extension of our prior work on the luminescent properties of europium titanate thin films.[23,24] The inclusion of phosphate

Department of Chemistry, Centre for Materials Science and Nanotechnology, University of Oslo, Sem Sælandsvei 26, 0371 Oslo, Norway. E-mail: Ola.Nilsen@kjemi.uio.no

† Electronic supplementary information (ESI) available. See DOI: 10.1039/c6ra27644j

results in an increased emission, which is expected to be due to reduced symmetry of the lanthanide surroundings, increasing the spontaneous emission rate. As solid solubility between $EuPO_4$ and any Ti–P–O structure does not seem to occur, the samples are completely amorphous up to relatively high temperatures, before decomposing into multiple crystalline phases.

We also demonstrate materials exhibiting a decrease in emission while being subjected to UV light, *i.e.* a form of photobleaching. As this effect can be desirable or not, depending on the application it is intended for (UV stable or UV reactive), it is useful to determine if it can be controlled. Photobleaching is often related to reversible or irreversible photoinduced structural changes,[25–27] and if the changes are reversible, they can potentially be useful for applications like optical storage and holography.[28]

Experimental

The films were deposited with an F-120 research-type ALD-reactor (ASM Microchemistry Ltd) at 300 °C and at a reactor pressure of 2.2 mbar. The β-diketonate chelate $Eu(thd)_3$ (thd = 2,2,6,6-tetramethyl-3,5-heptanedione) (Strem Chemicals, >99.9%), was used as the europium precursor. $TiCl_4$ (Aldrich, >99.9%) was used as titanium precursor. Me_3PO_4 (Merck Chemicals, >98%) was used as the phosphorous precursor. Ozone was used as the oxygen source and was produced from >99.9% O_2 in an In USA ozone generator (AC-2025). Nitrogen was used as carrier and purge gas and was separated from air in a nitrogen generator (Schmidlin UHPN3001 N_2 purifier, >99.999% N_2 + Ar purity). All depositions were preceded by an *in situ* 30 minute ozone cleaning consisting of 300 cycles of 3 s O_3 pulse and 3 s N_2 purge at the deposition temperature in order to remove any organic remains.

The sublimation temperature used for $Eu(thd)_3$ was 145 °C. Pulse durations for the deposition of Eu_2O_3 layers were 1.5/1/4/1.5 s for $Eu(thd)_3$/purge/O_3/purge, respectively. For TiO_2, pulse durations were 0.95/2/1/1.5 s for $TiCl_4$/purge/H_2O/purge, while for the deposition of phosphate, a pulse duration of 2/3/0.5/2/0.5/2 s for Me_3PO_4/purge/H_2O/O_3 + H_2O/H_2O/purge was used. The Me_3PO_4 was kept at room temperature and assisted with N_2 carrier gas. The europium and titanium processes were previously described by Hansen *et al.*,[24] while the phosphate process was previously described by Gandrud *et al.*[29] and all the process parameters were chosen to be well within saturating conditions according to prior investigations of these binary systems on the same equipment.

The thickness of the native oxide layer on the silicon substrates ranged from 2–4 nm and was measured by spectroscopic ellipsometry before each deposition.

For each deposition, the following substrates were used: one 3 × 3 cm^2 Si substrate for X-ray fluorescence purpose, ten 0.5 × 0.5 cm^2 Si substrates for annealing purposes and photoluminescence measurements, and two 4 × 0.5 cm^2 Si substrates placed at the back and front of the reaction chamber to monitor the conformality of the films across the whole chamber.

The produced layers will in this article be referred to as EPO and TPO for europium phosphate and titanium phosphate layers respectively, with an EPO cycle consisting of one europium oxide cycle followed by one phosphate cycle. Similarly, TPO cycles are constructed from one titanium oxide cycle followed by a phosphate cycle. A complete cycle will thus be referred to as an MP-cycle, where M can be either Eu or Ti.

The composition of the samples was controlled by adjusting the EPO : TPO cycle ratio, *e.g.* 30 pulse% EPO was achieved by three pulses of EPO and seven pulses of TPO. The pulses were alternated in such a way that that the EPO cycles were as evenly distributed between the TPO cycles as possible. N pulse% EPO will be abbreviated N EPO from here on.

The film thickness was kept to *ca.* 100 nm in order for this parameter to have minimal impact on the properties of interest.

The crystallinity of the samples was determined with a Bruker D8 Discovery X-ray diffractometer, using $CuK_{\alpha 1}$ radiation and a Ge(111) monochromator. The film thickness, extinction coefficient and refractive index were determined with a J. A. Woollam variable angle spectroscopic ellipsometer (VASE) in the 270–1000 nm range. The Tauc–Lorentz formalism was used to model and parameterize the ellipsometry experimental data. The model utilizes two layers, one for the substrate and one for the thin film. Surface roughness, R_q, of the as deposited samples was measured with a Park XE70 atomic force microscope (AFM) in tapping mode over a 5 × 5 μm^2 area and with a scan rate of 0.4 Hz. The chemical composition was determined by X-ray fluorescence (XRF) on a Phillips PW2400 Spectrometer and interpreted with the Uniquant analysis software. Photoluminescence (PL) measurements were performed with a 325 nm, CdHe laser with a power of 0.16 W mm^{-2} and a USB4000 photospectrometer from OceanOptics in the 350–1000 nm range. The emission spectra are not calibrated for the detector sensitivity. For recording photoluminescence excitation spectra (PLE) and performing quantum efficiency measurements we used an Edinburgh Instruments FLS920 fluorescence spectrometer, using a 450 W Xe lamp as excitation source and a Hamamatsu R928 PMT with a grating blazed at 300 nm for detection. The quantum efficiency measurements were performed on samples deposited on silica substrates, using an integrating sphere. PL decay measurements were performed with an optical parametric oscillator (OPO) system (Opotek HE 355 II) pumped by the third harmonic of a Nd:YAG laser as excitation source. For the PL decay measurements, the OPO system was set at $\lambda_{exc} = 355$ nm, with a repetition rate of 20 Hz. The PL decay was recorded with the same equipment used for the excitation measurement.

The PL data shown in Fig. 5 was recorded with 20 s integration time after an initial 1–2 s of laser exposure, and averaged over two spots near the centre of the sample. The emission in general appeared to be independent of where the beam hit the sample with the exception of the edges and some of the samples annealed at 800–1000 °C, which is expected to be due to variance in surface roughness across the sample surface after being exposed to high temperatures. This is thus not expected to impact the conclusions drawn in this study.

A SU8230 field emission scanning electron microscope (FE-SEM) from Hitachi was used to study the surface morphology.

The 0.5 × 0.5 cm^2 substrates for the various compositions were annealed inside an open quartz ampoule in air in a tube furnace for 10 min at 400, 500, 600, 700, 800 and 1000 °C.

Results and discussion

At a deposition temperature of 300 °C, the deposition rate of EPO and TPO was determined to be 1.0 Å per MP-cycle and 0.8 Å per MP-cycle respectively. The cation concentrations and deposition rate of the as deposited samples are shown in Fig. 1. The thin films all appear to be conformal across the whole deposition chamber and the surface roughness, R_q, of all samples is less than 0.4 nm, as determined by AFM. Additional information about number of regular cycles, thickness, cation concentrations, and roughness of the samples is provided in Table S1.† XRD was performed to obtain structural information about the samples, and revealed that all of them were amorphous as deposited (300 °C). A few samples showed signs of crystallization at 900 °C, though most did not appear to crystallize before being annealed at 1000 °C (Fig. S1†), which is expected to be due to the lack of a stable Eu–Ti–P–O phase. The samples may contain grains too small to be detected in θ–2θ geometry at temperatures lower than what we observe by XRD, as small grains were observed by AFM for some samples below 1000 °C (Fig. S2 and S3†). Fig. 2 shows diffraction patterns for all compositions annealed at 1000 °C. All the peaks in the pattern of the sample containing 80 EPO were found to correspond to the $EuPO_4$ phase[30] (Fig. S4†), indicating that all the peaks from 50–90 EPO that overlap with these peaks also originate from this phase. The small peak observed at 53° for the 60 and 70 EPO samples could also belong to $EuPO_4$, though various titanium oxide phases also have a reflection at this point, making it unclear which phase is responsible. The peak at ~25° of the samples containing 20–40 EPO corresponds to anatase TiO_2.[31]

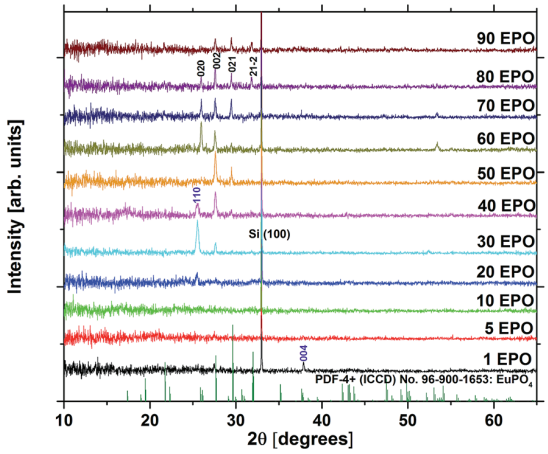

Fig. 2 X-ray diffraction patterns of all compositions annealed at 1000 °C. $EuPO_4$ reflections are highlighted in black, while anatase TiO_2 reflections are highlighted in purple.

The extinction coefficient, k, and refractive index, n, are important parameters that describe how the samples interact with light and are crucial in determining whether the material can be used for applications, such as a conversion layer for solar cells. Approximations of these parameters were determined for the as deposited samples using ellipsometry and the resulting data are presented in Fig. 3. It is evident that both n and k increase with increased TPO pulsing, demonstrating that the growth can be controlled by ALD. The UV-absorption is rather weak, particularly for samples with low Ti-content, which means that a thick layer would be required for applications where UV to visible conversion is desired.

The excitation and emission spectra were recorded in order to compare the shape and emission intensity of the samples. This is shown for one of the most emissive samples in Fig. 4. The shape of the spectrum was identical for all the as deposited

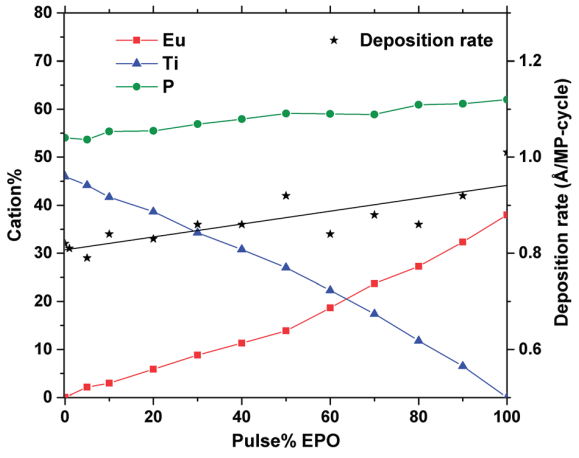

Fig. 1 Cation% and deposition rate *vs.* pulse% EPO of as deposited samples, as determined by XRF and ellipsometry.

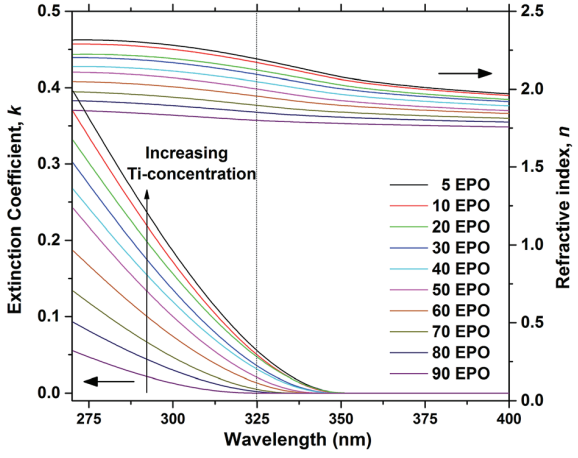

Fig. 3 Extinction coefficient, k, and refractive index, n, as a function of wavelength, shown for as deposited samples. The dotted line shows the wavelength of the laser used in the PL measurements.

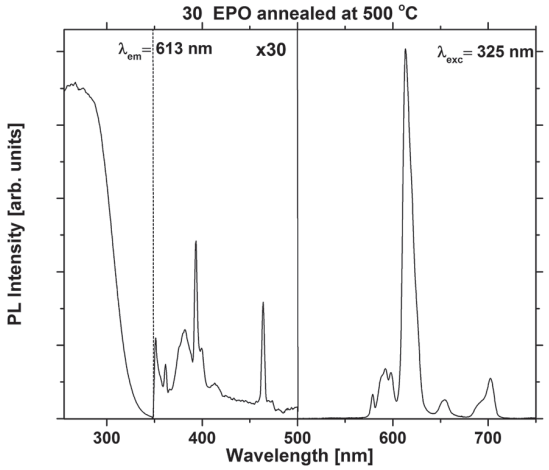

Fig. 4 PLE and PL spectra of a 30 EPO sample annealed at 500 °C.

samples (Fig. S5 and S6†), suggesting that the local coordination around Eu^{3+} is independent of composition for this set of samples. Additional excitation and emission spectra for samples annealed at 500 °C can be found in Fig. S7.†

Fig. 5 shows the total emission intensity of every sample plotted against the pulse% EPO and annealed at increasing temperatures up to 800 °C. The overall trend appears to be that annealing at 500–700 °C increases the luminescence of every sample significantly, while annealing at 800 °C quenches it. The photostability under UV or X-ray illumination of the as deposited samples and the samples annealed at 400 °C was poor in general (Fig. S8†), particularly for the samples with 30 EPO or less. The long integration time required to obtain reproducible results (20 s) thus had a significant impact on the detected emission from these samples. The luminescence of the samples could be completely recovered by tempering at 300 °C for 1 h, proving the process to be reversible (Fig. S9†). Reversible photostructural effects are well documented in amorphous chalcogenides,[27,32] and has previously been observed in amorphous Sb_2O_3–$SbPO_4$,[26] as well as crystalline $Tb_3Ga_5O_{12}$:Eu^{3+}.[33] The mechanisms governing these processes are not fully understood and several models have been proposed,[26,27] though, it has not been possible to verify if the EPO–TPO system follows any of these models. The emission did not recover by keeping the samples in the dark for any amount of time. No Eu^{2+} emission could be detected and no change in colour or refractive index could be observed after the bleaching. It is, however, our interpretation that both P and Ti are involved in the process, as the bleaching is most prominent in samples with high Ti concentrations and the effect was not observed for any of the europium titanate samples investigated in our previous work.[23,24] This indicates that phosphorous is required for the process to take place, either directly or indirectly by increasing the disorder.

Annealing the samples at 400 °C had no effect on the emission of some samples and only a slight effect on others. The photostability was still poor and differences between 300 °C are mainly attributed to uncertainty related to the bleaching effect. Annealing at 500 °C or above resulted in a sharp increase in the photostability. Fig. 6 shows the emission intensity of the 30 EPO sample plotted against the laser exposure time. It is evident that the photostability is dramatically increased after annealing at 600 °C for 10 min, though, the samples are not perfectly photostable and still bleach gradually over time (Fig. S10†). The inset shows a log–log plot that can be used to determine the bleaching rate, β, defined by:

$$I(t) = I_0 t^{-\beta},$$

where $I(t)$ is the emission intensity, t is the laser exposure time, and I_0 is the intensity after 1 second of laser exposure. It follows that in the log–log plot, the linear fit intersects the y-axis at log I_0. As the decay is exponential and goes towards infinity as t approaches 0, it is not possible to determine the emission of a completely unbleached sample; however, the emission after

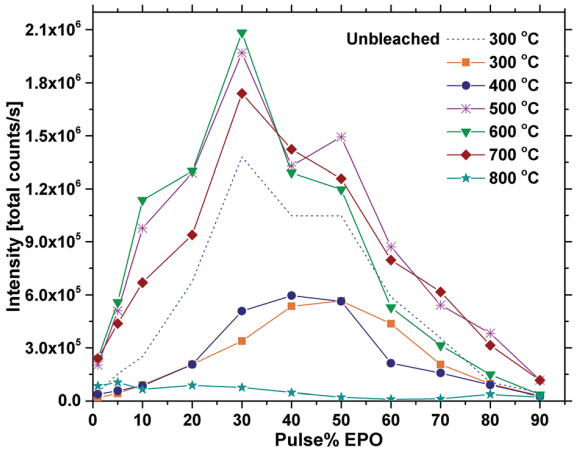

Fig. 5 Total PL intensity *vs.* pulse% EPO for samples annealed at different temperatures (300 °C is as deposited) at 325 nm excitation.

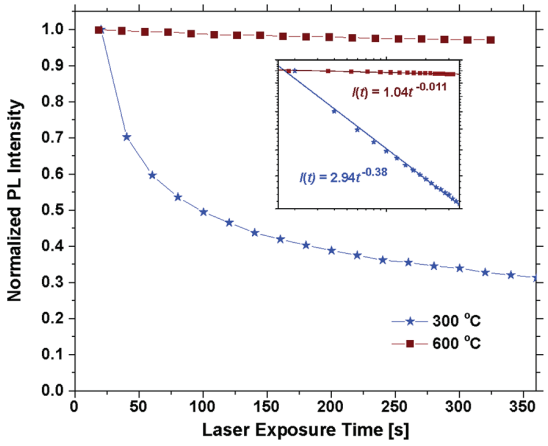

Fig. 6 Normalized PL intensity *vs.* laser exposure time for a sample with 30 EPO as deposited and annealed at 600 °C. Inset shows the same measurements on logarithmic scales and the resulting linear fit.

1 s of laser exposure should serve as reasonable approximation. This value is shown as the dotted line in Fig. 5 for all the as deposited samples. The corresponding bleaching rate for most of the samples is provided in Table 1, and shows that the bleaching increases linearly with reduced EPO (Fig. 11). By taking the bleaching into account, the relative intensities between the different EPO concentrations become similar to the annealed samples, *i.e.* it is only due to the bleaching effect that the 50 EPO sample displays the highest emission intensity as deposited. It could also be that the samples already are severely bleached after 1 s and that the emission observed after annealing at 500 °C best describes the emission of the unbleached samples.

The most important factors that impact the luminescence, and consequently help explain the observations in Fig. 5, are expected to be the energy transfer rate from the $(TiO_6)^{8-}$ complex to Eu^{3+}, and from Eu^{3+} to Eu^{3+}, as well as the symmetry around Eu^{3+} and the amount of quenching centres in the material. As the shape of the emission is identical for all the as deposited samples, the symmetry cannot explain the differences in emission intensity. The energy transfer rates, however, are highly dependent on the distance between the involved atoms and should vary significantly between the samples. The distances can be challenging to determine in amorphous materials, but can nevertheless be estimated in materials made by ALD. The Eu–Eu distance from a single $Eu(thd)_3/O_3$ cycle in the plane of the surface is for instance easily approximated by the size of the organic ligands, which in this case is slightly above 1 nm.[34] The longest distance at which efficient energy transfer between two dipoles takes place, *i.e.* the Förster radius, R_0, is only a few angstroms for the Eu^{3+}–Eu^{3+} couple[35,36] and amorphous mixtures of Eu and Ti have previously been shown to be resistant to concentration quenching[23,37] due to this. It follows that several consecutive EPO cycles would be required for the Eu–Eu distance to be reduced below R_0.

The lifetime of the excited state is very sensitive to all kinds of quenching, including concentration quenching, and it could thus be used to determine how many consecutive EPO cycles can be deposited before concentration quenching becomes dominant. Fig. 7 shows PL decay measurements of the as deposited samples. It is evident that the lifetime of the 80 and 90 EPO samples is severely reduced compared to the samples with less EPO. 80 EPO corresponds to a 1 : 4 pulse ratio of TPO and EPO, *i.e.* four consecutive EPO cycles. With a deposition rate of ~0.8 Å per MP-cycle this should correspond to slightly more than a monolayer. A 1 : 3 pulse ratio of TPO and EPO thus appears to be the limit before concentration quenching becomes dominant. The samples with 5–40 EPO have a fast decaying component hardly noticeable in the 50–90 EPO samples, and can only be fitted with a biexponential decay function (Fig. S12†), while the 50–90 EPO samples can be fitted to a single exponential decay function (Fig. S13†).

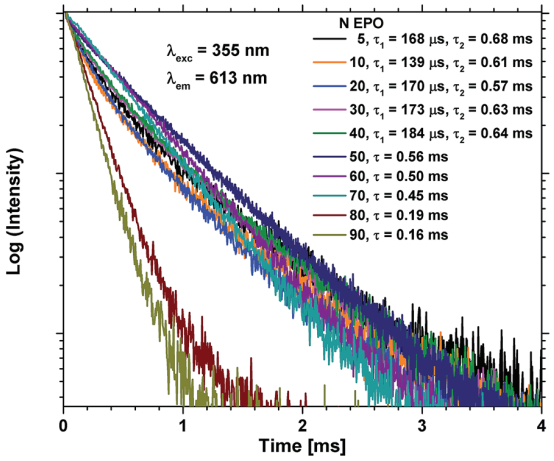

Fig. 7 PL decay measurements of as deposited samples with 5–90 EPO. 5–40 EPO were fitted using a biexponential decay function (Fig. S12†), while 50–90 EPO were fitted using a single exponential decay function (Fig. S13†).

The Ti–Eu distance should decrease with increased EPO content, and the ideal pulse ratio required in order to achieve optimal energy transfer between $(TiO_6)^{8-}$ and Eu^{3+}, while also avoiding concentration quenching, should thus be 1 : 3 between EPO and TPO (*i.e.* 75 EPO should be ideal). For ~100 nm thickness films we observe that 30 EPO displays the strongest emission intensity, however, from the ellipsometry measurements in Fig. 3, it is evident that absorption is a limiting factor for the observed emission in these samples, particularly for samples with low Ti-concentrations. By taking the absorption into account, the relative emission intensities become shifted towards higher EPO, as shown in Table 2. With a sufficiently thick film the 70 EPO sample is expected to exhibit the strongest emission, in agreement with the PL decay measurements. Samples with less than 30 EPO also display a sharply reduced emission. This suggests that energy transfer from $(TiO_6)^{8-}$ is reduced when depositing more than 3 consecutive cycles of TPO.

Annealing at 500–700 °C could have a positive effect on the emission beyond reducing the bleaching, provided that the approximation of the emission of the unbleached samples is valid. This would indicate that a change beyond increased photostability takes place. Fig. 8 shows that the lifetime of a sample with 40 EPO is increased after annealing at 500–700 °C and is strongly correlated to the detected emission intensities (a similar measurement of a 30 EPO sample can be found in Fig. S14†). The radiative lifetime is sensitive to quenching of any

Table 1 Bleaching rate, β, of as deposited samples excited at 325 nm

EPO	5	10	20	30	40	50	60	70	80
β	0.48	0.46	0.44	0.38	0.28	0.21	0.20	0.10	0.03

Table 2 Relative emission intensities, I_r, of unbleached, as deposited samples, adjusted for absorption at 325 nm

EPO	5	10	20	30	40	50	60	70	80
I_r	0.05	0.08	0.26	0.69	0.52	0.77	0.84	1	0.73

kind as well as the local symmetry around Eu^{3+}. As the emission from the $^5D_0 \rightarrow {}^7F_2$ is hypersensitive to the local symmetry around Eu^{3+}, the shape of the emission spectrum can be used to determine whether a change in symmetry actually occurs. Fig. 9 shows that the shape of the PL emission of samples containing 40 EPO and annealed at different temperatures remains constant up to 800 °C. At that point a shoulder appears in the $^5D_0 \rightarrow {}^7F_2$ peak (perhaps more obvious in Fig. S15†), while annealing beyond this quenches the luminescence. The increased lifetime observed after annealing at 500–700 °C can consequently only be due to a reduction in luminesce quenching. As concentration quenching should not be relevant for this sample and Eu-diffusion would result in an observable change in local coordination, it is our interpretation that the increased lifetime must be due to a reduction in the number of quenching sites, or access to these. As the emission rate of the unbleached samples is similar to the samples annealed at 500 °C, where bleaching takes place at a considerably slower rate, it appears that the bleaching is related to these quenching sites. Annealing at 500–700 °C removes a number of the quenching sites and thus also reduces the bleaching.

For the high temperature annealed samples, the exact crystallographic and chemical changes are important factors, and the discussion of emission efficiencies of these samples is more complex. The reduced emission intensity and lifetime observed at 800 °C are interpreted as an increase in the non-radiative decay rate, possibly due to concentration quenching. The change in symmetry around Eu^{3+} is indicative of Eu^{3+} diffusion taking place, probably reducing the Eu–Eu distance. The shoulder present at 800 °C was also observed for all the other samples annealed at the same temperature whose emission could be detected, apart from the sample with 1 EPO (Fig. S16 and S17†). This sample displayed a broad emission in the NIR range, which was enhanced dramatically when the sample was annealed at 1000 °C. This also becomes apparent for some of the other samples, as can be seen in Fig. 10. The NIR emission is most prominent in the samples containing, 1, 5, 60, 80 and 90 EPO, and noticeable in the sample containing 30 EPO. This could be caused by luminescence of rutile TiO_2, which can luminesce at around 850 nm.[38] As the observed emission is not due to an f–f transition, the emission wavelength is strongly affected by the surrounding ligands and it is thus not possible to deduce what kind of titanium phase is actually responsible. The presence of this luminescence implies, however, that some of the titanium ions no longer transfer their energy to nearby europium ions, indicating that the distance between europium and titanium has become too large for efficient energy transfer to take place.

NIR emission has also previously been reported in $KTiOPO_4$,[39] and the NIR emission was enhanced by europium doping. The Eu^{3+} emission observed is similar in shape to $EuPO_4$ emission[40] (Fig. S18†) for all samples, except for the 10

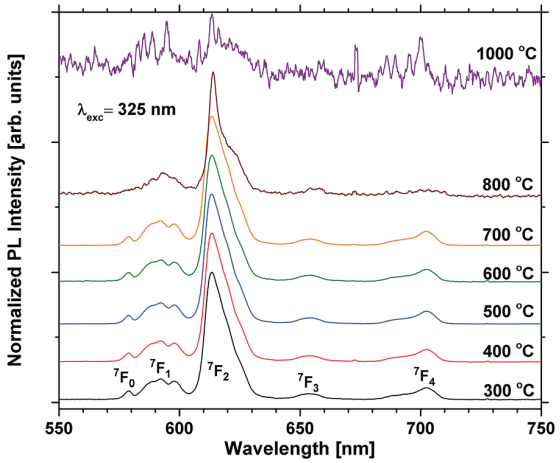

Fig. 9 Normalized PL scans of samples containing 40 EPO. The peaks are a result of emission from the $^5D_0$ state to the states shown in the figure.

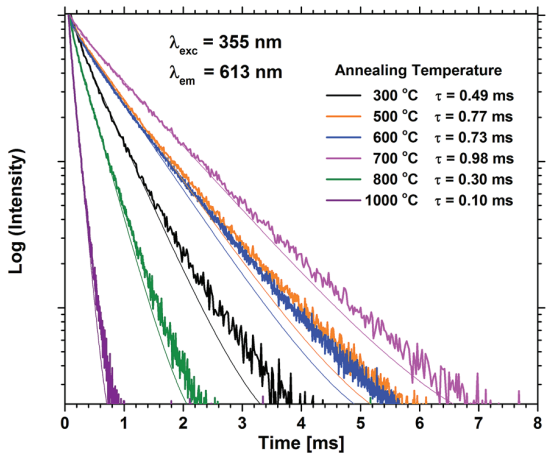

Fig. 8 PL decay measurements of samples containing 40 EPO for various annealing temperatures. τ is the lifetime obtained by fitting to a single exponential decay function.

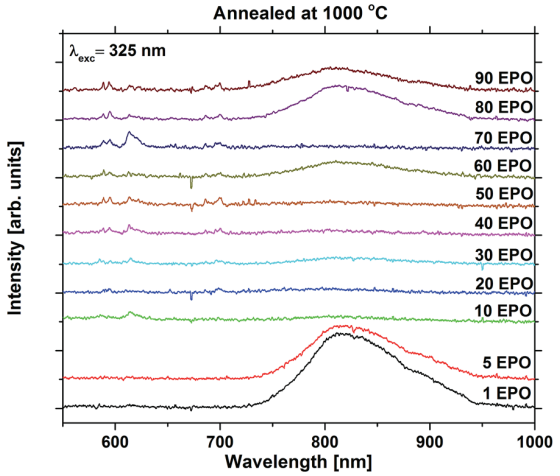

Fig. 10 Emission spectra of samples containing 1–90 EPO and annealed at 1000 °C.

and 70 EPO sample, whose emission still resembles that of the as deposited samples. These samples do not exhibit any NIR emission, which implies that energy transfer still takes place for these samples. As the XRD pattern shows that the $EuPO_4$ phase is present in most of the samples that have been annealed at 1000 °C, and the samples display broad luminescence, which f–f transitions do not display, it can be concluded that most of the Ti and Eu atoms have segregated and formed separate phases. As the separation between Eu-atoms in crystalline $EuPO_4$ is only a few angstroms, the concentration quenching should be very efficient. Combined with a very narrow absorption, the formation of crystalline $EuPO_4$ is expected to be extremely weak. This explains the dramatic drop in the luminescence intensity at 1000 °C, and could also have an effect on the samples annealed at 800 °C.

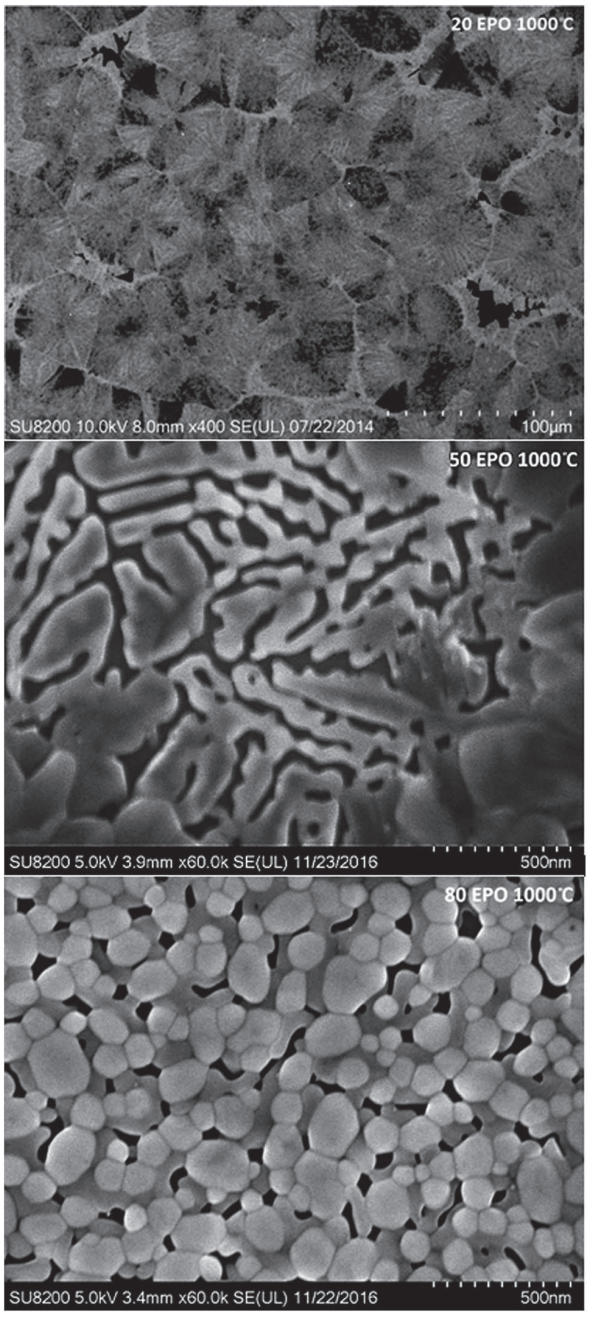

Fig. 11 FE-SEM images of the sample containing 20, 50 and 80 EPO and annealed at 1000 °C.

Diffusion of the various elements in the sample is expected to cause significant changes in the morphology. The samples were consequently investigated with FE-SEM to obtain a better understanding of the processes taking place during annealing. The samples containing 20, 50 and 80 EPO and annealed at 1000 °C, illustrate the phase separation taking place during annealing at this temperature, which is presented in Fig. 11. The image of the sample with 20 EPO exhibits dendritical growth from nucleation centres. This is typical when growth is limited by diffusion of a component in surplus, like the titanium phase in this case. The 50 EPO sample appears to exhibit some dewetting of the film. The reason for this is not clear, but it could be associated with the high atomic mobility of the oxide phases at this temperature. The 80 EPO sample is typical of all the samples with >50 EPO, in which most of the materials have crystallized, which XRD analysis confirms to be $EuPO_4$.

Quantum efficiency measurements performed on samples with 30–60 EPO deposited on fused silica and annealed at 300–600 °C, revealed that the sample with 60 EPO and annealed at 600 °C displayed the highest quantum yield of ~6%. A sample with 70 EPO would likely display a very similar quantum yield, possibly slightly higher. As the lifetime after annealing at 500–700 °C is similar to Eu^{3+} in materials with much higher quantum yields,[36,41] it is our interpretation that most of the energy is lost before it is transferred to Eu^{3+}. The NIR-emission observed in the samples annealed at 1000 °C indicate that the Stokes shift of $(TiO_6)^{8-}$ could be large in this system and can thus easily be quenched.

Summarising the results so far, it appears that photobleaching, possibly related to photostructural changes, dominates the emission signal for the as deposited samples. The material becomes resistant to this upon annealing at 500 °C, and combined with a reduction in the number of quenching sites, it results in significantly increased emission rates. Between 500–700 °C there are only slight changes for most samples, but above 700 °C, migration of most mobile elements, most likely titanium and possibly europium, cause the symmetry around Eu^{3+} to change, also accompanied by a reduction in emission rate and lifetime of the Eu^{3+} emission. The migration of these elements allows for various crystalline phases, as well as grain boundaries between them, to form, which results in reduced Eu–Eu distances and increased Ti–Eu distances, reducing the energy transfer rate between them, which results in NIR emission from the titanium phase.

While the quantum efficiency is too low for most applications, amorphous Eu–Ti–P–O thin films still offers some unique and interesting properties, like tuneable bleaching and emission that could potentially be exploited in future applications.

Conclusion

Through this work we have demonstrated that the EPO–TPO growth can be controlled by ALD. The optimal pulse ratio of EPO and TPO with respect to emission intensity with 325 nm excitation was found to be 3 : 7 for ~100 nm thickness films, though 7 : 3 was found to be optimal for thick films where absorption is not an issue. The optimal annealing temperature was determined to be 500–700 °C, depending on the pulse ratio. The highest measured quantum efficiency for the system was found to be ~6% for a sample with 60 EPO annealed at 600 °C.

All as deposited samples containing both Ti and Eu luminesce red light when exposed to UV, though, the emission intensity drops off rapidly when exposed to UV or X-ray radiation for a prolonged duration. The luminescence recovers when the sample is tempered. The bleaching rate can be tuned by varying the Ti-concentration in the samples, with increased bleaching rates for high Ti-concentrations. The photostability of all samples is dramatically increased by annealing at 500–700 °C. However, the luminescence is sharply reduced for all compositions when annealed at 800 °C. This has been interpreted to be due to increased diffusion of the various elements in the sample at this temperature, resulting in increased Ti–Eu distances, with an accompanied change in local coordination around Eu^{3+}, resulting in increased local symmetry. This reduces the spontaneous emission rate due to the parity forbidden nature of the transition, resulting in significantly reduced emission rates.

After annealing the samples at 1000 °C, the Eu^{3+} luminescence is more or less completely quenched for all compositions due to phase separation into various crystalline phases like $EuPO_4$ and TiO_2. This causes a sharp reduction in the energy transfer between Ti- and Eu-ions in the material resulting in broad, but weak NIR-emission from the titanium for most of the compositions.

Acknowledgements

This work was performed within "The Norwegian Research Centre for Solar Cell Technology", a Centre for Environment-Friendly Energy Research. The authors would also like to thank the Department of Geosciences, UiO, for use of the XRF equipment, the Institute for Energy Technology for use of the VASE ellipsometer, and the group of Professor Andries Meijerink at Utrecht University, for use of equipment and assistance with experiments.

References

1 M.-F. Joubert, *Opt. Mater.*, 1999, **11**, 181–203.
2 D. Chen, Y. Yu, P. Huang, H. Lin, Z. Shan, L. Zeng, A. Yang and Y. Wang, *Phys. Chem. Chem. Phys.*, 2010, **12**, 7775–7778.
3 L. Chen, K.-J. Chen, C.-C. Lin, C.-I. Chu, S.-F. Hu, M.-H. Lee and R.-S. Liu, *J. Comb. Chem.*, 2010, **12**, 587–594.
4 D. Cavouras, I. Kandarakis, G. S. Panayiotakis, E. K. Evangelou and C. D. Nomicos, *Med. Phys.*, 1996, **23**, 1965–1975.
5 J.-C. G. Bunzli and C. Piguet, *Chem. Soc. Rev.*, 2005, **34**, 1048–1077.
6 S. N. Misra, M. A. Gagnani, I. M. Devi and R. S. Shukla, *Bioinorg. Chem. Appl.*, 2004, **2**, 155–192.
7 T. Yanagida, *Opt. Mater.*, 2013, **35**, 1987–1992.
8 G. Bonnet, M. Lachkar, J. P. Larpin and J. C. Colson, *Solid State Ionics*, 1994, **72**, 344–348.
9 K. J. Hubbard and D. G. Schlom, *J. Mater. Res.*, 1996, **11**, 2757–2776.
10 B. S. Richards, *Sol. Energy Mater. Sol. Cells*, 2006, **90**, 1189–1207.
11 T. Trupke, A. Shalav, B. S. Richards, P. Würfel and M. A. Green, *Sol. Energy Mater. Sol. Cells*, 2006, **90**, 3327–3338.
12 B. M. van der Ende, L. Aarts and A. Meijerink, *Phys. Chem. Chem. Phys.*, 2009, **11**, 11081–11095.
13 J. Y. Chen, C. K. Huang, W. B. Hung, K. W. Sun and T. M. Chen, *Sol. Energy Mater. Sol. Cells*, 2014, **120**, 168–174.
14 K. Hermans and B. Slager, WO2010046358A1, 2010.
15 C. Wiemer, L. Lamagna and M. Fanciulli, *Semicond. Sci. Technol.*, 2012, **27**, 074013.
16 M. Coll, J. Gazquez, A. Palau, M. Varela, X. Obradors and T. Puig, *Chem. Mater.*, 2012, **24**, 3732–3737.
17 M. Coll, J. M. Montero Moreno, J. Gazquez, K. Nielsch, X. Obradors and T. Puig, *Adv. Funct. Mater.*, 2014, **24**, 5368–5374.
18 X. Wang, L. Dong, J. Zhang, Y. Liu, P. D. Ye and R. G. Gordon, *Nano Lett.*, 2013, **13**, 594–599.
19 V. Miikkulainen, M. Leskelä, M. Ritala and R. L. Puurunen, *J. Appl. Phys.*, 2013, **113**, 021301.
20 V. Miikkulainen, O. Nilsen, M. Laitinen, T. Sajavaara and H. Fjellvag, *RSC Adv.*, 2013, **3**, 7537–7542.
21 E. Ostreng, H. H. Sonsteby, T. Sajavaara, O. Nilsen and H. Fjellvag, *J. Mater. Chem. C*, 2013, **1**, 4283–4290.
22 H. H. Sønsteby, H. FJellvåg and O. Nilsen, *Adv. Mater. Interfaces*, 2017, 1600903.
23 P.-A. Hansen, H. Fjellvåg, T. G. Finstad and O. Nilsen, *Chem. Vap. Deposition*, 2014, **20**, 274–281.
24 P.-A. Hansen, H. Fjellvag, T. G. Finstad and O. Nilsen, *RSC Adv.*, 2014, **4**, 11876–11883.
25 A. C. Mendes, L. J. Q. Maia, S. H. Messaddeq, Y. Messaddeq, S. J. L. Ribeiro and M. Siu Li, *Phys. B*, 2011, **406**, 4381–4386.
26 M. Nalin, Y. Messaddeq, S. J. L. Ribeiro, M. Poulain and V. Briois, *J. Optoelectron. Adv. Mater.*, 2001, **3**, 553–558.
27 S. R. Elliott, *J. Non-Cryst. Solids*, 1986, **81**, 71–98.
28 K. Schwartz, *The Physics of Optical Recording*, Springer, Berlin, 1993.
29 K. B. Gandrud, A. Pettersen, O. Nilsen and H. Fjellvag, *J. Mater. Chem. A*, 2013, **1**, 9054–9059.
30 Y. Ni, J. M. Hughes and A. N. Mariano, *Am. Mineral.*, 1995, **80**, 21–26.
31 G. L. Breneman and R. D. Willett, *Acta Crystallogr.*, 1967, **23**, 334.
32 Y. Kuzukawa, A. Ganjoo and K. Shimakawa, *J. Non-Cryst. Solids*, 1998, **227–230**, 715–718.
33 K. Sawada and S. Adachi, *J. Appl. Phys.*, 2015, **118**, 103106.

34 R. Metzger, C. Werner and A. Spitzer, *Thin Solid Films*, 2000, **365**, 242–250.
35 Z. Wang, J. Zhong, H. Liang and J. Wang, *Opt. Mater. Express*, 2013, **3**, 418–425.
36 M. Janulevicius, P. Marmokas, M. Misevicius, J. Grigorjevaite, L. Mikoliunaite, S. Sakirzanovas and A. Katelnikovas, *Sci. Rep.*, 2016, **6**, 26098.
37 J. Ovenstone, P. J. Titler, R. Withnall and J. Silver, *J. Mater. Res.*, 2002, **17**, 2524–2531.
38 X. Wang, Z. Feng, J. Shi, G. Jia, S. Shen, J. Zhou and C. Li, *Phys. Chem. Chem. Phys.*, 2010, **12**, 7083–7090.
39 O. Plantevin, E. Oliviero, G. Dantelle and L. Mayer, *Nucl. Instrum. Methods Phys. Res., Sect. B*, 2014, **326**, 106–109.
40 J. Dexpert-Ghys, R. Mauricot and M. D. Faucher, *J. Lumin.*, 1996, **69**, 203–215.
41 Y. Huang, Y. Nakai, T. Tsuboi and H. J. Seo, *Opt. Express*, 2011, **19**, 6303–6311.

Supplementary

Table S1: Overview of number of MP-cycles, thickness (from ellipsometry), deposition rate, relative concentrations of each cation (from XRF), and surface roughness, R_q (from AFM for the as deposited thin films). NM means that no measurement data is available for that sample.

Pulse % EPO (%)	MP - cycles	Thickness (nm)	Deposition rate (Å/MP-cycle)	Eu % (cation %)	Ti % (cation %)	P % (cation %)	R_q (nm)
0	1000	82	0.82	0	46.0	54.0	NM
1	1400	113	0.81	NM	NM	NM	NM
5	1160	92	0.79	2.1	44.2	53.7	0.35
10	1150	97	0.84	3.0	41.7	55.3	0.30
20	1125	93	0.83	5.9	38.7	55.5	0.35
30	1220	104	0.86	8.8	34.3	56.9	0.31
40	1100	95	0.86	11.3	30.8	57.9	0.30
50	1080	100	0.92	13.9	27.0	59.1	0.37
60	1065	89	0.84	18.7	22.3	59.0	0.24
70	1100	97	0.88	23.7	17.4	58.9	0.25
80	1125	96	0.86	27.3	11.8	60.9	0.35
90	1060	97	0.92	32.4	6.5	61.1	0.33
100	1000	101	1.01	37.9	0	62.1	NM

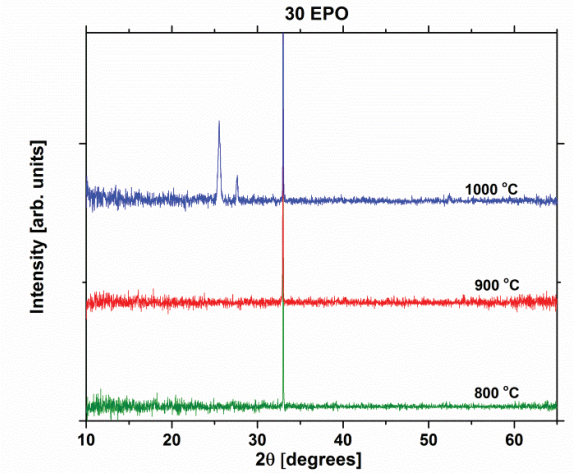

Figure S1: XRD 30 EPO 800-1000 °C. No crystalline phase could be detected after annealing below 900 °C.

Table S2: Surface Roughness, R_q, in nm from AFM scans shown in **Figure S2** and **Figure S3**.				
Annealing Temperature (°C)	**20 EPO**	**30 EPO**	**70 EPO**	**80 EPO**
600	0.3	0.2	-	-
700	2.0	2.9	0.1	0.1
800	11.3	2.0	1.0	1.1
1000	11.3	9.8	7.4	6.1

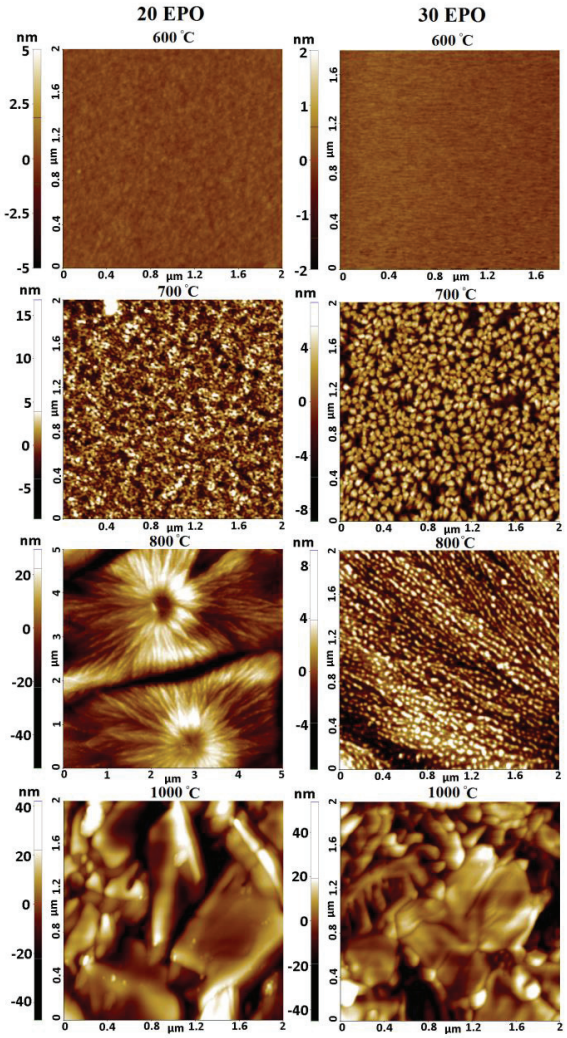

Figure S2: AFM images of samples with 20 EPO (left column) and 30 EPO (right column), annealed at 600, 700, 800 and 1000 °C. 20 and 30 EPO samples annealed at 600 °C or below did not exhibit any features. 20 EPO at 800 °C shows a larger scan area in order to

better display the morphology of the sample. Note the difference in the z-scale.

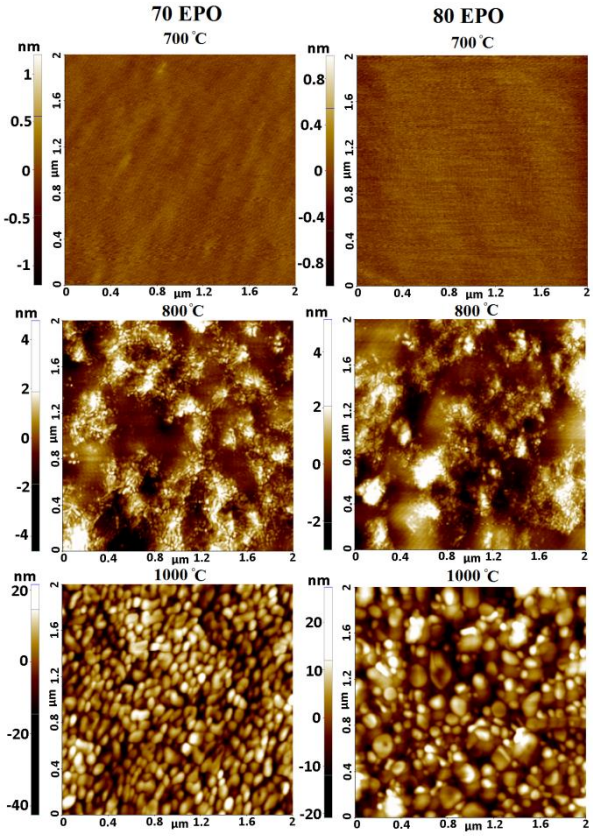

Figure S3: AFM images of samples with 70 EPO (left column) and 80 EPO (right column), annealed at 700, 800 and 1000 ˚C. 70 and 80 EPO samples annealed at 700 °C or below did not exhibit any features. Note the difference in the z-scale.

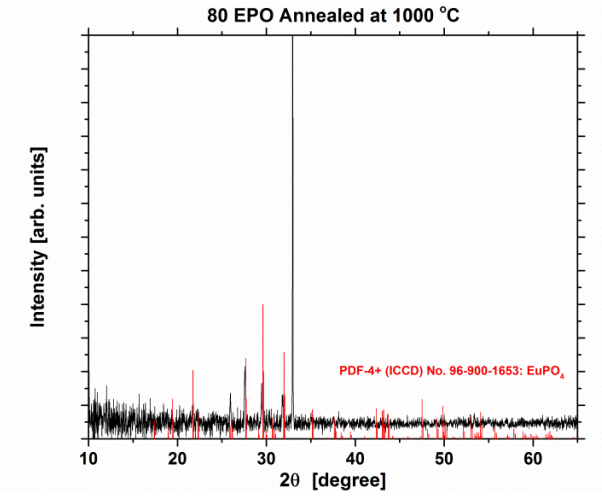

Figure S4: XRD of 80 EPO compared with EuPO4 crystal data.

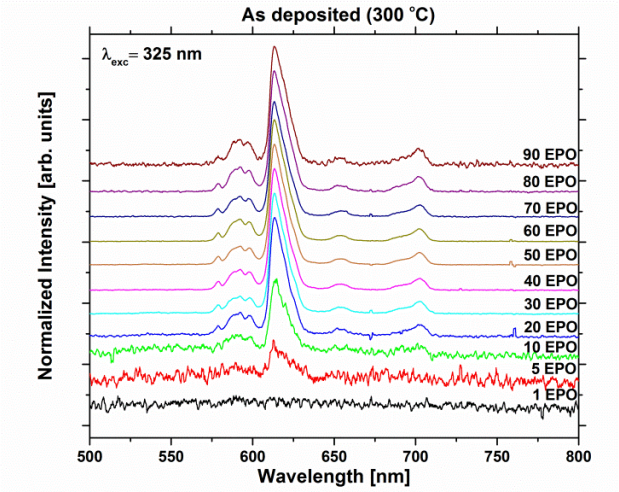

Figure S5: Normalized PL emission spectra of as deposited samples with increasing pulse % EPO from bottom to top. 1-10 EPO are quenched due to photobleaching.

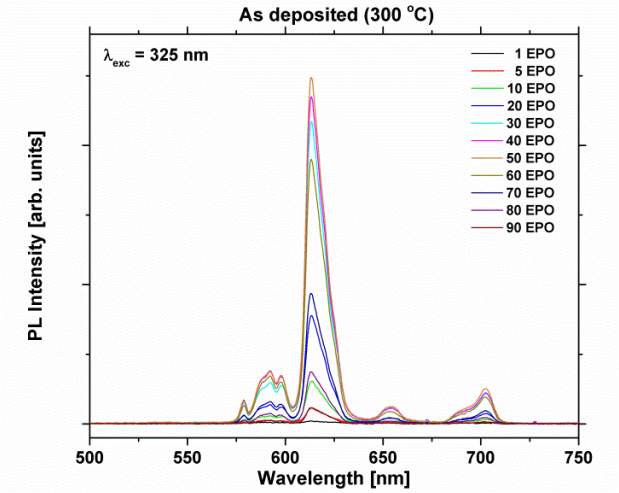

Figure S6: PL of as deposited samples after 20 s of laser exposure. Shape of emission is identical for all compositions.

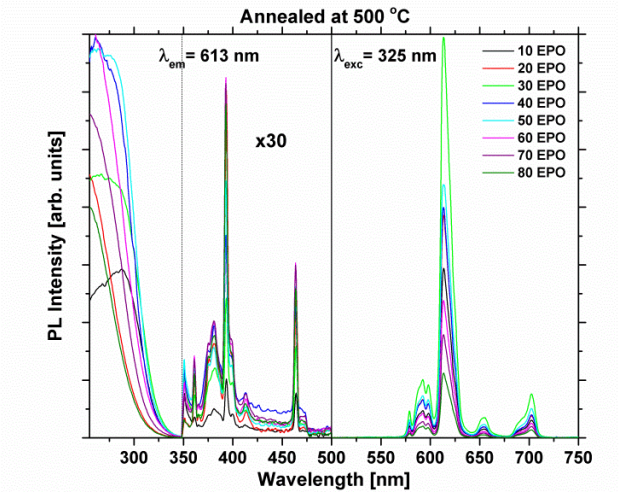

Figure S7: Excitation measurements of 10-80 pulse % EPO of samples annealed at 500 °C, monitoring the Eu^{3+} emission at 613 nm (left). PL emission from 325 nm laser (right). PLE and PL were not measured with the same equipment.

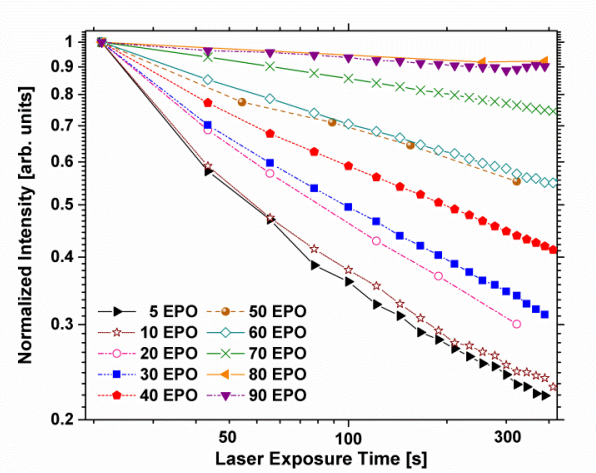

Figure S8: Normalized PL intensity vs. laser exposure time for as deposited samples plotted on logarithmic scales.

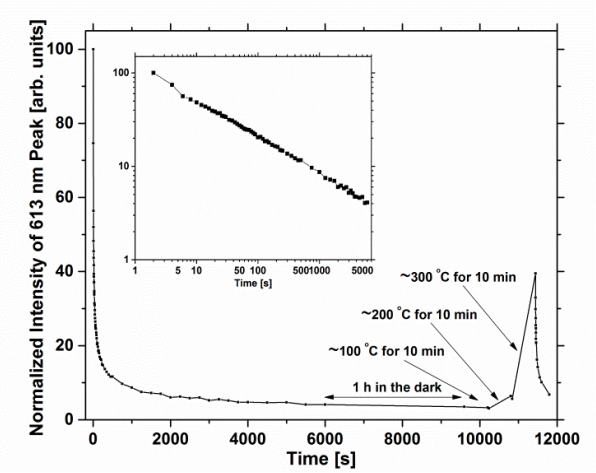

Figure S9: Normalized luminescence intensity of the Eu^{3+} emission at 613 nm for an as deposited sample containing 20 EPO vs. laser exposure time. After 6000 s the sample was left in the dark for 1 h before being heated on a hot plate for 10 min at 100, 200 and 300 °C. The luminescence was completely recovered after tempering in a furnace at 300°C for 1 h. Inset shows the first 6000 s of the experiment on logarithmic scales.

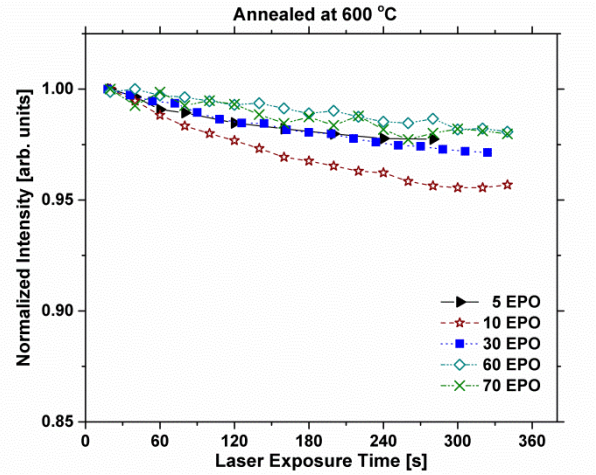

Figure S10: Normalized PL intensity vs. laser exposure time for selected samples annealed at 600 ˚C, plotted on a linear scales.

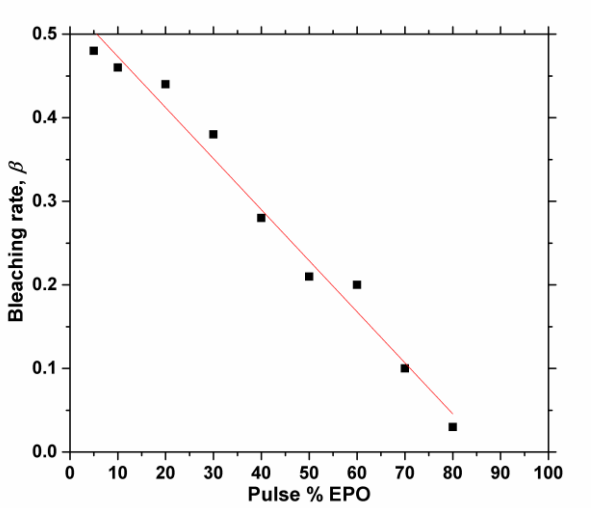

Figure S11: Bleaching rate for as deposited samples exposed to 325 nm excitation, fitted to a linear curve. 1 and 90 EPO were omitted due to low signal to noise ratio for these samples.

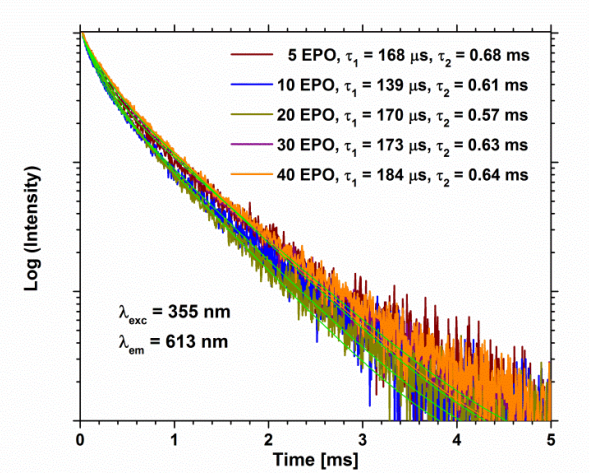

Figure S12: PL decay measurements of as deposited samples with 5-40 EPO, fitted by a biexponential decay function.

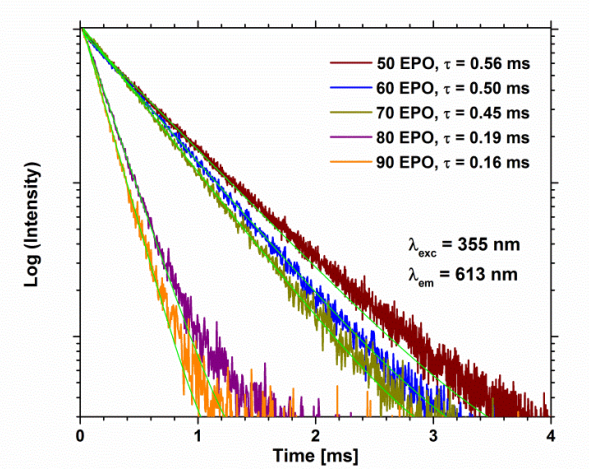

Figure S13: PL decay measurements of as deposited samples with 50-90 EPO, fitted by a single exponential decay function.

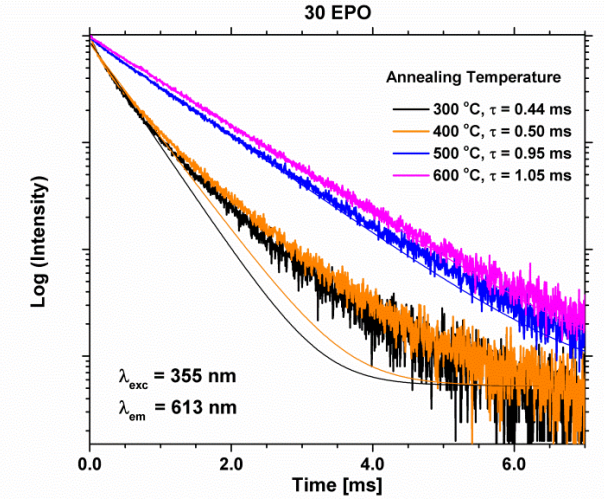

Figure S14: PL decay measurements of samples with 30 EPO and annealed at 300-600 °C. τ is extracted from fitting the data to a single exponential decay function.

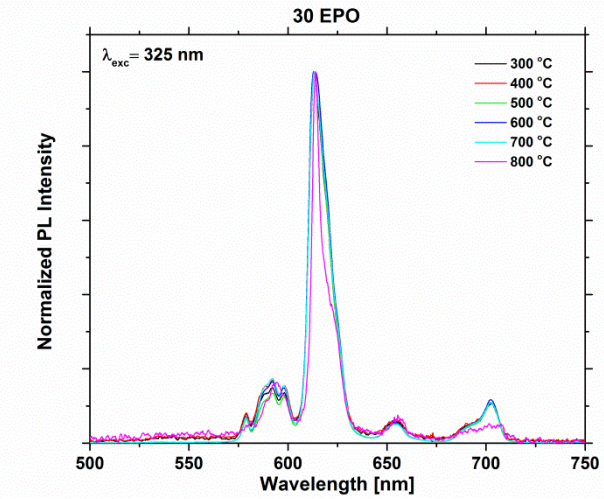

Figure S15: Normalized PL of samples containing 30 EPO and annealed at 300-800 °C. The shape of the spectrum remains unchanged up to 800 °C.

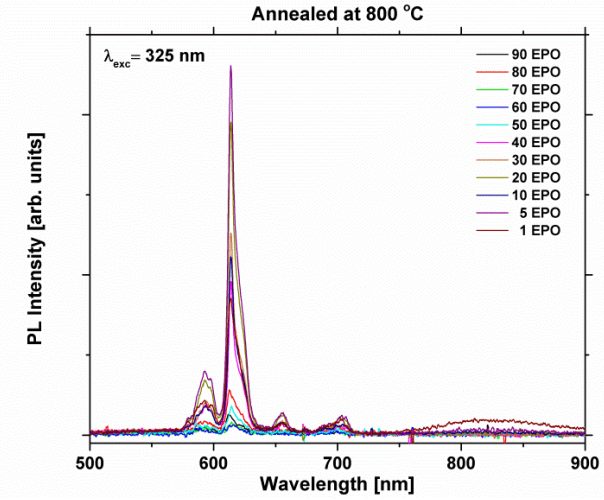

Figure S16: PL of samples annealed at 800 °C.

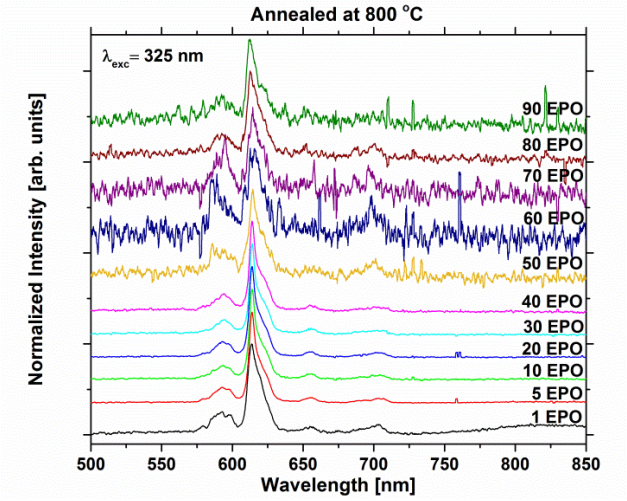

Figure S17: Normalized PL scans of samples annealed at 800 °C.

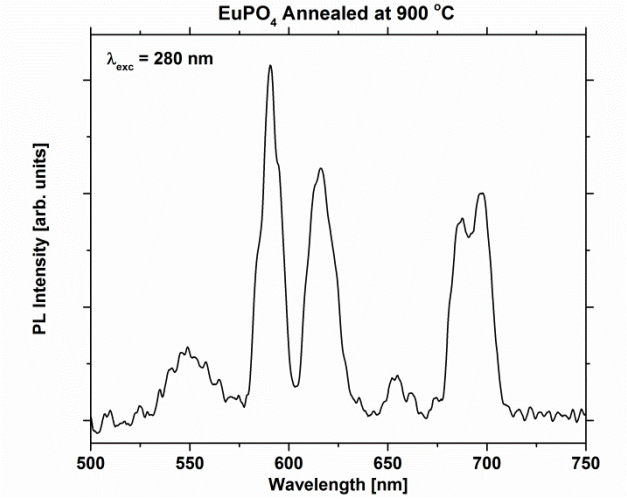

Figure S18: PL emission of 100 EPO annealed at 900 °C.